

Methods to hyperpolarize nuclear spins via dissolution and sublimation DNP at high magnetic field

THÈSE N° 6927 (2016)

PRÉSENTÉE LE 11 MARS 2016
À LA FACULTÉ DES SCIENCES DE BASE
GROUPE COMMENT
PROGRAMME DOCTORAL EN PHYSIQUE

ÉCOLE POLYTECHNIQUE FÉDÉRALE DE LAUSANNE

POUR L'OBTENTION DU GRADE DE DOCTEUR ÈS SCIENCES

PAR

Andrea CAPOZZI

acceptée sur proposition du jury:

Prof. V. Savona, président du jury
Prof. A. Comment, Dr C. Roussel, directeurs de thèse
Prof. J.-H. Ardenkjaer-Larsen, rapporteur
Prof. G. Jeshke, rapporteur
Dr G. Boero, rapporteur



ÉCOLE POLYTECHNIQUE
FÉDÉRALE DE LAUSANNE

Suisse
2016

To my beloved father

*“I think physicists are the Peter Pans of the human race. They never grow
up and they keep their curiosity.”*

I. I. Rabi

Acknowledgments

Dear all,

after four years I have come to the end of a long beautiful journey. I still remember as if it was yesterday, when I packed my room in Pavia and I came to Lausanne. Someone says that when you feel the time passing so fast you are enjoying it; and that was the case for me. For sure during my PhD I grew up from the scientific point of view, but most of all from the human one. Because of all the experiences I had the chance to have I now consider myself a richer person. Without many of you, all that would not have been possible!

First of all I want to tank you Arnaud. You have been an amazing thesis director! Thanks for the interesting and challenging research subjects you offered me and for all the trust, the freedom and fruitful discussions along these years. Many thanks also for all the "non-working" time we spent together. You are a really fair person! I wish you all the best for your new carrier in Cambridge.

Thank you Jacques for all the time you spent with me even though you did not have any official duty. Thanks for all your invaluable help and suggestions. At your age I would be honored to have half of your enthusiasm and knowledge.

Cher Jean-Noel, you have been a constant and very important presence during these years. You were at the same time PhD co-supervisor, PhD buddy, assistant, running partner, climbing partner and most of all a very very very good friend! Thank you so

much to you and your nice family...vous êtes énormes! Many thanks also for having squatted my couch every week for at least two years...at that time it was not an easy period for me, and having you at home made me feel much less alone :)

Thank you Christophe for your stubbornness in explaining me Chemistry... at the end I probably understood something :) Thanks also for your moral support, your political incorrectness and all the funny moments we spent together in your office.

Thanks a lot Tian, my hardware angel. You have been extremely important especially at the beginning! You are just incredible, always ready to help me during the day, the night, the week and the weekends! You have been a patient and precious teacher. Thank you from the bottom of my heart.

Merci Najat pour ton amitié! Excepted for all the suitable sleeping hours I lost with you in front of the scanner ;) I remember with big big pleasure each moment we spent together.

Grazie Mor and Simone for all the fruitful and interesting discussions we had together. Many thanks for the amazing Italo-Israeli fusion cuisine I had the chance to try at you place. You added a spot of Mediterranean taste during my PhD.

Thank you Lillian for making our life much easier every day... as you say...only solutions!!!

A big thank also to the rest of the DNP team: Hikari, Riccardo, Jess, Elise, Yuhei and most of all Emine...my four years long super nice and quite office mate.

Un grand merci à Florent et à la "coloc des rêves", for all the nice time we spent together parting, climbing and running!!! Av. de Sévelin 4a is the place to be!!!

Thank you Alberto, my elder brother in-law. During these years you have always been there, ready to give me suggestions and support through your very sharp and critical point of view. A big thank also to Khati and Pancito, I miss you so much now that you are in Cambridge...

Grazie mille to the CHUV Italian clan: Gabri, Simo, la Ginami and especially Robb . Bob all the feelings I have for you can be summarized in..."CHE MASCHIO" :)

Grazie di cuore to my 10 years long friends Valeria and Valentina. I am so happy we kept in touch during these last years even tough we were far away. Vi voglio un sacco di bene!!!

Bella Cucci for all dreams you sell me every day! Watch out for "la Flaca"... always remember this link when you feel weak https://www.youtube.com/watch?v=_R8XkdFSJqM.

Grazie Giulia for one and a half year brainstorming. You are a really deep and precious person.

Grazie to my best friend Stefanino to be always on my side and to pop-up (using bla-bla car) when you do not expect it shaking up your weekend :)

Last but not least...the biggest thanks is for my family. I left almost 10 years ago when I was little more than a kid and you always supported me. Most of all...Grazie Pap ...I have to admit that if I decided to study Physics is because of you, if I came to Lausanne is because of you and if I am now getting my PhD is because of you, but...the most amazing thing is that you never forced me to do so, you just transmitted me your passion for this amazing job :)

Facete bonum

Andrea

Abstract

Dynamic Nuclear Polarization (DNP) is, nowadays, the most well-established and widespread Nuclear Magnetic Resonance (NMR) hyperpolarization technique. With respect to other methods, the main advantage of DNP is, with no doubt, its versatility. In theory each NMR active nuclear spin species can be polarized via DNP, allowing to obtain enhanced NMR signals from samples in the solid state, liquid state and gas state. Thus its utility ranges from material science to biomedicine.

The DNP process efficiency is strongly influenced by experimental conditions (temperature and magnetic field) as well as samples preparation. The fine tuning of these features is often asserted as the key point for practical purposes, where it is desirable to obtain a nuclear polarization as high as possible in a relatively short amount of time.

The aim of the present thesis work is to look into some of these aspects, trying to understand up to which point the technique can be improved. Big emphasis is given to the study of the phenomenon at high magnetic field, one of the current hot topics within the DNP community. Moreover the feasibility for the production of hyperpolarized ^{129}Xe gas is studied, showing that sublimation-DNP represents a promising alternative to the well-established Spin Exchange Optical Pumping (SEOP), when the sample preparation is carefully optimized. The most interesting and innovative part of the thesis is centered around the investigation of a new kind of photo-induced non-persistent radicals. Their use as DNP polarizing agents was tested on several nuclei (^{13}C , ^{129}Xe ,

^6Li , ^1H) in unfavorable hyperpolarized (HP) solution transfer conditions. It was indeed demonstrated that, the natural recombination of the paramagnetic centers, when the temperature is increased, helps in preserving the highly out-of-equilibrium nuclear spin order of the dissolved sample. Moreover, we believe the UV-radicals unique property of self-quenching could represent the first step towards the development of a simple way to handle and store nuclear polarization, by means of the generation of highly polarized radical-free solid samples.

Keywords

Nuclear Magnetic Resonance (NMR), Electron Spin Resonance (ESR), Dynamic Nuclear Polarization (DNP), dissolution-DNP, sublimation-DNP, nitroxyl radicals, UV-induced non-persistent-radicals, ^{13}C NMR, ^{129}Xe NMR, ^6Li NMR, ^1H NMR.

Résumé

La technique de Polarisation Nucléaire Dynamique (DNP) est, aujourd’hui, la méthode d’hyperpolarisation la plus répandue et la plus établie en Résonance Magnétique Nucléaire (RMN). Par rapports aux autres méthodes, l’avantage principal de la DNP est, sans aucun doute, son large champ d’application. En effet, en principe, n’importe quel noyau de spin non nul (donc actif en RMN) peut être hyperpolarisé (HP) par DNP, ce qui permet d’obtenir un rehaussement du signal RMN d’échantillons à l’état solide, liquide ou gazeux. Elle trouve donc des applications dans des domaines aussi variés que la physique des matériaux ou l’imagerie médicale.

L’efficacité du mécanisme DNP est très influencée par la composition de l’échantillon et par les conditions expérimentales (température et champ magnétique). L’optimisation de ces paramètres est un point clé pour pouvoir obtenir expérimentalement la polarisation nucléaire la plus élevée dans un temps raisonnable. L’objectif de cette thèse est de mieux comprendre les mécanismes en jeu et les optimisations pratiques possibles pour tirer le meilleur parti de cette technique. D’abord, une attention particulière a été portée à l’étude du phénomène à haut champ magnétique, une question actuellement très discutée dans la communauté DNP. Ensuite les nouvelles stratégies pour la production de ^{129}Xe Hyperpolarisé proposées dans cette thèse, montre que la technique dite de ”sublimation-DNP” est une alternative prometteuse à la technique de référence actuelle, à savoir le pompage optique indirect par échange de spins (SEOP), lorsque la

préparation des échantillons est soigneusement optimisée. La partie la plus innovante et intéressante de ce travail de thèse est centrée sur l'étude des propriétés et applications potentielles d'un nouveau type d'agent polarisant : des radicaux non persistants photo-induit dans une molécule organique bio-compatible. Ce nouveau type de radicaux a été utilisé pour polariser différents noyaux (^{13}C , ^{129}Xe , ^6Li , ^1H) dans des conditions peu favorables de transfert de la solution hyperpolarisée. De plus on croit que cette unique propriété de recombinaison naturelle des centres paramagnétiques, peut représenter un bon point de départ en vue d'une solution bon marché et technologiquement simple pour le stockage de la polarisation nucléaire, par voie de la génération d'un échantillon hyperpolarisé sans radical.

Mots clés

Résonance Magnétique Nucléaire (RMN), Résonance Paramagnétique Electronique (RPE), Polarisation Nucléaire Dynamique (DNP), dissolution-DNP, sublimation-DNP, radicaux nitroxyl, radicaux non persistants photo-induits, RMN du ^{13}C , RMN du ^{129}Xe , RMN du ^6Li , RMN du ^1H .

Contents

List of Figures	xii
List of Tables	xv
1 Introduction	1
1.1 Context	1
1.2 Aim of the thesis	4
1.3 Structure of the thesis	5
2 Hyperpolarization techniques overview	7
2.1 Concept of spin polarization and NMR signal	7
2.2 Brute force	11
2.3 Spin exchange optical pumping	12
2.4 Parahydrogen-induced polarization	14
2.5 Dissolution-DNP: a practical approach	16
2.5.1 Sample preparation	17
2.5.2 Experimental conditions	19
2.5.3 The dissolution step	22
3 Theoretical background	25
3.1 Introduction	25

3.2	The spin Hamiltonian	26
3.2.1	Electron and nuclear Zeeman interaction	26
3.2.2	Hyperfine interaction	28
3.2.3	Zero-field splitting	29
3.2.4	Nuclear quadrupole interaction	30
3.2.5	Nuclear dipolar interaction	31
3.2.6	DNP system approximations	33
3.3	Spin transitions and relaxation processes	38
3.3.1	Electron relaxation processes	40
3.3.2	Nuclear relaxation processes	43
3.4	DNP via Thermal Mixing	47
3.4.1	Spin Temperature theory and "Dynamic Cooling"	48
3.4.2	"Thermal Mixing" in the strict sense	52
3.4.3	"Low temperature case": the Borghini model	55
4	High field DNP: the breakdown of the Thermal Mixing regime	59
4.1	Introduction	60
4.2	Experimental methods	61
4.2.1	Samples preparation	61
4.2.2	Solid state DNP measurements	63
4.2.3	Calculated ESR spectra	65
4.3	Experimental results	66
4.4	Discussion	67
4.4.1	Relation with earlier results	67
4.4.2	Data analysis at 3.4 T and 5 T	71
4.4.3	Data analysis at 7 T	73

5	UV-induced non-persistent radicals for DNP	77
5.1	Introduction	78
5.2	UV-radicals for X-nuclei dissolution-DNP	81
5.2.1	Experimental methods	81
5.2.2	Results and discussion	85
6	Hyperpolarized Xenon gas via sublimation-DNP	99
6.1	Introduction	100
6.2	Experimental methods	101
6.3	Results and discussion	104
7	Conclusions and perspectives	113
7.1	The influence of the magnetic field on the DNP process	113
7.2	UV-induced non-persistent radicals	115
7.3	HP ^{129}Xe gas via sublimation-DNP	117
A	Chapter 4 supplementary material	119
A.1	Solid state ^{13}C NMR spectral line width	119
A.2	Microwave power calibration	120
B	Chapter 5 supplementary material	123
B.1	X-band ESR spectrometer calibration curve	123
B.2	5 T ^{129}Xe and 7 T ^6Li (^{13}C) microwave spectra	124
C	EasySpin ESR spectra fitting and calculation	125
C.1	X-band TEMPO radical fit	125
C.2	X-band UV-irradiated PA fit	126
C.3	X-band UV-irradiated 1- ^{13}C -PA fit	128
C.4	X-band UV-irradiated 2- ^{13}C -PA fit	129

C.5	X-band UV irradiated d4-PA ($S = 1/2$) fit	130
C.6	X-band UV-irradiated d4-PA ($S = 1$) fit	131
C.7	TEMPO radical calculated spectrum at 3.4 T	132
C.8	TEMPO radical calculated spectrum at 5 T	133
C.9	UV-PA radical calculated spectrum at 5 T	135
C.10	UV-d4-PA radical calculated spectrum at 5 T	136
C.11	TEMPO radical calculated spectrum at 7 T	137
D	Chapter 6 supplementary material	139
D.1	Polarization build-up time constant	139
D.2	Supplementary xenon solid state spectra	142
D.3	Solid state xenon NMR spectral line width	142
	Bibliography	145
	List of publication	163
	Curriculum vitae	169

List of Figures

1.1	DNP main parameters sketch.	4
2.1	Thermal equilibrium vs HP state.	11
2.2	SEOP method.	12
2.3	PHIP method.	15
2.4	ESR vs DNP microwave spectra.	18
2.5	P_{0S} , P_{0I} and T_{1S} temperature dependence.	20
2.6	Original dissolution-DNP setup by Ardenkjaer-Larsen et al..	21
2.7	Transfer setup CIBM.	23
3.1	TEMPO free radical sketch.	27
3.2	TEMPO radical: dipolar-broadening effect.	35
3.3	Sketch of different spin transitions.	39
3.4	Spin packets model.	41
3.5	Field dependence of T_{1I} and $T_{I,SS}$	47
3.6	Population distribution and "Spin Temperature".	50
3.7	Theoretical "high temperature" DNP microwave spectrum.	54
3.8	Thermal Mixing diagram.	57
4.1	DNP polarizer inserts.	62
4.2	Solid state NMR circuit.	64

4.3	TEMPO X-band ESR spectrum.	65
4.4	Magnetic field dependence of $g(\omega_I)/g(0)$	68
4.5	DNP ^{13}C and ^1H microwave spectra at 3.4 T and 5 T.	69
4.6	DNP "best enhancement" as a function of deuteration.	70
4.7	Relation between TM speed and DNP enhancement.	72
4.8	DNP ^{13}C and ^1H microwave spectra at 7 T.	73
4.9	Solid-state sodium acetate ^{13}C NMR line width.	75
5.1	Phosphorescence Jablonsky diagram.	78
5.2	α -keto acid general chemical structure.	79
5.3	UV-radical generation mechanism.	80
5.4	UV-induced radicals ESR spectra.	86
5.5	UV-irradiated PA line broadening.	88
5.6	UV-radical yield irradiation time and PA concentration dependence.	90
5.7	UV radicals ^{129}Xe and ^6Li DNP.	91
5.8	UV-radicals microwave spectra at 5 T.	93
5.9	Sodium $[1-^{13}\text{C}]$ acetate dissolution-DNP with UV-radicals.	96
6.1	Xenon samples preparation procedure.	103
6.2	Xenon solubility threshold.	104
6.3	Inhomogeneous solid state ^{129}Xe DNP spectrum.	106
6.4	Solvent polarity effect on ^{129}Xe DNP spectra.	107
6.5	Matrix deuteration effect on ^{129}Xe polarization.	108
6.6	HP ^{129}Xe gas imaging.	110
A.1	Microwave power calibration at 3.4 T.	121
A.2	Microwave power calibration at 5 T.	121
A.3	Microwave power calibration at 7 T.	121

B.1	X-band ESR spectrometer calibration curve.	123
B.2	UV radicals ¹²⁹ Xe DNP microwave spectra.	124
D.1	Polarization time constant as a function of Xe concentration.	141
D.2	Supplementary inhomogeneous ¹²⁹ Xe solid state spectra.	142
D.3	¹²⁹ Xe <i>FWHM</i> vs ¹ H spins density of the solvent.	144

List of Tables

2.1	Spins quantum number and gyromagnetic ratio.	10
3.1	Relevant spin Hamiltonian interactions.	38
4.1	Different fields ESR and NMR frequencies.	63
4.2	Summary of experimental results.	66
5.1	Sodium [1- ^{13}C]acetate dissolution-DNP with UV-radicals.	97
6.1	Xenon solvents physico-chemical properties.	102
D.1	2-methyl-1-pentanol xenon samples polarization time constants.	140
D.2	2-methyl-1-propanol xenon samples polarization time constants.	140
D.3	Ethanol xenon samples polarization time constants.	140
D.4	^{129}Xe line width study.	144

Chapter 1

Introduction

"Dubium sapientiae initium."

R. Descartes

1.1 Context

Nuclear magnetic resonance (NMR) was discovered by I. I. Rabi in 1938 [119]. With its two main applications, magnetic resonance spectroscopy (MRS) and imaging (MRI), NMR plays nowadays a crucial role in many different fields. MRS is considered one of the most powerful analytic techniques due to the detailed information that can be obtained concerning, for instance, molecular and macromolecular structures, dynamic processes, chemical reactions and living tissues. MRI is a medical diagnostic technique characterized by high anatomic spatial resolution and a plurality of image contrast mechanisms able to highlight, as appropriate, different pathologies. Moreover, since no ionizing radiations are involved, MRI is completely non invasive in contrast to other diagnostic techniques such as CT (computed tomography) and PET (positron emission

tomography). However, all these applications suffer of a lack of sensitivity that entails, in most of the cases, experiments characterized by long acquisitions and thus a poor time resolution. The NMR signal is proportional to the nuclear polarization that can be defined as a measure of the nuclear spins order expressed by the entropy of the system [79, 134]. The polarization represents the nuclear spin population difference between distinct Zeeman levels and is the result of two competing energies: the magnetic energy, tending to arrange all spins on the lower energy level, and the thermal energy tending to equipopulate them. At thermal equilibrium the energy levels population follows the Boltzmann distribution and, since the ratio between the magnetic and thermal energy is generally around $10^{-5} - 10^{-6}$, the nuclear polarization is intrinsically low.¹ Although significant technological improvements (such as higher magnetic field, cryo-probes and multichannels probes) increased the NMR sensitivity during the years, hyperpolarization techniques represent the most dramatic way to overcome NMR's main drawback. The general concept behind these experimental strategies is to create a non-equilibrium polarization state forcing all the nuclear spins of a given sample to seat on a single Zeeman level, in order to maximize the population difference. The experimental approach that is currently the most versatile and established in terms of achieving high polarization in a reasonable amount of time and applicability to a large variety of nuclear species is known as dynamic nuclear polarization (DNP).

The idea that electron spins can be used to enhance the polarization of nuclear spins in metals was presented for the first time in a seminal theoretical work by Overhauser and shortly thereafter confirmed experimentally by Craver and Slichter in the early '50s [33, 113]. The same concept was later extended to the case of liquids containing paramagnetic impurities and to paramagnetic ions [2]. As far as we will be concerned in this thesis, the concept of DNP is limited to the case of polarization transfer from electron

¹At 9.4 T and room temperature an ensemble of ^1H nuclei has a polarization of 32 ppm that decreases to 8 ppm for ^{13}C nuclei.

spins of fixed paramagnetic centers to nuclear spins, both embedded in a diamagnetic glassy solid and coupled by dipolar interaction, at low temperature ($1-1.5$ K) and moderate magnetic field ($3.38-7$ T) [4]. This technique first found application in the field of high energy particles physics with the intent of producing "polarized targets", usually consisting of frozen beads of water/alcohol solutions, for performing spin scattering experiments [103]. DNP is also used to increase NMR sensitivity. Besides applications in solid state NMR experiments, already introduced in the '80s [50, 52, 137], DNP was successfully employed, in more recent years, for increasing the polarization of low-gamma nuclei that exhibit a long liquid state longitudinal relaxation-time (T_1) in solutions such as ^{13}C , ^6Li , ^{15}N [44, 63, 138]. This technique, invented by Ardenkjaer-Larsen et al. in 2003, is known as dissolution-DNP [8]. The overwhelming liquid state nuclear polarization enhancement (e.g. > 10000 at room temperature and 9.4 T) turned out to be of primary utility in many MRS applications ranging from real-time enzyme and polymers kinetics [28, 86], to drug discovery from ligands analysis [87], to studies of cell metabolism [89]. Concerning MRI, dissolution-DNP found its most prominent employment in early cancer diagnosis in the picture of what is currently known as metabolic imaging [56]. For instance highlighting the increased pyruvate-to-lactate conversion in breast cancer and lymphoma was made possible thanks to ^{13}C NMR signal enhancement yielded by this technique [45, 61]. Most studies published so far were performed using *Hypersense*TM, a commercial dissolution-DNP instrument working at 3.35 T, and the proprietary trityl radical as source of unpaired electrons for $[1-^{13}\text{C}]$ pyruvic acid hyperpolarization [10, 102]. At the same time several home-made dissolution-DNP machines were developed, working also at higher magnetic field [34, 40, 71], and other most widely available radicals (e.g. BDPA, DPPH, TEMPO, Galvinoxyl) investigated [81, 101, 98, 100, 99]. More recently the possibility to create non-persistent UV-induced paramagnetic centers, suitable for DNP, was also pointed out [49]. The efficiency of

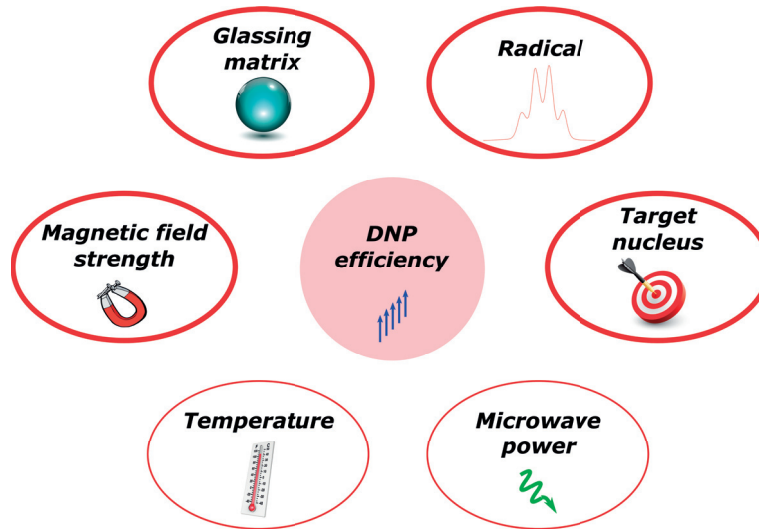


Figure 1.1: Main parameters influencing the DNP mechanism efficiency. Elements surrounded by a thicker line were investigated in the present work.

dissolution-DNP was additionally extended to noble gases: after a minimal modification of the experimental procedure, Comment et al. managed to produce HP ^{129}Xe at room temperature and atmospheric pressure (sublimation-DNP) [41].

1.2 Aim of the thesis

The development of the dissolution-DNP technique has led to renewed interest in the theoretical models to elucidate details concerning the mechanism generating the out-of-equilibrium nuclear polarization. Especially for experimental conditions routinely achieved in dissolution-DNP experiments, where the electron polarization is close to unity and the radical electron spin resonance (ESR) line is characterized by pronounced g-anisotropy, all main theoretical works have been developed about thirty years ago and a generally applicable theory is not acknowledged [3]. The goal of the thesis is to experimentally investigate the principal parameters influencing the electron-to-nuclei polarization transfer, especially at high magnetic field (5 T and 7 T). Hardware as well as sample composition can have strong influence on the absolute DNP enhancement

and polarization time. Four main features were taken under consideration: the effect of the strength of the magnetic field, the species and concentration of the nucleus of interest (target nucleus), the efficiency of a new kind of endogenous non-persistent radical induced by UV-illumination [49] and the role of the glassing matrix in which the radical and the nuclear species to hyperpolarize are embedded (see Figure 1.1).

1.3 Structure of the thesis

Generally speaking, all the main elements suitable for the understanding of the work accomplished during the thesis are presented in Chapters 2 and 3, while Chapters 4 to 6 contain the core of the manuscript and deal with the four main subjects investigated. After an overview of the concept of polarization and the different hyperpolarization techniques, the main aspects characterizing dissolution-DNP are reported in Chapter 2. Chapter 3 pictures the theoretical background of the thesis. First, basic interactions and relevant parameters of an ideal DNP system are presented; then the main classic DNP mechanism involved in dissolution-DNP condition, "Thermal Mixing" (TM), is treated in both high and low temperature cases. In Chapter 4, the effect of the strength of the magnetic field on the DNP performances in the case of "broad-line" radicals is studied on a standard sample containing TEMPOL and sodium $[1-^{13}\text{C}]$ acetate. Big emphasis is given to the validity of the Borghini model in the picture of "Spin Temperature" theory. This project was accomplished in collaboration with the Institute for Molecules and Materials of the Radboud University in Nijmegen (Netherlands) where the measurements at the lower field (3.4 T) were performed. In Chapter 5, the potentiality of non-persistent UV-radicals are investigated in some depth, testing their capability of polarizing different low-gamma nuclear species (^{13}C , ^{129}Xe and ^6Li) and preserving the nuclear polarization under unfavorable HP solution transfer conditions.

The importance of the solvent, constituting the DNP sample glassing matrix, and the concentration of the target nucleus are pointed out in Chapter 6 in the picture of ^{129}Xe sublimation-DNP. Conclusions and perspectives are reported in Chapter 7.

Chapter 2

Hyperpolarization techniques overview

“Order is something artificially imposed; the natural state is chaos”

A. Schnitzler

2.1 Concept of spin polarization and NMR signal

Spin angular momentum, usually called just spin, is an intrinsic property of elementary particles as the mass and the charge [78]. By convention \vec{I} denotes the nuclear spin, result of the coupling between protons and neutrons constituting the nucleus, and \vec{S} the electron one. Let us consider a nucleus with spin quantum number I (what reported in the dissertation that follows applies also to electrons, it is sufficient to replace momentum \vec{I} with \vec{S}). As a consequence of the quantization of the angular momentum, the allowed values of the projection of \vec{I} along a given direction (the z-axis by convention) are $m_I = -I, -I + 1, \dots, I - 1, I$; where m_I represents the magnetic

quantum number. Each nucleus with spin posses a magnetic moment $\vec{\mu}$ given by

$$\vec{\mu}_I = g_n \beta_n \vec{I} = \gamma_I \hbar \vec{I} \quad (2.1)$$

where $\hbar = 1.054 \times 10^{-34} \text{ J} \cdot \text{s}$ and $\beta_n = 5.051 \times 10^{-27} \text{ J/T}$ are the Planck constant divided by 2π and the nuclear magneton respectively, while γ_I and g_n are characteristic of the nuclear species and represent the gyromagnetic ratio and nuclear g-factor.¹ In presence of an external magnetic field $\vec{B}_0 = B_0 \hat{z}$ the magnetic moment interacts with the latter generating what is known as Zeeman effect. The Hamiltonian describing this kind of interaction writes:

$$\mathcal{H}_{NZ} = -\vec{\mu}_I \cdot \vec{B}_0 = -g_n \beta_n I_z B_0 = -\gamma_I \hbar I_z B_0 \quad (2.2)$$

Since I_z can assume only integer or half integer values, the allowed energy states are discrete and characterized by energy values of the kind:

$$E_{m_I} = -\gamma_I \hbar m_I B_0 = -\hbar \omega_I m_I \quad (2.3)$$

where $\omega_I = \gamma_I B_0$ represents the nuclear Larmor frequency; successive Zeeman levels are separated in energy by $\hbar \omega_I$. Indeed the magnetic moment is not statically aligned with the external magnetic field, but it precesses around the z-axis with angular speed ω_I .²

Let us now consider a system of N_I identical, isolated and non interacting nuclear spins I , in thermal equilibrium at a given temperature τ_I . In case no external magnetic field is applied all Zeeman levels are degenerate and so the N_I spins are randomly

¹For a free electron $\vec{\mu}_S = g_e \beta_e \vec{S} = \gamma_S \hbar \vec{S}$ where $g_e = 2.0023$ is the electron g-factor and $\beta_e = 9.274 \times 10^{-24} \text{ J/T}$ the Bohr magneton; for bound electrons the value of the g-factor is affected by the molecular environment and can also assume tensorial form (\tilde{g}).

²The term Larmor frequency is a convention, indeed from the physical quantities point of view ω_I is measured in rad/s. The actual frequency of precession or frequency of resonance is $\nu_I = \omega_I/2\pi$.

oriented in the space. If now $\vec{B}_0 = B_0 \hat{z}$ is "switched on" the spin system is going to evolve into the minimum available energy configuration. Since Zeeman levels characterized by a parallel orientation of $\vec{\mu}_I$ with the field are less energetic, the magnetic moments are going to point preferably in that direction. The polarization $P_I = \langle I_z \rangle / I$ is the degree to which, on average over all N_I nuclei of the system, the nuclear spin angular momentum is aligned with the magnetic field. As already anticipated in Chapter 1, at thermal equilibrium, the spin polarization can be expressed through the Boltzmann distribution:

$$P_{0I} = \frac{1}{I} \frac{\sum_{m_I} m_I \exp(-E_{m_I}/k_B \tau_I)}{\sum_{m_I} \exp(-E_{m_I}/k_B \tau_I)} \quad (2.4)$$

where $k_B = 1.38 \times 10^{-23}$ J/K. In case of spins 1/2 there are only two Zeeman levels corresponding to $m_I = \pm 1/2$ with energy $E_{\pm 1/2} = \mp \hbar \omega_I / 2$, thus (2.4) becomes:

$$P_{0I} = \tanh\left(\frac{\hbar \omega_I}{2k_B \tau_I}\right) = \tanh\left(\frac{\hbar \gamma_I B_0}{2k_B \tau_I}\right) \quad (2.5)$$

It is interesting to analyze two extreme situations characterized by a finite value of B_0 : if the temperature is zero all spins are in the lower energy level because there is no thermal energy trying to destroy the spin alignment created by the magnetic field and the polarization value is 1; if the temperature is infinite the two levels are equipopulated and the polarization is zero. For given experimental conditions (magnetic field and temperature) equation (2.5) is strongly influenced by the value of the gyromagnetic ratio only. Indeed in standard dissolution-DNP conditions (1.2 K and 3.35 T) the polarization of an ensemble of unpaired electron, 1H nuclei and ^{13}C nuclei is respectively 0.9545, 0.0028 and 0.0007. Since for nuclei the magnetic energy is, in most of the cases, much smaller than the thermal one (even for temperatures around 1 K) the high-temperature

Spin species	Spin quantum number	$\gamma/2\pi$ [MHz/T]
e^-	1/2	-28024.952
1H	1/2	42.576
^{129}Xe	1/2	-11.777
^{13}C	1/2	10.705
2H	1	6.536
6Li	1	6.265

Table 2.1: The two characteristic parameters (spin quantum number and gyromagnetic ratio) of the spin species encountered in the thesis are reported.

approximation is often used:

$$P_{0I} = \tanh\left(\frac{\hbar\omega_I}{2k_B\tau_I}\right) \approx \frac{\hbar\omega_I}{2k_B\tau_I} \quad (2.6)$$

In Table 2.1 are listed the main features of the spin species treated in the present work.

Besides the efficiency of the hardware and other features linked to the spectrometer, the NMR signal is strictly linked to the amount of magnetization inducing the electromotive force inside the detection coil (for further information about basics of NMR see [60, 90]). The magnetization \vec{M} is defined as the average magnetic moment per unit volume thus, assuming the N_I nuclear spins to be distributed in a volume V , at thermal equilibrium its modulus writes:

$$|\vec{M}| = \left| \frac{1}{V} \sum_i \vec{\mu}_I \right| = \frac{N_I}{V} \langle (\vec{\mu}_I)_z \rangle = \frac{N_I}{V} \mu_I \tanh\left(\frac{\hbar\omega_I}{k_B\tau_I}\right) \quad (2.7)$$

and it is oriented with the same direction of the magnetic field. So that the maximum available NMR signal can be written:

$$Signal \propto \frac{N_I}{V} \mu_I P_{0I} \quad (2.8)$$

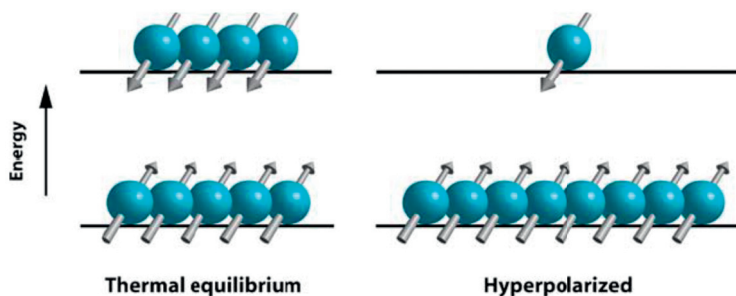


Figure 2.1: Pictorial description of the orientation of the nuclei at thermal equilibrium and in the hyperpolarized state. In the sketch, the magnetic field B_0 is directed vertically upwards and the nuclear gyromagnetic ratio assumed positive [104].

From equation (2.8) follows directly that improving the polarization leads to a linear increase of the signal. Whenever hyperpolarization is mentioned, it is referred to a manipulation of a nuclear spin system ending with one Zeeman energy level highly more populated than the others. Figure 2.1 shows a pictorial representation of the Zeeman levels population for spins $1/2$ at thermal equilibrium and in a HP state. The HP state has, however, a limited lifetime: once the hyperpolarization has been created, the polarization will strive to return to the thermal equilibrium level at a rate governed by the T_1 longitudinal-relaxation time. Nuclear T_1 strongly depends on the chemical structure and environment (magnetic field and temperature) of the hyperpolarized compound. It can typically range from few milliseconds to several hours [90]. Four different methods of hyperpolarization are currently known [55]: brute force approach (BF), spin exchange optimal pumping (SEOP), parahydrogen-induced polarization (PHIP) and DNP.³

2.2 Brute force

Equation (2.5) shows how the thermal equilibrium polarization, and thus the maximum available NMR signal, is an increasing function of B_0/τ_I so the most straightforward

³One could argue that also chemical induced dynamic nuclear polarization (CIDNP) is such a method, although is of very limited utility (see [76] for a deeper dissertation of the topic).

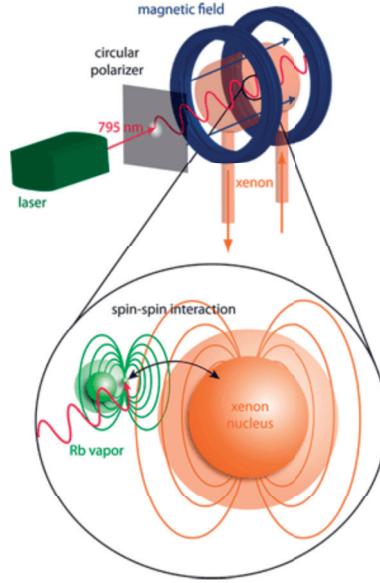


Figure 2.2: Pictorial representation of the SEOP method. In the upper part of the picture is reported the pumping cell where the noble gas is hyperpolarized, in the lower part a pictorial representation of the angular momentum transfer collision between a xenon nucleus and a rubidium atom.

method to improve P_{0I} consists in cooling down (as much as possible) the sample in a strong magnetic fields (as high as possible). Although the method is conceptually simple and applicable to large samples [66], it is rather unpracticable since it presents one main drawback: the polarization time. For instance, assuming to use a 14 T superconductive magnet, in order to achieve a high nuclear polarization (e.g. 0.80 for 1H and 0.20 for ^{13}C), a temperature around 15 mK is required. This temperature has to be maintained for long time because in the above mentioned experimental conditions the nuclear longitudinal relaxation time (T_{1I}) in a diamagnetic material can be hundreds of hours, thus the sample could take several days to reach thermal equilibrium.

2.3 Spin exchange optical pumping

The nuclear spins of ^{129}Xe and other noble gases (such as ^{83}Kr and 3He) can be hyperpolarized to fairly high levels and in short time by SEOP [132]. In this two-

steps process, the electron spin polarization of an alkali metal vapor, such as rubidium, is firstly increased by the absorption of angular momentum from circularly polarized laser light (795 nm). Spin-exchange collisions between the alkali metal atoms and the xenon ones then transfer the angular momentum to the ^{129}Xe nuclear spins through Fermi hyperfine-interaction, resulting in a high non-Boltzmann population distribution of the xenon nuclear Zeeman levels that increases the NMR detection sensitivity (a pictorial representation of the method is reported in Figure 2.2). The two most common approaches to hyperpolarize ^{129}Xe through SEOP are termed "continuous-flow" [64, 123] and "stopped-flow" (usually called also "batch-mode") [112, 122] with respect to the delivery of xenon gas to and from the polarization cell. The nuclear polarization of the noble gas, after a given duration of optical pumping, depends on many parameters such as the electron spin polarization of the alkali atoms, the rate of spin exchange collisions between the latter and the noble gas nuclei and the spin relaxation of both electrons and nuclei. A buffer gas, typically N_2 or ^4He which are chemically inert, is generally added to the xenon/alkali metal gas mixture. The function of the buffer is threefold: spin confinement, pressure broadening of the optical absorption line and quenching of the alkali metals fluorescence [17]. These three factors together allow to efficiently excite the alkali atoms via laser light pumping and keep them polarized until an angular momentum transfer collision with a noble gas atom occurs. Concerning applications, "batch-mode" systems are attractive not only for their relative simplicity, but also because they can operate in a xenon rich regime that obviates the need to separate the polarized xenon from the buffer gas via cryocollection, thus eliminating a potential source of polarization loss [82]. In addition it facilitates applications using quadrupolar noble gas isotopes [126].

2.4 Parahydrogen-induced polarization

The PHIP method can improve nuclear polarization via a chemical reaction (hydrogenation) involving the zero spin configuration of the H_2 molecule (parahydrogen, $p-H_2$, see Figure 2.3A). Bowers and Weitekamp initially predicted and verified that the PHIP effect arises in molecules catalytically hydrogenated with parahydrogen [30, 29]. Differently from other hyperpolarization techniques (e. g. SEOP and DNP), where the coupling between nuclear spin ordering and electron spin degrees of freedom is involved, PHIP may be seen as a coupling, through a chemical reaction, of molecular rotation to nuclear-spin polarization and relies on the strict correlation between rotational states and nuclear spin states which arises in molecules with identical nuclei from the symmetrization postulate of quantum mechanics [30].

Indeed the quantum states of molecular hydrogen, in both gaseous and condensed phases are divisible into two manifolds, orthohydrogen ($o-H_2$) and the above mentioned $p-H_2$, with interconversion between them at a rate usually much slower than the rate of equilibration within each manifold in absence of a catalyst. The requirement that the overall molecular wave function must be antisymmetric with respect to exchange of the two nuclei restricts the rotational states associated to a manifold in a well-known way [121]. In particular $p-H_2$ represents the lowest-energy configuration of the molecule that is separated by the lowest ortho states by a rotational energy quantum equivalent to 190 K, allowing preparation of essentially pure $p-H_2$ at cryogenic temperatures.

The enrichment of parahydrogen represents the first step of the PHIP method. Conventionally it is performed by cooling down hydrogen gas to 77 K (at the equilibrium the amount of $p-H_2$ is around 50 %) in presence of a catalyst (e. g. charcoal) to speed up the conversion process from one spin multiplicity to the other. Decreasing the temperature down to 22 K, just above H_2 's boiling point, the amount of $p-H_2$ is around 100 %, when equilibrium is achieved [110]. As $p-H_2$ and $o-H_2$ are reasonably

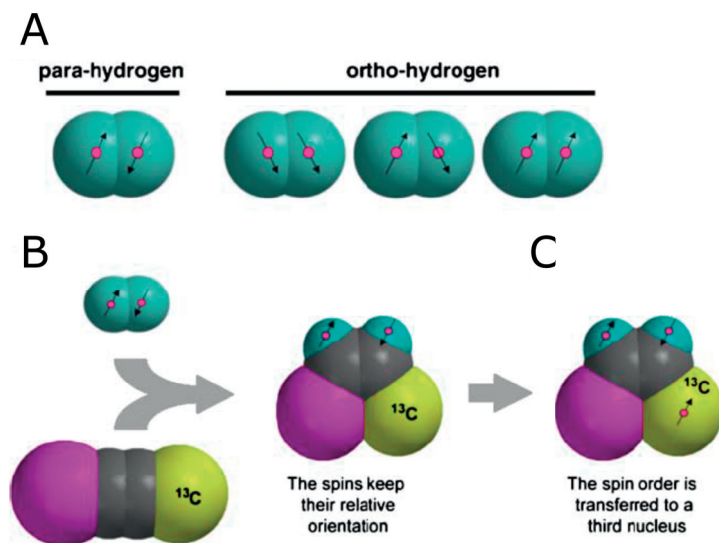


Figure 2.3: The four possible orientations of the nuclear spin in the hydrogen molecule are reported (A). A substrate molecule containing, e.g. ^{13}C is hydrogenated with parahydrogen (B). The spin order of the parahydrogen molecule is converted to nuclear polarization of the ^{13}C nucleus via a diabatic-adiabatic field cycling scheme or by a sequence of radiofrequency pulses (C) [104].

stable in absence of a catalyst, the gas can be successively warmed up without a change of spin state. At this stage of the process H_2 molecules possess a large spin order (spin entropy close to zero), but $p-H_2$ has no NMR signal, since the spin angular momentum of the system is zero.

In order to transform this spin order into useful NMR polarization the magnetic symmetry of the H_2 molecule must be broken [30]. The second step (i. e. molecular addition) of the PHIP method deals with this issue: $p-H_2$ is added to another molecule through a catalyst induced hydrogenation reaction. The coupling with other nuclei and the new electronic environment (i. e. different chemical shifts) allow to treat the two $p-H_2$ hyperpolarized protons separately from the NMR point of view. A requisite is that the hydrogenation mechanism operates by transfer of the hydrogen molecule as a unit onto the substrate (see Figure 2.3B). The non-equilibrium spin order of the nascent protons of the parahydrogen molecule can be directly used for

imaging applications [26] or intramolecularly transferred to longer-lived lower-gamma nuclei of the substrate, either by means of diabatic–adiabatic field cycling [54, 73] or by a sequence of radio frequency pulses [74] (see Figure 2.3C). The technique, despite its capability to increase the nuclear polarization by several orders of magnitude in a really short time (few seconds after the hydrogenation reaction has been completed), is generally limited to ^{13}C and hyperpolarization of specific organic molecules because the hydrogenation reaction is the key point of the technique and it is therefore most efficient in substrates including mainly double or triple $\text{C} - \text{C}$ bonds [104]. Recently, an extension of this method to hyperpolarize a larger variety of molecules has been proposed [7].

2.5 Dissolution-DNP: a practical approach

A detailed description of the physical mechanisms through which the highly out of equilibrium nuclear polarization is obtained, in dissolution-DNP conditions, will be given in Chapter 3. We here aim at introducing the technique mostly from a practical point of view, in order to highlight the main features affecting the efficiency of the process.

In principle, each molecule containing a NMR sensitive nucleus ($I \neq 0$) can be successfully polarized via DNP. The basic idea is to enhance the nuclear spin polarization by driving highly polarized unpaired electron spins out of thermal equilibrium, by means of slightly off-resonance microwave irradiation with respect to the electron Larmor frequency. Thus, cross-polarization between electrons and their surrounding nuclei allows to transfer the spin order to the latter. The two essential parameters determining the DNP efficiency are the electron spin longitudinal relaxation time T_{1S} and the thermal equilibrium electron spin polarization P_{0S} . At first approximation, the

nuclear spin longitudinal relaxation time T_{1I} is not an independent parameter because it is directly proportional to T_{1S} , as the main relaxation mechanism of the nuclear spins is dipolar coupling to the unpaired electron spins [42]. Ideally, P_{0S} should be as large as possible, since it represents the theoretical upper limit of the achievable maximum nuclear polarization [4], and T_{1S} sufficiently long to allow an efficient saturation of the ESR line (see Section 3.3.1) with a minimal amount of microwave power, thereby avoiding excessive sample heating. The latter effect is facilitated if the unpaired electron spins are homogeneously distributed inside the sample with random orientations even between nearest neighbors. Such a configuration yields strong dipolar couplings between electron spins that are spectrally far apart facilitating spectral diffusion [71] (see Section 3.3.1).

In Chapter 1 (see Figure 1.1), it was pointed out that the achievement of these conditions depends on the optimization of six main features: the species and concentration of the target nucleus to hyperpolarize; the species and concentration of the radical (electron paramagnetic agent, EPA); the nature of the glassing matrix; the temperature; the strength of the magnetic field; the microwave irradiation.

2.5.1 Sample preparation

The DNP sample is made of three components: the substrate bearing the target nucleus, the electron paramagnetic agent (or its precursor in case of photo-induced radicals) and, unless the molecule of interest is self-glassy when frozen, a so-called "glassing solvent". The sample is first prepared in the liquid state, carefully mixing the above mentioned components, and then, before transfer to the DNP-polarizer, frozen in liquid nitrogen. The role played by the solvent is fundamental because the solid sample has to be characterized by an amorphous glassy structure. Indeed a random distribution of the radicals cannot be achieved in a polycrystalline sample because the paramagnetic centers

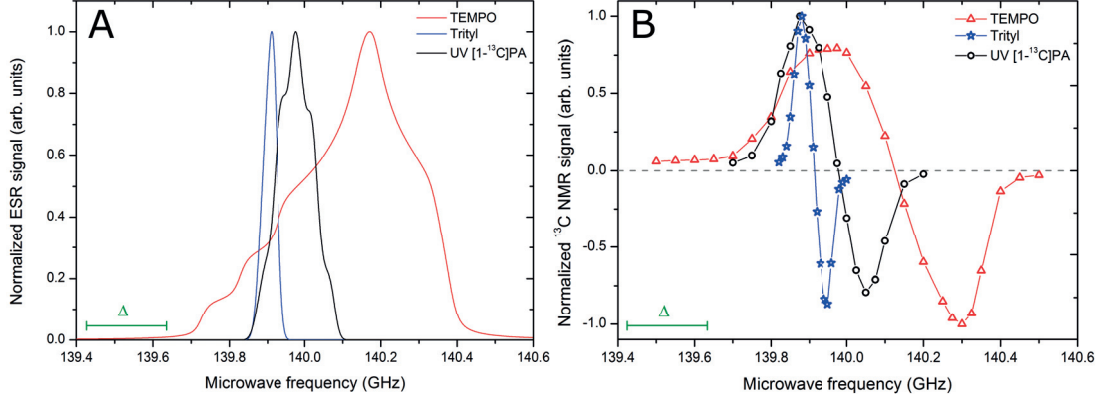


Figure 2.4: (A) Calculated ESR spectrum at 5 T of 6.0×10^{18} spins/cm³ OX063 trityl radical (blue stars), UV-irradiated neat $[1 - ^{13}\text{C}]$ pyruvic acid generating a radical concentration of about 1.1×10^{19} spins/cm³ (black circles), and 3.0×10^{19} spins/cm³ TEMPO nitroxyl radical (red triangles) assuming a spatial random distribution of the paramagnetic centers. (B) Microwave spectra at 5 T and 4.2 K. Comparison between the microwave spectra measured by ¹³C MR in $[1 - ^{13}\text{C}]$ pyruvic acid doped with 6.0×10^{18} spins/cm³ OX063 trityl radical (blue stars), UV-irradiated neat $[1 - ^{13}\text{C}]$ pyruvic acid generating a radical concentration of about 1.1×10^{19} spins/cm³ (black circles), and a frozen 3 M sodium $[1 - ^{13}\text{C}]$ pyruvate aqueous solution doped with 3.0×10^{19} spins/cm³ TEMPO nitroxyl radical (red triangles). Δ corresponds to the ¹H MR frequency at 5 T.

will migrate to the boundaries of the microcrystals leading to a poor DNP effect [68].

The concentration of the substrate to hyperpolarize is usually around 10^{21} spin/cm³. Higher nuclear spins concentration yield, in general, to faster polarization because of a more efficient spin-diffusion mechanism [96] (see Section 3.3.2). Nevertheless, especially when the substrate appears in the form of salt, a too high presence of the latter in the solution could negatively affect the quality of the amorphous structure of the solid frozen sample. A compromise between the two effects has to be found.

The typical EPA concentration is in the range $10^{18} - 10^{19}$ spins/cm³ depending on the kind of dopant and, to date, trityl radicals and the persistent 1,3-bisdiphenylene-2-phenylallyl (BDPA) radical have proven to be the most efficient agents for polarizing low-gamma nuclei [72, 101]. One of the most important characteristic of a radical in the context of DNP is its ESR line width, which correlates with the width of the frequency dependent nuclear polarization enhancement microwave spectrum (see Figure

2.4). The essential feature behind the high DNP efficiency of "narrow-line" radicals (e.g. trityls) is that their ESR line width is narrower than the 1H resonance frequency at a given magnetic field. As a consequence the probability of enabling electron spins to cross-polarize proton spins under microwave irradiation is very low, increasing the chance of polarization transfer to low-gamma nuclei [42]. Although less efficient, since characterized by a much larger spectrum line width (more than four times the trityl one, see Figure 2.4), the nitroxyl radical TEMPO was used in many studies [81, 71, 34]. More recently a new kind of non-persistent radical was developed [49]. Instead of chemically doping the DNP sample solution (as for trityl, TEMPO or BDPA) the paramagnetic centers are induced directly in frozen pyruvic acid via UV-irradiation at liquid nitrogen temperature. The UV-irradiated pyruvic acid (UV-PA) shows an ESR line width in between TEMPO and trityl (see Figure 2.4), with the additional advantage of quenching at the moment of dissolution.

2.5.2 Experimental conditions

Once the solid state sample is ready it is loaded inside the dissolution-DNP machine. In order to achieve an electron spin polarization suitable for efficient DNP, a moderate magnetic field and low temperature are required. In Figure 2.5 the scenario is pictured at 5 T in the range 0.1 K – 300 K. It is clear that the conditions are much more advantageous at 1 K than at liquid nitrogen temperature (77 K) or room temperature (~ 290 K). Indeed at 1 K P_{0S} is essentially 100% and T_{1S} around 1 s; on the other hand at 77 K the former is only 4% and the latter on the order of few hundreds of microseconds making the saturation of the radical ESR line really challenging even for high microwave power [42]. The situation is even worse at room temperature. Note that the values given for the T_{1S} are only representative, since they refer to nitroxyl radicals at 0.35 T [84]. Nevertheless the same trend was found for other radicals at higher field

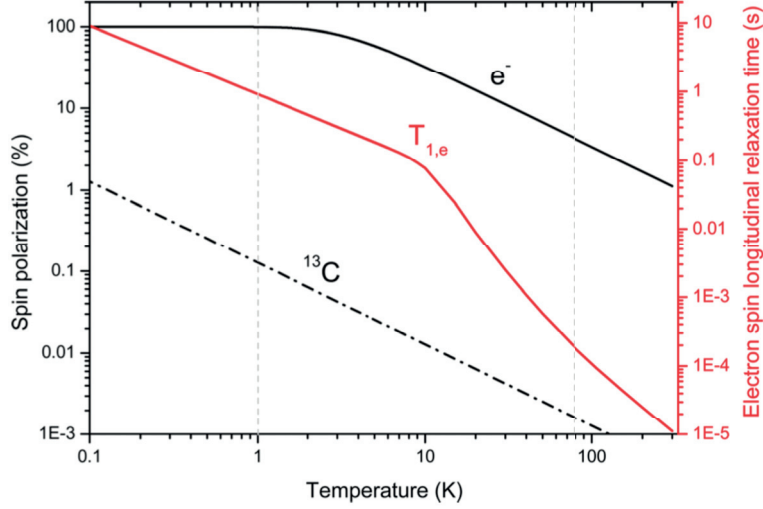


Figure 2.5: ^{13}C (dashed black curve) and electron (solid black curve) spin polarization at 5 T together with the electron spin longitudinal relaxation time (red curve) at 0.35 T as a function of temperature. The relaxation times for nitroxyl radicals were calculated from the fitting curved given in [84]. The graph was taken from [42].

[97]. It is important to notice that reaching and keeping a temperature around 1 K is not that complicated from the technological point of view. The temperature is still "high" enough to just immerse the sample in liquid ^4He at a pressure of ~ 1 mbar. Complicated ^3He dilution cryostats, often employed in the "brute force" method are not required.

The device that allows to work in the desired experimental conditions is called dissolution-DNP polarizer (or "pre-polarizer") and consists of three main hardware components: a superconducting magnet to set the external magnetic field, a helium cryostat connected to a vacuum pumping system to cool the sample to ~ 1 K and a microwave source to enable the polarization transfer from the incorporated electron spins to the surrounding nuclear spins. The original system developed by Amersham Health is reported in Figure 2.6 [8].

Concerning the magnetic field strength, the original dissolution-DNP machine was developed at 3.35 T because microwave sources are readily available at 94 GHz [8, 68].

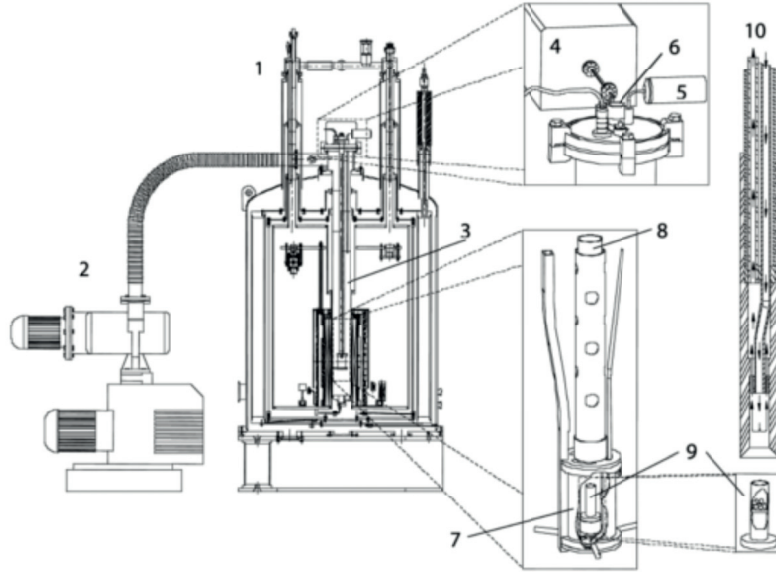


Figure 2.6: Schematic drawing of the original dissolution-DNP polarizer developed by Ardenkjaer-Larsen et al.: (1) DNP polarizer, (2) vacuum pumps, (3) variable-temperature insert, (4) microwave source, (5) pressure transducer, (6) sample port, (7) microwave cavity, (8) sample holder, (9) sample container, (10) dissolution wand [8].

It has been shown that increasing the magnetic field up to 7 T yields to higher nuclear polarization, at least for ^{13}C , using common radicals [34, 71, 72]. According to the scenario described above, besides technological issues such as complicated cryogenics and large microwave losses when the frequency is increased, one would conclude that the higher the field and the lower the temperature, the larger the maximum achievable nuclear polarization. The drawback of working at very high field and low temperature is that the polarization time becomes prohibitively long. Indeed, as we will see in the Chapter 3, the dynamics of the DNP mechanism slows down with a factor $(1 - P_{OS}^2)/B_0^2$ [4]. Increasing the microwave power is not the solution because, if on one hand side the number of photon-electron spin interactions per unit time is increased, speeding up the DNP process, on the other sample heating will negatively affect the polarization efficiency [70]. A temperature of 1 K and a field of 5 T seems to be a good compromise

for dissolution-DNP [42].⁴

2.5.3 The dissolution step

As already mentioned in Chapter 1, the groundbreaking innovation that led, about 10 years ago, to a renewed interest of the scientific community in the DNP process was the addition of a dissolution procedure for producing HP liquid state spectroscopic/imaging agents at physiological temperature [42]. Once the maximum nuclear polarization is achieved in the solid state, dissolution is performed by propelling a hot solvent onto the frozen sample to rapidly melt it. The resulting solution is chased out of the polarizer using pressurized helium gas and collected for injection into an NMR tube, an animal, or more recently a human. A pivotal point that has made dissolution-DNP feasible was the determination of the appropriate environment in which to perform the solid-to-liquid phase transformation. The main problem is that, in general, the nuclear spin-lattice relaxation time T_{1I} of a substrate embedded in a diamagnetic solid doped with paramagnetic impurities becomes really short (down to few ms) when the temperature is increased especially at low magnetic field [1, 42]. Thus, the key for an efficient dissolution, limiting polarization losses, is to melt the frozen solid sample almost instantaneously in a region with a rather strong magnetic field. In practical terms that means performing dissolution directly inside the cryostat (just above liquid helium), employed for reaching the DNP working temperature, in the magnetic field of the polarizer using a large (compared to the solid state sample) volume of super-heated solvent with a big heat capacity (water represents the solvent with the highest specific heat capacity that is liquid at room temperature). In that way it is possible to transform, in less than 1 s, the HP frozen glassy block in a diluted liquid state solution, limiting interactions

⁴The dissolution-DNP hyperpolarizer for clinical use SPINlab, developed by GE Healthcare operates at 0.8 K and 5 T.

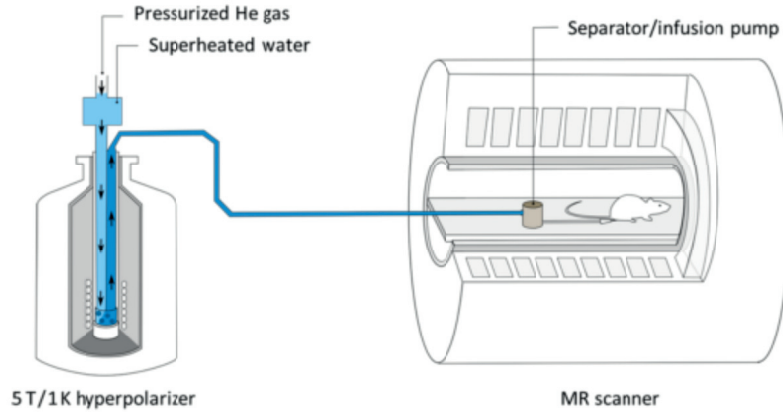


Figure 2.7: Sketch of the dissolution-DNP setup installed at the Center for Biomedical Imaging (CIBM) of the EPFL. A 5 T, 1 K polarizer is located ~ 4 m from a 9.4 T rodent MR scanner. A specific device (infusion pump/separator) minimizing the delay between dissolution and infusion of the HP substrate in the test subject has been implemented for *in vivo* applications. The delay can be as short as 3 s [42].

between HP nuclei and paramagnetic centers (the distances between them are now increased), thus slowing down the relaxation processes.

Once the HP solution is ready, it has to be transferred from the DNP polarizer into the bore of the MR system where the HP spectroscopy/imaging experiment is performed. During the path between the two magnets the HP nuclear spins will usually experience drastic magnetic field variations crossing regions where T_{1I} might be extremely short. For this reason, it is of primary importance to keep the distance between the two systems as short as possible and to perform the transfer as fast as possible.

The T_{1I} is influenced by the chemical environment of the nuclear spins, the magnetic field and the temperature. The main feature is not to cross regions characterized by very strong magnetic field gradients or zero field spots that would reduce the nuclear polarization. Concerning the temperature, in order to minimize relaxation prior to injection, a good strategy can be to quickly stabilize the HP liquid sample's temperature using a massive receiver maintained at an optimal value (in Figure 2.7 is reported the

HP solution transfer set-up routinely used in our lab for *in vivo* applications) [35, 40]. The chemical environment can be partially controlled using an appropriate solvent (e.g. using D_2O instead of H_2O minimizes the nuclear dipolar relaxation in solutions) and/or scavenging the radical after dissolution [105].

Chapter 3

Theoretical background

“It doesn’t matter how beautiful your theory is, it doesn’t matter how smart you are. If it doesn’t agree with experiments, it’s wrong.”

R. Feynman

3.1 Introduction

The aim of the present chapter is to give a description of the physical interactions characterizing a nuclear spins system embedded in an amorphous diamagnetic solid with small concentration of paramagnetic centers at moderate magnetic field and low temperature with the contingent presence of microwave irradiation. The subject is restricted to the pertinent information for the understanding of the DNP process. Section 3.2 deals with the Hamiltonian of the spin system. Section 3.3 is about relaxation processes and the effect of microwave irradiation. In the last section the classic theory of DNP is presented; the theoretical dissertation is restricted to the mechanism known

as "Thermal Mixing" (TM), active in case of "broad-line" radicals with non-negligible dipolar coupling.

3.2 The spin Hamiltonian

Let us consider a system composed by N_S electron spins and N_I nuclear spins per unit volume, assumed all of the same species and such as $N_I/N_S = m \approx 1000$, immersed in a static magnetic field $\vec{B}_0 = B_0 \hat{z}$ (the interaction with the lattice is neglected for the moment). For simplicity we normalize to one single electron spin \vec{S} and we take into account the interaction with the surrounding nuclear spins \vec{I}_k ; the interactions among nuclear spins themselves are also considered. The time independent Hamiltonian of the system writes [125]:

$$\begin{aligned} \mathcal{H}_0 &= \mathcal{H}_{EZ} + \mathcal{H}_{ZFS} + \mathcal{H}_{HF} + \mathcal{H}_{NZ} + \mathcal{H}_{NQ} + \mathcal{H}_{NN} \\ &= \beta_e \vec{B}_0 \cdot \tilde{g} \cdot \vec{S} + \vec{S} \cdot \tilde{D} \cdot \vec{S} + \sum_{k=1}^m \vec{S} \cdot \tilde{A} \cdot \vec{I}_k - \beta_n g_n \sum_{k=1}^m \vec{B}_0 \cdot \vec{I}_k + \sum_{k=1}^m \vec{I}_k \cdot P \cdot \vec{I}_k + \sum_{j \neq k} \vec{I}_j \cdot \tilde{d}_{jk} \cdot \vec{I}_k \quad (3.1) \end{aligned}$$

The different terms in equation (3.1) represent, in the order, the electron Zeeman interaction, the zero-field splitting, the hyperfine coupling of the electron spin and the m nuclear spins, the nuclear Zeeman interaction, the nuclear quadrupolar interaction and the nuclear spin-spin interaction.

3.2.1 Electron and nuclear Zeeman interaction

We explain here in more detail what was briefly introduced in Section 2.1. The interaction between the unpaired electron spin of a radical and the external magnetic field $\vec{B}_0 = B_0 \hat{z}$ expressed in an arbitrary coordinate frame is given by the electron Zeeman

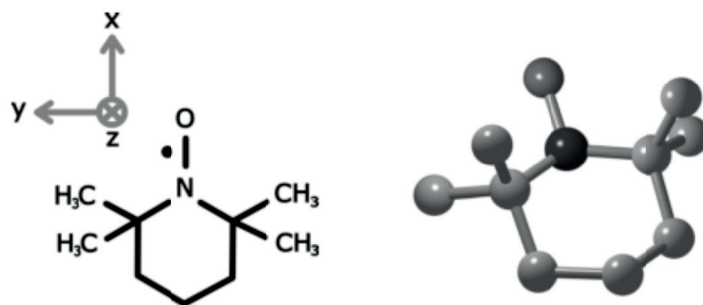


Figure 3.1: Drawing of the TEMPO free radical. The molecule is drawn in 2-D on the left with its molecular axis, and in 3-D on the right. The molecule is neither axial symmetric nor planar, so its \tilde{g} and \tilde{A} tensor result to have orthorhombic symmetry: $g_x \neq g_y \neq g_z$ and $A_x \neq A_y \neq A_z$.

term

$$\mathcal{H}_{EZ} = \beta_e \vec{B}_0 \cdot \tilde{g} \cdot \vec{S} \quad (3.2)$$

For a spin $S = 1/2$ at moderate magnetic field, the Zeeman term represents the dominant interaction characterizing the radical ESR spectrum. Most of the time \mathcal{H}_{EZ} is anisotropic; meaning that its expectation value, the Zeeman energy, depends on the spatial orientation of the paramagnetic center with respect to the magnetic field. This feature is expressed by \tilde{g} that is a symmetric 3×3 second order tensor. Thus \tilde{g} , fixed the reference frame, can always be written in diagonal form characterized by the three principal values g_x , g_y and g_z . Usually the \tilde{g} principal axes frame is considered as the molecular frame of the radical and all interaction tensors are referred to this frame (see Figure 3.1). For a non-degenerate electronic ground state the orbital angular momentum is quenched ($L = 0$). The deviation of the principal values from the g_e value of the free electron spin and the orientation dependence of the electron Zeeman term is determined by the interaction between the electron spin \vec{S} and the orbital angular momentum \vec{L} from the excited states, known as spin-orbit interaction. Since for most organic radicals the excited states are high in energy, the spin-orbit coupling is weak and, in general, the principal values of \tilde{g} deviate by less than $\Delta g = 0.01$ from g_e [125].

The interaction of one nuclear spin I with an external magnetic field $\vec{B}_0 = B_0 \hat{z}$ is given by equation (2.2). For protons, the nuclear Zeeman interaction is only $1/685$ of the electron one, and for all other nuclear species, it is even less. In the present work, for simplicity, the nuclear Zeeman interaction will be considered as isotropic. Thus, g_n will assume the form of a proportionality factor rather than a tensor as in the electronic case.

3.2.2 Hyperfine interaction

The hyperfine interaction between an electron and a nuclear spin given by the Hamiltonian

$$\mathcal{H}_{HF} = \vec{S} \cdot \tilde{A} \cdot \vec{I} \quad (3.3)$$

represents one of the most important sources of information that can be understood from the observation of an ESR spectrum as regarding the paramagnetic species molecular structure. The hyperfine tensor \tilde{A} is the sum of two contributions: the isotropic Fermi contact interaction \mathcal{H}_{HF} and the electron-nucleus dipole-dipole coupling \mathcal{H}_{DD} . The Fermi contact interaction writes

$$\mathcal{H}_F = a_{iso} \vec{S} \cdot \vec{I} \quad (3.4)$$

where, introducing the vacuum permeability constant $\mu_0 = 4\pi \times 10^{-7} \text{ H/m}$,

$$a_{iso} \propto \mu_0 \hbar^2 \gamma_e \gamma_n |\psi_0(0)|^2 \quad (3.5)$$

is the isotropic hyperfine coupling constant and $|\psi_0(0)|^2$ is the electron spin density probability at the nucleus site.

The electron-nuclear dipole-dipole coupling is described by

$$\mathcal{H}_{DD} = \frac{\mu_0}{4\pi} \frac{\hbar^2 \gamma_S \gamma_I}{r^3} \left[\vec{S} \cdot \vec{I} - 3 \frac{(\vec{S} \cdot \vec{r})(\vec{I} \cdot \vec{r})}{r^2} \right] \quad (3.6)$$

where \vec{r} , representing the vector connecting the electron and nuclear spins, has an orientation dependence from the two polar angles θ and ϕ (the z-axis is assumed always parallel to magnetic field). Integration over the spatial electron distribution allows to calculate the anisotropic dipolar coupling tensor \tilde{T} so that

$$\mathcal{H}_{DD} = \vec{S} \cdot \tilde{T} \cdot \vec{I} \quad (3.7)$$

As in the case of the \tilde{g} tensor also the \tilde{T} tensor can be always expressed in diagonal form characterized by the three principal values T_x , T_y and T_z . Since the scalar nature of \mathcal{H}_F , the same applies to \tilde{A} , identified by the three principal values A_x , A_y and A_z .

It is important to underline two main features about the hyperfine interaction: it is magnetic field independent and strongly affected by the distance between the electron and nuclear spins. As far as we will be concerned in this work only the nuclear spins in close vicinity to the unpaired electron (e.g. the nuclei composing the radical molecule) will be taken into account concerning the interpretation of the ESR spectra.

3.2.3 Zero-field splitting

For electron spin systems with effective spin $S > 1/2$ and non-cubic symmetry, the dipole-dipole coupling between the electron spins lifts the $(2S + 1)$ degeneracy of the ground state. This interaction is field independent and is known as zero-field splitting.

The related Hamiltonian assumes the form:

$$\mathcal{H}_{ZFS} = \vec{S} \cdot \tilde{D} \cdot \vec{S} \quad (3.8)$$

where D is the symmetric and traceless zero-field interaction tensor. In the principal axes system of the \tilde{D} tensor equation (3.8) can be written as

$$\mathcal{H}_{ZFS} = D_x S_x^2 + D_y S_y^2 + D_z S_z^2 = D \left[S_z^2 - \frac{1}{3} S(S+1) \right] + E (S_x^2 - S_y^2) \quad (3.9)$$

with $D = 3D_z/2$ and $E = (D_x - D_y)/2$. At X-band frequencies (~ 9.5 GHz) the zero-field splitting is often the main magnetic interaction in systems with $S > 1/2$ [125].

3.2.4 Nuclear quadrupole interaction

Nuclei with spin $I \geq 1$ are characterized by a non-spherical charge distribution expressed by the nuclear electrical quadrupole moment Q ; the charge distribution interacts with the electric field generated by nuclei and electrons in close proximity and the relative Hamiltonian writes:

$$\mathcal{H}_{NQ} = \vec{I} \cdot \tilde{P} \cdot \vec{I} \quad (3.10)$$

where \tilde{P} is the nuclear quadrupole tensor. In its principal axis system \tilde{P} is traceless and can be written as

$$\mathcal{H}_{NQ} = P_x I_x^2 + P_y I_y^2 + P_z I_z^2 = \frac{e^2 q Q}{4I(2I-1)} [(3I_z^2 - I(I+1)^2) + \eta (I_x^2 - I_y^2)] \quad (3.11)$$

where e is the elementary charge, eq the electric field gradient and $\eta = (P_x - P_y)/P_z$ the asymmetry parameter. The two quantities, usually reported in the literature, char-

acterizing the nuclear quadrupole interaction, are its strength e^2qQ and the asymmetry η .

3.2.5 Nuclear dipolar interaction

The dipole-dipole interaction between m like nuclear spins I is a special case of equation (3.6), the Hamiltonian writes [1]:

$$\mathcal{H}_{NN} = \sum_{j \neq k} \vec{I}_j \cdot \tilde{d}_{jk} \cdot \vec{I}_k = \frac{\mu_0}{4\pi} \sum_{j \neq k} \frac{\hbar^2 \gamma_I^2}{r_{jk}^3} \left[\vec{I}_j \cdot \vec{I}_k - 3 \frac{(\vec{I}_j \cdot \vec{r}_{jk})(\vec{I}_k \cdot \vec{r}_{jk})}{r_{jk}^2} \right] \quad (3.12)$$

The nuclear dipole-coupling tensor \tilde{d}_{ik} , too small to be resolved on the ESR scale, provides one of the main sources of information in solid state NMR and, describing the vector \vec{r}_{jk} joining the nuclear spins j and k through the polar angles θ and ϕ , can be expressed as:

$$\tilde{d}_{jk} = \frac{\mu_0}{4\pi} \frac{\hbar^2 \gamma_I^2}{r_{jk}^3} [A + B + C + D + E + F] \quad (3.13)$$

where

$$\begin{aligned} A &= I_{j,z} I_{k,z} (1 - 3 \cos^2 \theta) \\ B &= -\frac{1}{4} (1 - 3 \cos^2 \theta) (I_{j,+} I_{k,-} + I_{j,-} I_{k,+}) = \frac{1}{2} (1 - 3 \cos^2 \theta) (\vec{I}_{j,z} I_{k,z} - \vec{I}_j \cdot \vec{I}_k) \\ C &= -\frac{3}{2} \sin \theta \cos \theta \exp(-i\phi) (I_{j,z} I_{k,+} + I_{k,z} I_{j,+}) \\ D &= -\frac{3}{2} \sin \theta \cos \theta \exp(i\phi) (I_{j,z} I_{k,-} + I_{k,z} I_{j,-}) \\ E &= -\frac{3}{4} \sin^2 \theta \exp(-2i\phi) I_{k,+} I_{j,+} \\ F &= -\frac{3}{4} \sin^2 \theta \exp(2i\phi) I_{k,-} I_{j,-} \end{aligned} \quad (3.14)$$

In equations (3.14) the only terms of the dipolar-coupling tensor \tilde{d}_{ik} that commute with the nuclear Zeeman Hamiltonian \mathcal{H}_{NZ} are A and B . The latter are called secular terms

and, according to first order perturbation theory, are responsible of the broadening of the nuclear Zeeman levels. Without any dipolar-coupling all the m nuclear spins would resonate at $\omega_I = \gamma_I B_0$. In presence of dipolar interaction the secular terms add a contribution to the static magnetic field \vec{B}_0 called dipolar local field $B_{l,II}$ whose direction and intensity depends on the spins distribution. Thus, the nuclei are going to resonate in a frequency range $\Delta\omega_I$ around ω_I given by $\Delta\omega_I = \gamma_I B_{l,II}$. Moreover the B term in equation (3.14) allows also an energy conserving simultaneous reversal of two neighboring spins in opposite direction. As we will see in the next section this mechanism called, "flip-flop" transition, is responsible of the phenomenon known as nuclear spin-diffusion. Terms C , D and E , F are responsible, respectively, for those interactions that expect the spin-flip of one nuclear spin only and two nuclear spins in the same direction simultaneously. Those terms do not commute with the nuclear Zeeman Hamiltonian \mathcal{H}_{NZ} so, at the first order, they have no influence on the NMR line shape and are not going to be considered here. The truncated form of the homonuclear dipolar coupling writes:

$$\mathcal{H}'_{NN} = \frac{\mu_0}{4\pi} \sum_{j \neq k} \frac{\hbar^2 \gamma_I^2}{r_{jk}^3} [A_{jk} + B_{jk}] = \frac{\mu_0}{4\pi} \sum_{j \neq k} \frac{\hbar^2 \gamma_I^2}{r_{jk}^3} \frac{1}{2} (1 - 3 \cos^2 \theta_{jk}) \left(3I_{j,z}I_{k,z} - \vec{I}_j \cdot \vec{I}_k \right) \quad (3.15)$$

A fair estimation of the NMR line width $\Delta\omega_I$ is the square root of the homogeneous second moment $M_{2II,hom}$ [1]:

$$\Delta\omega_I = \gamma_I B_{l,II} \approx \delta_{II} \quad (3.16)$$

where $\delta_{II} = \sqrt{M_{2II,hom}}$. The dipolar contribution given by \mathcal{H}'_{NN} to the NMR line second moment can be evaluated through the Van Vleck formula and writes [1, 131]:

$$M_{2II,hom} = \frac{3}{4} \left(\frac{\mu_0}{4\pi} \right)^2 \hbar^2 \gamma_I^4 I(I+1) \sum_k \frac{(1 - 3 \cos^2 \theta_{jk})^2}{r_{jk}^6} \quad (3.17)$$

3.2.6 DNP system approximations

As far as we will be concerned we are going to deal with ensembles of low-gamma NMR active nuclear spins ($\sim 10^{21}$ spins/cm³) embedded in a glassy diamagnetic solid ($\sim 10^{22}$ spins/cm³ of 1H and/or 2H nuclei) with small concentrations ($\sim 10^{19}$ spins/cm³) of organic radicals at moderate magnetic field and low temperature.

From the ESR point of view all paramagnetic centers are fixed and randomly oriented in space. For the values of the magnetic field investigated in the present work (3.4 T – 7 T) the main electron interaction is the Zeeman followed by the hyperfine one. The ESR line, looking like an inhomogeneously broadened powder spectrum, is the result of the superposition of several "spin packets" with distinct Larmor frequencies (see Section 3.3.1), which do not change in time. The position of the resonances is spread around the center of gravity ω_{0S} of the line shape function $f(\omega)$ defined as

$$1 = \int_{-\infty}^{+\infty} f(\omega) d\omega \quad (3.18)$$

$$\omega_{0S} = \int_{-\infty}^{+\infty} \omega f(\omega) d\omega \quad (3.19)$$

while its width is parameterized through the square root of the inhomogeneous second moment $M_{2,inhom}$

$$M_{2,inhom} = \int_{-\infty}^{+\infty} (\omega - \omega_{0S})^2 f(\omega) d\omega \quad (3.20)$$

Equation (3.1) was normalized to one single electron spin. In the systems we are going to study the coupling between the paramagnetic centers, homogeneously dispersed in the glassy matrix, is not negligible. The electron spin-spin coupling Hamiltonian is composed by two parts: the exchange coupling and the electron-electron dipolar-coupling such as

$$\mathcal{H}_{EE} = \mathcal{H}_{ex} + \mathcal{H}_{SS} \quad (3.21)$$

The first term of equation (3.21) starts to be observable in solids for distances between electron spins shorter than 1.5 nm [125]. The second term is the same reported in equation (3.12) written for electron spins. The Van Vleck formula (3.17) can be used for evaluating the homogeneous broadening of a spin packet. A rough estimation of $M_{2SS, hom}$ is obtained by assuming r_{jk} to follow a Poissonian distribution. The probability of finding no other electron spins within a distance r_{jk} from a given one S_j is $\exp(-4/3\pi N_S r_{jk}^3)$ where N_S represents the electron spin concentration per unit volume. Setting this probability to 1/2 the average distance between first neighboring paramagnetic centers results to be [67]

$$r_{e-e} \simeq 0.55 N_S^{-1/3} \quad (3.22)$$

Since the free radicals are randomly oriented, the $(1 - 3\cos^2\theta_{jk})^2$ factor in (3.17) can be averaged over θ from 0 to π . Assuming $S = 1/2$ the Van Vleck formula becomes [1]

$$M_{2SS, hom} = \delta_{SS}^2 = \frac{9}{20} \left(\frac{\mu_0}{4\pi}\right)^2 \hbar^2 \gamma_S^4 \frac{1}{r_{e-e}^6} \simeq 16 \left(\frac{\mu_0}{4\pi}\right)^2 \hbar^2 \gamma_S^4 N_S^2 \quad (3.23)$$

Written in frequency units equation (3.23) gives $\Delta\omega_S \approx \delta_{SS} = 1.3 \times 10^{-12} N_S$ Hz with N_S expressed in spins/cm³ i.e. 13 MHz every 10¹⁹ spins/cm³. The latter represents the main contribution to the broadening of each electron spin packet because, according to the radical concentration range considered in DNP experiments, the exchange coupling can be neglected since the average distance between first neighboring paramagnetic centers r_{e-e} is larger than 3 nm.

All the calculated or fitted ESR spectra we are going to encounter in next chapters were evaluated using the PEPPER routine (for powder spectra) of the MATLAB-based software Easyspin [128] considering only $S = 1/2$ electron spin systems including Zeeman interaction, hyperfine interaction with the nuclei composing the radical molecule,

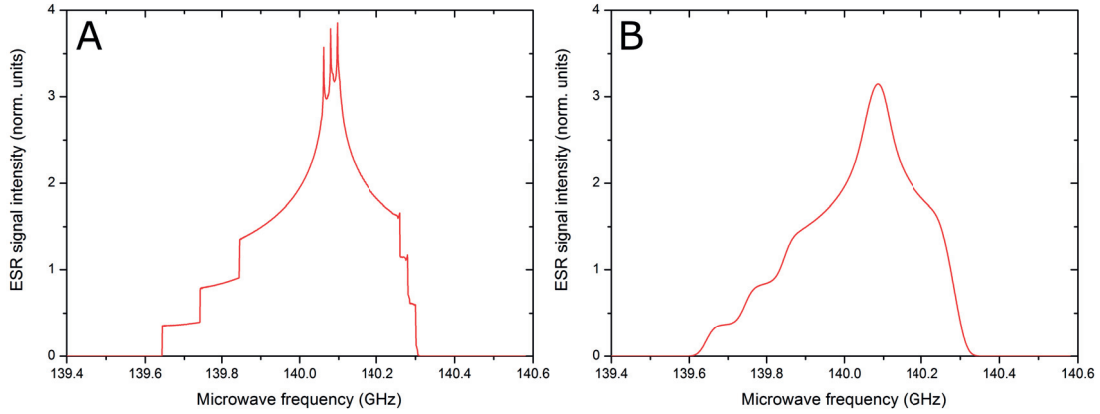


Figure 3.2: Calculated TEMPO radical ESR spectrum at 5 T without electron-electron dipolar broadening (A) and with a "phenomenological" electron-electron dipolar broadening expressed as a convolution of the powder spectrum with a Gaussian line of 39 MHz FWHM, corresponding to a radical concentration of 3.0×10^{19} spins/cm³ (B). For both spectra the square root of the inhomogeneous second moment $M_{2,inhom}$ resulted to be 148 MHz.

and a "phenomenological" electron-electron dipolar broadening expressed as a convolution of the powder spectrum with a Gaussian line width equal to $\Delta\omega_S$ (only in one case the zero-field splitting of a $S = 1$ spin system was taken into account and resulted in a negligible contribution, see Chapter 5). The effect of the dipolar-broadening on a powder spectrum is reported in Figure 3.2 in the case of TEMPO radicals. The spectra at 5 T were calculated using the following parameters [53]: $\tilde{g} = [2.0094; 2.0065; 2.0017]$; $\tilde{A} = [20.48; 17.68; 101.00]$ MHz related to the interaction with the ^{14}N nucleus sharing the same molecular site as the unpaired electron; moreover, for the spectrum reported in panel B, a 39 MHz dipolar-broadening was added. The square root of the inhomogeneous second moment $M_{2,inhom}$ resulted to be 148 MHz confirming that for such a value of the magnetic field, the radical ESR spectrum is dominated by the anisotropy of the Zeeman and hyperfine interactions. Nevertheless the homogeneous dipolar-broadening plays a fundamental role in the phenomenon known as "spectral diffusion" and thus, as we will see, the establishment of a homogeneous spin temperature across the ESR line under microwave irradiation (see Section 3.4).

Concerning the NMR spectrum analysis relative to the DNP target nuclear species (^{13}C , ^6Li and ^{129}Xe), besides the nuclear Zeeman interaction that determines the Larmor frequency, only the heteronuclear dipolar coupling was considered for investigating the effect of the solvent constituting the glassing matrix. The homogeneous broadening for unlike spins can be evaluated by means of a modified version of the Van Vleck formula since in equation (3.14) only term A commutes with the nuclear Zeeman Hamiltonian (the flip-flop term does not conserve the energy this time). The broadening observed on nuclear spin species I caused by nuclear spin species I' can be written [1]

$$M_{2II',hom} = \frac{1}{3} \left(\frac{\mu_0}{4\pi} \right)^2 \hbar^2 \gamma_I^2 \gamma_{I'}^2 I' (I' + 1) \sum_{k'} \frac{(1 - 3 \cos^2 \theta_{jk'})^2}{r_{jk'}^6} \quad (3.24)$$

Moreover, when the nuclear spins under investigation are not single entities, but (as generally happens) each of them is born on a molecule, their resonance frequency can be slightly different from $\omega_I = \gamma_I B_0$, because of the influence of the molecule's electrons. This phenomenon known as chemical shift (CS) is a two-step process. First the external magnetic field \vec{B}_0 induces currents in the electronic cloud surrounding the molecule; then the circulating molecular currents in turn generates a magnetic field called induced field $B_{j,ind}^{\vec{}}$. The nuclear spins feel the sum of the applied external field and the induced one such as

$$\vec{B}_j = B_{j,ind}^{\vec{}} + \vec{B}_0 \quad (3.25)$$

where \vec{B}_j represents the total magnetic field in the j -site of the molecule. Typically the $B_{j,ind}$ value is only 10^{-4} of B_0 . This is small, but large enough to give rise to measurable shifts in the spin precession frequencies. The induced field can either shield or increase the external one depending on if the induced currents are generated by electrons in the ground state (diamagnetic term) or in the excited states (paramagnetic term) respectively [90].

The induced field is, to a very good approximation, linearly dependent on the applied field, and may be written

$$\vec{B}_{j,ind} = \tilde{\delta}_j \cdot \vec{B}_0 \quad (3.26)$$

where $\tilde{\delta}_j$ is a 3×3 matrix of real numbers called chemical shift tensor. The use of the matrix takes into account that the direction of the induced field can be different with respect to the one of the external field. For each nuclear site, there are three special directions of the external magnetic field for which $\vec{B}_{j,ind}$ is parallel to \vec{B}_0 . These directions are always perpendicular to each other and are called principal axis of the chemical shift tensor. The principal axis are indicated by the capital letters X, Y, Z and often correlate with molecular structures features. In the principal axis system $\tilde{\delta}_j$ is always diagonal and its trace is represented by the principal axis values $\delta_{j,XX}, \delta_{j,YY}$ and $\delta_{j,ZZ}$ [90]. The mean of the three principal axes values is called isotropic chemical shift $\delta_{j,iso}$. If all three principal axis values are equal, then $\tilde{\delta}_j$ is said to be isotropic. If two or more are not equal, then $\tilde{\delta}_j$ is said to be anisotropic and the nuclear system under investigation affected by chemical shift anisotropy (CSA).

In an isotropic liquid, because of motional averaging, the chemical shifted resonance frequency ($\omega_{j,I}$) of the nuclear system results to be, even in case CSA is present [90]:

$$\omega_{j,I} = \gamma_I B_0 (1 + \delta_{j,iso}) \quad (3.27)$$

In a solid the scenario changes dramatically, because the orientation Θ of the nuclear framework with respect to the external magnetic field becomes of fundamental importance. In this case the $\omega_{j,I}$ of each nucleus assumes the form [90]:

$$\omega_{j,I} = \gamma_I B_0 (1 + \delta_{j,zz}(\Theta)) \quad (3.28)$$

Interaction	Spin Hamiltonian component	Magnitude [MHz]
Electron Zeeman	\mathcal{H}_{EZ}	$10^3 - 10^5$
Zero-field splitting	\mathcal{H}_{ZFS}	$< 10^1$
Hyperfine	\mathcal{H}_{HF}	$10^1 - 10^2$
Electron dipolar	\mathcal{H}_{dd}	10^1
Nuclear Zeeman	\mathcal{H}_{NZ}	$10^1 - 10^2$
Nuclear quadrupolar	\mathcal{H}_{NQ}	$< 10^{-3}$
Nuclear dipolar	\mathcal{H}_{NN}	$10^{-3} - 10^{-2}$
Chemical shift	\mathcal{H}_{CS}	$10^{-3} - 10^{-2}$

Table 3.1: Relevant terms of the spin system Hamiltonian we will encounter in the present work with the corresponding magnitude range reported in frequency units. The expression of the chemical shift Hamilton \mathcal{H}_{CS} , not explicit in the text, has the form $\mathcal{H}_{CS} = -\beta_n g_n \sum_{k=1}^m \vec{B}_0 \cdot \tilde{\delta}_k \cdot \vec{I}_k$, see [90] for an extended dissertation about the topic.

where $\delta_{j,zz}(\Theta)$ depends on Θ and the chemical shift principal values. In the case of a powder (or a glass) all possible orientations are possible and, as we will see in Chapter 4, the solid state NMR spectrum can be really broad if CSA is present especially for high values of the external magnetic field [115].

On the other hand, the homonuclear dipolar-broadening, because of the spin concentrations and gyromagnetic ratios involved, was always found to be negligible (< 1 kHz) and, in the special case of ${}^6\text{Li}$ the quadrupole moment $Q = -8.0 \times 10^{-28} \text{ cm}^2$ is one of the smallest among spins $I > 1/2$ [46, 136].

In Table 3.1 are summarized the relevant terms of the spin system Hamiltonian we will encounter in the present work with the corresponding magnitude range reported in frequency units.

3.3 Spin transitions and relaxation processes

The possibility of obtaining dynamic orientation of nuclear spins in dielectric solids containing unpaired electron spins, at low temperature and moderate magnetic fields, rely on the existence of particular transitions between spin states. Some of them, involving

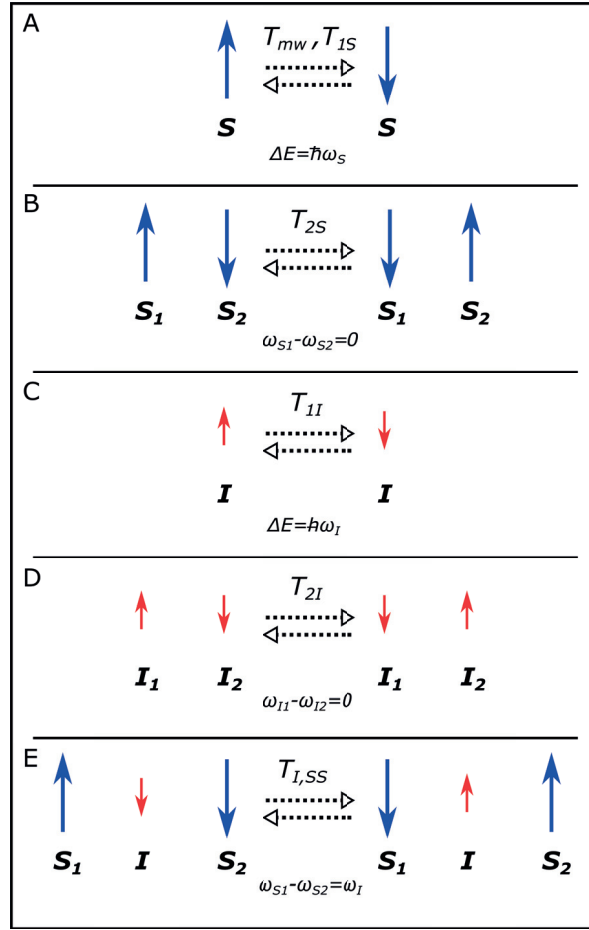


Figure 3.3: Spin transitions responsible for main relaxation processes. Electron spin-lattice relaxation and microwave excitation (A). Electron spectral diffusion (B). Nuclear spin-lattice relaxation (C). Nuclear spin diffusion (D). Electron-nucleus cross-relaxation (E).

one spin kind only, conserve energy and angular momentum and are thus called "allowed transition"; the others, involving both spin kinds, are called "forbidden transition" because they would not conserve angular momentum in the absence of a electron-nucleus dipolar coupling. For simplicity, hereafter only spin 1/2 will be considered. See Figure 3.3 for a summary of the different spin transitions treated.

3.3.1 Electron relaxation processes

The orientation reversal of an electron spin from a state $\uparrow \doteq |S_z = +1/2\rangle$ to a state $\downarrow \doteq |S_z = -1/2\rangle$ (or vice versa) can occur because of the coupling of the spin with the lattice vibrations or under the action of an applied microwave field with a frequency ω_{mw} equal or close to the Larmor frequency ($\omega_S = \gamma_S B_0$) of the electron spin in the applied magnetic field. If such time-dependent perturbation is applied, the Hamiltonian describing the coupling between the microwave rotating field $\vec{B}_1 = B_1 (\hat{x} \cos \omega_{mw} t + \hat{y} \sin \omega_{mw} t)$ (perpendicular to the static magnetic field $\vec{B}_0 = B_0 \hat{z}$) and the electron spin magnetic moment can be written [1]:

$$\mathcal{H}_{mw} = -\gamma_S \hbar B_1 (S_x \cos \omega_{mw} t + S_y \sin \omega_{mw} t) = -\hbar \omega_1 (S_x \cos \omega_{mw} t + S_y \sin \omega_{mw} t) \quad (3.29)$$

Using the Fermi golden rule the transition probability per unit of time induced by equation (3.29) between the two spin states results to be:

$$W_{+\frac{1}{2} \rightarrow -\frac{1}{2}} = W_{-\frac{1}{2} \rightarrow +\frac{1}{2}} = W = \frac{\pi}{2} \omega_1^2 f(\omega) \doteq \frac{T_{mw}}{2} \quad (3.30)$$

where $f(\omega)$ defined in equation (3.18) is the electronic line shape function and T_{mw} the characteristic time constant. Considering an ensemble of electron spins under continuous irradiation, at thermal equilibrium, an energy absorption is observed because the low energy state $\downarrow \doteq |S_z = -1/2\rangle$ is more populated. When the population of the two energy levels is equalized, the system is called saturated. The latter is a non-equilibrium state, the mechanism of spin-lattice relaxation characterized by the constant time T_{1S} tends to restore the Boltzmann condition expressed by equation (2.5), but written for the electrons case.

Several processes are known to cause electron spin-lattice relaxation [3]. For values

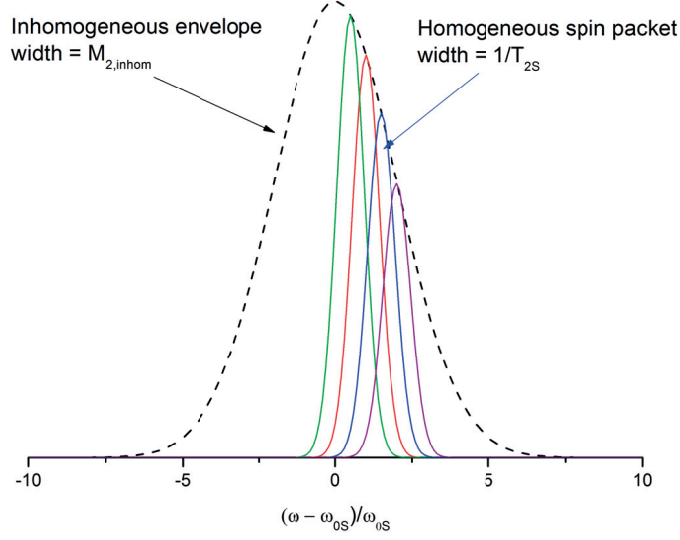


Figure 3.4: Sketch of the ESR line spin packet model.

of temperature and magnetic field routinely used in dissolution-DNP conditions, the mechanism known as "direct process" dominates, consisting simply of an electron flip followed by absorption or emission of a phonon of energy equal to $\hbar\omega_S$. The paramagnetic centers used for DNP are always of the so-called Kramers type (i.e. with an odd number of unpaired electrons). For such paramagnetic species, in a crystal and at very low concentration, the acoustic phonon dispersion leads to a dependence on temperature and magnetic field given by [4]

$$\frac{1}{T_{1S}} = \omega_S^n \coth\left(\frac{\hbar\omega_S}{2k_B\tau_S}\right) \quad (3.31)$$

with $n = 5$ for strict Kramers degeneracy, $n = 3$ if the latter is lifted by hyperfine coupling and τ_S representing the temperature of the electron spins ensemble. It is experimentally proved that for DNP systems the value of T_{1S} is radical concentration dependent [57, 65] so, assuming that equation (3.31) is also valid in a glass, it represents a higher limit for the T_{1S} value.

When the unpaired electron concentration increases, the dipolar coupling becomes

important. The $S_{j,+}S_{k,-}$ terms of the dipolar interaction Hamiltonian (see equation (3.14)) are responsible for a kind of spin transition characterized by the orientation exchange between two electron spins (flip-flop transition). This pure spin-spin process (it conserves angular momentum and the Zeeman energy) takes place with the characteristic time constant T_{2S} called electron spin-spin relaxation time. The latter, function of the distance between the electron spins is concentration dependent; a good estimation is given by $1/T_{2S} = \Delta\omega_S$ (see Section 3.2.6). As already mentioned, those flip-flop transitions are at the origin of the mechanism known as "spectral diffusion" consisting in the propagation, among the electron spin ensemble, of a given spin order reducing polarization differences. The concept was theoretically developed by Portis [116] who introduced the idea of the dependence of the diffusion rate on the ratio between the inhomogeneous line width and the homogeneous line width. Later Bloembergen [20] followed by Mims [107] worked on a model that assumes the inhomogeneous line composed of a series of partially overlapped dipolar-broadened adjacent resonances called "spin packets" (see Figure 3.4). The diffusion time T_{sd} required by an absorbed energy quantum to diffuse across the inhomogeneous line, through several electron spin flip-flops, among the spin packets can be roughly evaluated as [20]:

$$T_{sd} = T_{2S} \left(\frac{M_{2,inhom}}{M_{2SS,hom}} \right)^{3/2} \quad (3.32)$$

Equation (3.32) does not take into account higher order spin transitions (e.g. four or six spins flip-flops) that would eventually shorten T_{sd} . The spectral diffusion is therefore very efficient as soon as the dipolar broadening of one single spin packet is not too small compared to the inhomogeneous broadening. If we consider the example reported in Figure (3.2) T_{sd} turns out to be around $1 \mu s$ much shorter than T_{1S} that for typical DNP conditions (e.g. 5 T and 1 K) is between several hundreds of ms and 1 s [65, 72]. As we

will see, this feature represents a key point in the efficiency of the TM mechanism for DNP: it is possible to saturate the radical ESR line, under microwave irradiation, even if the inhomogeneous broadening dominates. The electron spin lattice relaxation will start to efficiently compete with the spectral diffusion time for radical concentrations around 10^{18} spins/cm³ i.e. 1.5 mM.

3.3.2 Nuclear relaxation processes

The orientation reversal of a nuclear spin from a state $\uparrow \doteq |I_z = +1/2\rangle$ to a state $\downarrow \doteq |I_z = -1/2\rangle$ or vice versa represents the basic process behind nuclear spin-lattice relaxation. It is well known that the latter proceeds mostly via interaction with paramagnetic centers, because the number of phonons "on speaking terms" with the low energy corresponding to the nuclear Zeeman one is extremely small at low temperature [3]. The "direct" (or "leakage" as we will see later) nuclear spin-lattice relaxation can be described, in the frame of the random field approach (BPP theory [19]), as due to the fluctuations of the electronic dipolar field at the nuclear site. For low concentration of unpaired electrons and at low temperature (fixed paramagnetic centers), the correlation time of the random field is T_{1S} and the nuclear spin-lattice relaxation can be written [3]:

$$\frac{1}{T_{1I}} = \frac{9}{4} \left(\frac{\mu_0}{4\pi} \right)^2 \left(\frac{\hbar\gamma_S\gamma_I}{r^3} \right)^2 \sin^2 \theta \cos^2 \theta \frac{T_{1S}}{1 + \omega_I^2 T_{1S}^2} \quad (3.33)$$

where θ represents the angle between the external field \vec{B}_0 and the vector \vec{r} connecting the electron and nuclear spins. In most practical case, $T_{1S}\omega_I \gg 1$ and equation (3.33) can therefore be written

$$\frac{1}{T_{1I}} = \frac{9}{4} \left(\frac{\mu_0}{4\pi} \right)^2 \left(\frac{\hbar\gamma_S}{r^3} \right)^2 \sin^2 \theta \cos^2 \theta \frac{1}{B_0^2} T_{1S}^{-1} \quad (3.34)$$

At low temperature and moderate magnetic field, the electron polarization is close to unity. A correction factor has to be added in equation (3.34) for taking into account the temperature dependence of the nuclear spin-lattice relaxation time [3]:

$$\frac{1}{T_{1I}} = \frac{9}{4} \left(\frac{\mu_0}{4\pi} \right)^2 \left(\frac{\hbar\gamma_S}{r^3} \right)^2 \sin^2 \theta \cos^2 \theta \frac{(1 - P_{0S}^2)}{B_0^2} T_{1S}^{-1} \quad (3.35)$$

where P_{0S} represents the electron Boltzmann equilibrium polarization. The factor $(1 - P_{0S})^2/B_0^2$ gives roughly the transition probability per unit time for an electron to perform a spin-flip causing the dipolar field fluctuation at the nuclear site. At low temperature this factor is very small according to the fact that, when almost all electron spin are frozen in the low energy level, less electron spin-flips triggering nuclear relaxation can occur.

Equation (3.35) was obtained for one electron-nucleus pair and is not directly applicable to bulk nuclei. In the bulk the nucleus-nucleus dipolar interaction, through the $I_{j,+}I_{k,-}$ terms, causes rapid energy conserving flip-flops between nuclear spins, somewhat similar to what happens in the spectral diffusion process among electron spins. This process, known as "nuclear spin diffusion", happens on a time scale characterized by the nuclear spin-spin relaxation time constant T_{2I} (see [18]). It allows to maintain a uniform polarization among the nuclei at all times and starts at a distance b from the paramagnetic impurity. Indeed the NMR frequency shift due to the dipolar local field $\sim \hbar\gamma_S/r^3$, generated by a free electron, does not allow to perform energy conserving flip-flops between nuclei included in a sphere of radius equal to b such that the frequency shift is smaller than the nuclear homogeneous dipolar broadening (see equations (3.16) and (3.17)). The simplest model then assumes that the effective value of T_{1I}^{-1} is the value given by equation (3.35) averaged over all nuclei comprised between a sphere of

radius b and a sphere of volume $V = 1/N_S$ [3]:

$$\frac{1}{T_{1I,eff}} = \frac{1}{V} \int_V \frac{1}{T_1}(\vec{r}) d^3\vec{r} \simeq \frac{2\pi}{5} \frac{N_S}{b^3} \hbar^2 \gamma_S^2 \frac{(1 - P_{0S}^2)}{B_0^2} T_{1S}^{-1} \quad (3.36)$$

A fair estimation of the magnitude of the local field $B_{l,II}$ generating the nuclear homogeneous broadening is the square root of $M_{2II,hom}$ divided by γ_I . As already demonstrated in Section 3.2.6, $\sqrt{M_{2II,hom}}$ is proportional to N_I ; in order of magnitude we can write $B_{l,II} \propto \hbar \gamma_I N_I$. From the definition of diffusion barrier b : $B_{l,II} \sim \hbar \gamma_S / b^3$ we can then write

$$\frac{1}{T_{1I,eff}} \propto \frac{N_S}{N_I} \hbar^2 \frac{\gamma_S}{\gamma_I} \left(\frac{B_{l,II}}{B_0^2} \right)^2 \frac{(1 - P_{0S}^2)}{T_{1S}} = N_S N_I \hbar^2 \gamma_I \gamma_S \frac{(1 - P_{0S}^2)}{B_0^2} T_{1S}^{-1} \quad (3.37)$$

As far as we will be concerned, we do not really care about the precise expression for $T_{1I,eff}$; the remarkable features of equation (3.37) are its linear dependence in the nuclear concentration and gamma and the strong damping at high field due to the factor $(1 - P_{0S}^2)/B_0^2$. Indeed, concerning the expression of T_{1S} reported in equation (3.31), it does not matter which behavior is predominant (strict Kramers degeneracy or hyperfine symmetry breaking): $1/T_{1I,eff}$ is a monotonically decreasing function of B_0 starting from values of the magnetic field interesting for dissolution-DNP (see Figure 3.5A).

If the electronic concentration N_S is not very low, electronic flip-flops will occur at a rate $1/T_{2S}$, much faster than $1/T_{1S}$. It is tempting to argue that T_{2S} rather than T_{1S} is the correlation time of the local electronic field "seen" by the nuclei [3]. We can thus introduce a new nuclear longitudinal relaxation time constant $T_{I,SS}$ characteristic of a

mechanism triggered by the strong dipolar coupling among the paramagnetic centers:

$$\frac{1}{T_{I,SS}} \propto N_S N_I \hbar^2 \gamma_I \gamma_S \frac{(1 - P_{0S}^2)}{B_0^2} T_{2S}^{-1} \quad (3.38)$$

It is clear that the rate given by equation (3.38) has nothing to do with the coupling of the nuclear spins with the lattice since no parameters relative to the latter appear in the formula (in equation (3.37), T_{1S} reflects the lattice acoustic phonon dispersion at a given temperature). What is expressed is the existence of a coupling between the electronic spin-spin energy \mathcal{H}_{SS} and the nuclear Zeeman energy \mathcal{H}_{NZ} , a fundamental step of the DNP process by TM. Indeed we can make the assumption, well verified by experiments [4], that \mathcal{H}_{NZ} and \mathcal{H}_{SS} reach a common spin order (or spin temperature as we will see later in Section 3.4) in a time of the order of $T_{I,SS}$ called cross-relaxation time¹ (or Thermal Mixing time). On a microscopic scale, the energy exchange between the two spin systems occurs as a succession of total energy conserving process, each one of them being a nuclear spin-flip accompanied by a flip-flop between two electron spins S_1 and S_2 separated in energy by $\omega_I = \omega_{S_1} - \omega_{S_2}$.

Dealing with an inhomogeneously broadened radical ESR line, equation (3.38) is still valid if spectral diffusion is efficient (see Section 3.3.1). In that case, a dependence on the ESR line autocorrelation function evaluated at the nuclear Larmor frequency $g(\omega_I)$ has to be added such as [135]

$$\frac{1}{T_{I,SS}} \propto N_S N_I \hbar^2 \gamma_I \gamma_S \frac{(1 - P_{0S}^2)}{B_0^2} \frac{g(\omega_I)}{g(0)} T_{2S}^{-1} \quad (3.39)$$

¹In the literature what we referred as "spectral diffusion time" is sometimes reported as "cross relaxation time". For the sake of clarity we call "cross relaxation time" or "Thermal Mixing" time the one associated with a three-particle energy conserving process that concerns a nuclear spin-flip accompanied by an electron flip-flop.

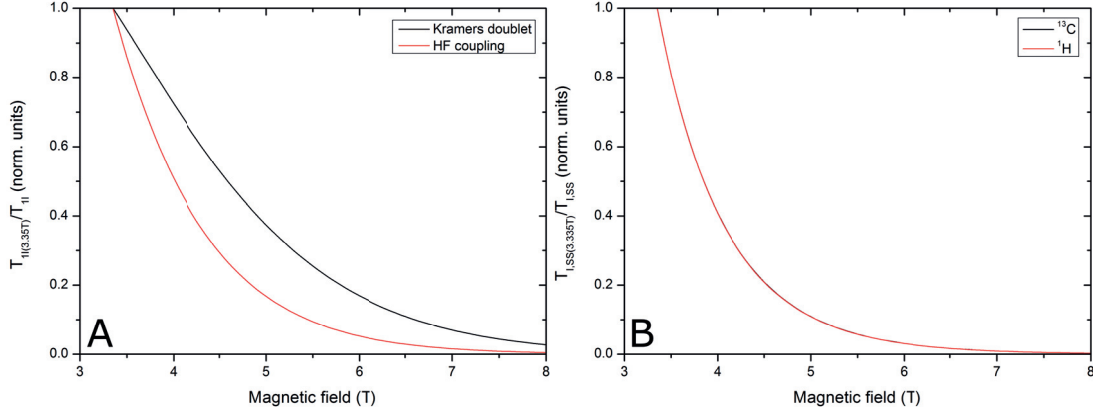


Figure 3.5: Magnetic field dependence of the "direct" (or "leakage") nuclear spin-lattice relaxation time T_{1I} as expressed in equation (3.37) for $n = 5$ (black line) and $n = 3$ (red line) (A). Magnetic field dependence of the cross-relaxation (or "Thermal Mixing") time $T_{I,SS}$ as expressed in equation (3.39) calculated at the ^{13}C (black curve) and ^1H (red curve) Larmor frequency for an ESR line spectrum corresponding to 50 mM of TEMPO radical (see Figure 3.2); the two curves are almost superimposed due to the strong dumping given by the $(1 - P_{0S}^2) / B_0^2$ (B). Both graphs are normalized to the relaxation time value at 3.35 T.

where

$$\frac{g(\omega_I)}{g(0)} = \frac{\int_{-\infty}^{+\infty} f(\omega) f(\omega - \omega_I) d\omega}{\int_{-\infty}^{+\infty} f(\omega)^2 d\omega} \quad (3.40)$$

gives the probability to have a flip-flop transition between two electron spins S_1 and S_2 separated in energy by $\omega_I = \omega_{S_1} - \omega_{S_2}$. The parameters dependence considerations made for equation (3.37) are valid also for (3.39) (see Figure 3.5B).

3.4 DNP via Thermal Mixing

The DNP process takes place through the TM mechanism when the radical ESR line width is comparable or larger than the nuclear Larmor frequency ($\Delta\omega_S \geq \omega_I$) and the electron spin-spin relaxation time is much shorter than the electron spin-lattice relaxation time ($T_{2S} \ll T_{1S}$). Those requirements are always fulfilled when dissolution-DNP is performed on X-nuclei (see for instance [10, 40, 71, 81]). Indeed the field and temperature values together with the radical concentration used for preparing the

sample guarantee the validity of the condition on the electron relaxation times; on the other hand, dealing with nuclei such as ^{13}C , ^{129}Xe , ^6Li , ^{15}N ..., the small gyromagnetic ratio, compared to the proton one, assures the condition $\Delta\omega_S \geq \omega_I$ even in cases where sharp ESR line radicals (e.g. Trityls and BDPA) are involved. Contrary to the "Solid Effect", for which the electron spin order is directly transferred to nuclei through microwave driven "forbidden" double-quantum electron-nucleus spin transitions (see [3] for a detailed dissertation), TM takes place in two steps: "Dynamic Cooling" and "Thermal Mixing" in the strict sense. The first step is a single-quantum transition, thus TM generally requires less microwave power.

3.4.1 Spin Temperature theory and "Dynamic Cooling"

The basic hypothesis in "Spin Temperature" theory [6] is that the evolution of an isolated system of a large number of interacting spins leads to a state of equilibrium characterized by a temperature, i.e. a Boltzmann distribution of the populations in its various energy levels. In formal terms the density matrix σ of the system assumes the form [3]:

$$\sigma = \frac{\exp(-\rho\mathcal{H})}{\text{Tr}(\exp(-\rho\mathcal{H}))} \quad (3.41)$$

where \mathcal{H} is the Hamiltonian of the spin system and $\rho = \hbar/k_B\tau_{spin}$ is the inverse spin temperature. In reality spin systems are never completely isolated and the concept of spin temperature is meaningful only if the rate $1/T_{eq}$ of achievement of internal equilibrium is much faster than the spin-lattice relaxation rate $1/T_1$. For intermediate times between T_{eq} and T_1 , the spin temperature exists and can be different from the lattice temperature. Spin-lattice relaxation then simply describes the equalization of the spin temperature τ_{spin} and the lattice temperature τ_L through the thermal coupling between two reservoirs: the spin system and the lattice.

In that context, the concept of "Dynamic Cooling" uses a fundamental idea first developed by Redfield for NMR under strong radio frequency saturation [120], and later applied to ESR and DNP [23, 127]. Let us first consider an ensemble of N_S electron spins, immersed in a static magnetic field \vec{B}_0 and in equilibrium with the lattice at a temperature τ_L , coupled by dipolar interaction \mathcal{H}'_{SS} (we consider the truncated Hamiltonian only; see equation (3.15)). When a microwave field is applied close to electron Larmor frequency, the effective Zeeman Hamiltonian is time-independent in a frame rotating with the field around \vec{B}_0 (the so-called "rotating frame"), and the large Zeeman part of the static-frame Hamiltonian is considerably reduced. Nevertheless thermodynamics consideration of entropy maximization applies in the rotating frame. Thus the spin polarization can still be expressed as in equation (2.5) with an appropriate "spin temperature" in the rotating frame given by

$$\tau_{rot,L} = \frac{\omega_S - \omega_{mw}}{\omega_S} \tau_L = \frac{\Delta}{\omega_S} \tau_L = \frac{B_{eff}}{B_0} \tau_L \quad (3.42)$$

where B_{eff} represents the effective magnetic field parallel to the \hat{z} axis felt by the spins. If microwaves are shined at a frequency close to the electrons resonance such as B_{eff} is strongly reduced and the electron Zeeman interaction, in the rotating frame, becomes comparable to the dipolar one $\hbar\Delta \approx \langle \mathcal{H}'_{SS} \rangle$ an energy exchange between the two can happen. Provotorov generalized Redfield theory for weak intensity of the microwave field in the "high temperature" limit (see equation (2.6)) for electrons, showing that in the latter case the system can be described by two distinct "spin temperatures" one for the Zeeman interaction and one for the dipolar one [118]. Indeed, owing to the dipolar coupling, the Zeeman levels have a certain width of the order of the local field $\gamma_S B_{i,SS} \approx \Delta\omega_S$. If $\hbar\Delta\omega_S$ is small with respect to the Zeeman energy, but big enough to establish a Boltzmann order among the Zeeman levels through fast flip-flop transitions,

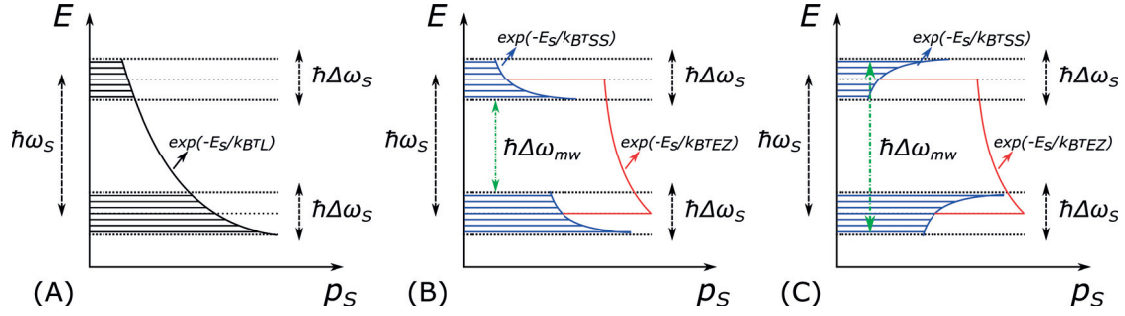


Figure 3.6: Electron spins population distribution p_S between and among the energy Zeeman levels at thermal equilibrium with the lattice ($\tau_{EZ} = \tau_{SS} = \tau_L$) (A); under microwave irradiation at frequency $\omega_{mw} < \omega_S$ ($|\tau_{SS}| < \tau_{EZ}$ with $\tau_{SS} > 0$) (B); under microwave irradiation at frequency $\omega_{mw} > \omega_S$ ($|\tau_{SS}| < \tau_{EZ}$ with $\tau_{SS} < 0$) (C). E_S represents the total energy of the spin system.

then we can segregate the dipolar interaction into a reservoir SSR , separated from the Zeeman one, EZR , and characterized by its own spin temperature and relaxation time. The two spin temperatures τ_{EZ} and τ_{SS} describe the Boltzmann distribution between the Zeeman levels and the spin ordering in the local field, respectively. The time constants T_{1EZ} and T_{1SS} are on the order of the electron spin-lattice relaxation time T_{1S} . The condition required for such situation to be verified is $T_{2S} \ll T_{1S}$ [118]. At thermal equilibrium, the two spin temperatures are equal to the lattice one ($\tau_{EZ} = \tau_{SS} = \tau_L$). However, under some experimental conditions $|\tau_{SS}|$ can be reduced with respect to τ_{EZ} : if slightly off-resonance microwaves are applied, the EZR starts to heat up and the SSR is cooled down. These two processes are limited by spin-lattice relaxation; however the overall effect is to take energy out from SSR and dump it to the lattice (which as usual, is supposed to have an infinite heat capacity, so that its temperature does not change). Depending on the sign of $\Delta = \omega_{mw} - \omega_S$, τ_{SS} can be positive or negative. A pictorial representation is reported in Figure 3.6.

Under such conditions, the evolution in the rotating frame of the inverse spin temperature of the EZR and SSR , $\alpha = \hbar/k_B\tau_{EZ}$ and $\beta = \hbar/k_B\tau_{SS}$ respectively, with respect to the inverse lattice temperature $\beta_L = \hbar/k_B\tau_L$, are given by the two Provo-

torov equations [3, 118]:

$$\frac{d\alpha}{dt} = -W(\alpha - \beta) - \frac{1}{T_{1EZ}}(\alpha - \alpha_L) \quad (3.43)$$

$$\frac{d\beta}{dt} = W\left(\frac{\Delta}{D}\right)^2(\alpha - \beta) - \frac{1}{T_{1SS}}(\beta - \beta_L) \quad (3.44)$$

where $W = 2W_{+\frac{1}{2} \rightarrow -\frac{1}{2}} = \pi\omega_1^2 f(\Delta)$ is twice the transition probability per unit of time induced by the microwave field from state $\uparrow \doteq |S_z = +1/2\rangle$ to a state $\downarrow \doteq |S_z = -1/2\rangle$ or vice versa (see equation (3.30)); $D \doteq \Delta\omega_S$ is the dipolar energy in frequency units and $\alpha_L = \beta_L(\omega_S/\Delta)$ is the inverse lattice temperature in the rotating frame. In steady state conditions ($d\alpha/dt = 0$ and $d\beta/dt = 0$) we obtain the following value of the equilibrium inverse spin temperature of the *SSR*

$$\beta_{eq} = \alpha_L \frac{WT_{1SS}(\Delta/D)^2}{1 + WT_{1EZ} + WT_{1SS}(\Delta/D)^2} = \beta_L \frac{WT_{1SS}(\omega_S\Delta/D^2)}{1 + WT_{1EZ} + WT_{1SS}(\Delta/D)^2} \quad (3.45)$$

Since $\omega_S \gg \Delta$ and D , $|\beta_{eq}|$ is much larger than β_L as soon as WT_{1SS} is non-negligible compared to unity: this represents a "dynamic cooling" of the spin-spin interaction. In case of strong saturation ($WT_{1EZ}, WT_{1SS} \rightarrow \infty$), one has:

$$\beta_{eq} = \beta_L \frac{\omega_S\Delta}{\Delta^2 + (T_{1EZ}/T_{1SS})D^2} \quad (3.46)$$

Is important to stress that the microwave irradiation plays two main roles: cooling down the *EZR* in the rotating frame and allowing an energy exchange between the *EZR* and the *SSR*, since the effective electron Zeeman Hamiltonian becomes similar to the dipolar one ($\Delta \sim D$). Note that no nuclei were involved so far; the dynamic cooling is a manipulation of part of the electron spin Hamiltonian and it exists regardless of the DNP process. A clean demonstration of dynamic cooling without DNP was given by Atsarkin [12].

3.4.2 "Thermal Mixing" in the strict sense

Let us now introduce in our system N_I nuclear spins. The DNP step into Provotorov equations was made by Borghini [23] observing that, if the condition $\Delta\omega_S \geq \omega_I$ is fulfilled, the electron dipolar interaction and the nuclear Zeeman interaction have compatible quanta of energy, and might therefore come into thermal equilibrium if some form of coupling is available between the two. We can thus add a third reservoir to the system, the so-called nuclear Zeeman reservoir NZR , characterized by a spin temperature τ_{NZ} : cooling down the SSR by means of off-resonance microwave irradiation would result in a reduction of τ_{NZ} and thus an increased nuclear polarization. TM in the strict sense is equivalent to what happens when two different liquids at two different temperatures are poured into the same vessel: through several molecular collision the system ends up with a common temperature. In case of electron and nuclear spins, the coupling interaction is represented by cross-relaxation (see Section 3.3.2): through several energy conserving three-particle spin transitions the NZR and the SSR are going to reach the same spin temperature. Once thermal equilibrium is achieved the common spin temperature relaxes toward the lattice with a time constant result of the coupling between the two reservoirs. As already reported before, SSR alone would relax with T_{1SS} , but the NZR acts as an extra "load" slowing down the relaxation processes of the combined (electron) non Zeeman reservoir nZR such as [3]:

$$\frac{1}{T_{1nZ}} = \frac{1}{T_{1SS}} \frac{\langle \mathcal{H}'_{SS} \rangle}{\langle \mathcal{H}'_{SS} \rangle + \langle \mathcal{H}'_{NZ} \rangle} (1 + f) = \frac{1}{T_{1SS}} \frac{D^2}{D'^2} (1 + f) \quad (3.47)$$

where $D'^2 = D^2 + (N_I/N_S) \omega_I^2$ represents the relative "heat capacity" of nZR normalized to one electron spin² and f the so-called "leakage factor" taking into account all "direct" nuclear relaxation processes different from the coupling with the SSR (see Section

²Actually D'^2 represents the nZR relative "heat capacity" multiplied by the square of the off-resonance frequency $\Delta = \omega_{mw} - \omega_S$. That's easy to understand looking at equation (3.44).

3.3.2). It can be shown that $1/T_{1nZ}$ decreases as a function of the magnetic field with the same factor $(1 - P_{0S}^2)/B_0^2$ discussed in Section 3.3.2 [3].

In the limit of very fast cross-relaxation (perfect thermal contact between SSR and NZR) and nuclear spin diffusion, the inverse NZR spin temperature $\gamma = \hbar/k_B\tau_{NZ}$ is uniform among the nuclear system and equals to β at any time. Replacing T_{1SS} with T_{1nZ} and β with γ in equation (3.46), we obtain the steady state solution for the inverse nuclear spin temperature under strong microwave irradiation [3]:

$$\gamma_{eq} = \beta_L \frac{\omega_S \Delta}{\Delta^2 + (T_{1EZ}/T_{1SS}) D'^2 (1 + f)} \quad (3.48)$$

Equation (3.48) can be extended to the case of an inhomogeneous ESR line, if the spectral diffusion is fast enough to keep the same spin temperature across the radical spectrum, replacing D^2 by $M_{2,inhom}$ (see equation (3.20)). Equation (3.48), pictured in Figure 3.7, represents what was called the "DNP microwave spectrum" in Chapter 2. Note that, in the strict sense, TM will exist without microwaves, just as dynamic cooling can exist without the presence of nuclei.

Is now clear that the main feature of TM is the achievement of a common temperature between NZR and SSR , under off-resonance microwave irradiation. That temperature is directly related to the maximum nuclear polarization enhancement ε such as

$$\varepsilon = \frac{\gamma_{eq}}{\beta_L} \quad (3.49)$$

If more nuclear species are involved, they are all going to be in thermal equilibrium with SSR and thus be characterized by the same DNP enhancement. The difference is in the expression of D' that would contain more terms $[(N_I/N_S)\omega_I^2]_i$ one for each "i" nuclear species, thus increasing the relative "heat capacity" of nZR . Indeed in spin temperature theories the "heat capacity" of a reservoir is the derivative of the energy

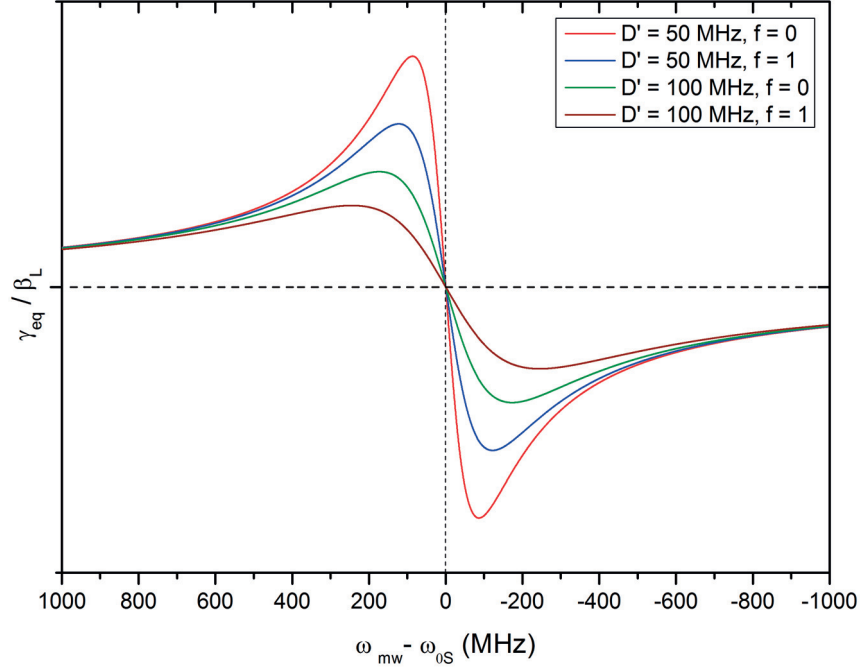


Figure 3.7: DNP enhancement $\varepsilon = \gamma_{eq}/\beta_L$ as a function of the microwave irradiation frequency off-set $\Delta = \omega_{mw} - \omega_S$. $|\varepsilon|$ is maximum when $\Delta^2 = (T_{1EZ}/T_{1SS}) D'^2 (1 + f)$. For all curves reported was assumed $T_{1EZ}/T_{1SS} = 3$.

expectation value with respect to the inverse spin temperature of the reservoir itself [6, 135]. If we imagine to have two nuclear species "a" and "b", we can write the NZR energy content as

$$\langle \mathcal{H}_{NZ} \rangle = N_{Ia} \hbar \omega_{Ia} P_{Ia} + N_{Ib} \hbar \omega_{Ib} P_{Ib} \quad (3.50)$$

where $P_I = \tanh(\gamma \omega_I / 2)$ is the nuclear species polarization expressed in terms of the inverse spin temperature (we dropped the indexes "a" and "b"). Assuming that the two nuclei ensembles have the same γ (as actually happens in TM), in the high temperature approximation equation (3.50) writes

$$\langle \mathcal{H}_{NZ} \rangle = N_{Ia} \hbar \omega_{Ia} \tanh(\gamma \omega_{Ia} / 2) + N_{Ib} \hbar \omega_{Ib} \tanh(\gamma \omega_{Ib} / 2) \approx \frac{\hbar \gamma}{2} [N_{Ia} \omega_{Ia}^2 + N_{Ib} \omega_{Ib}^2] \quad (3.51)$$

Thus the NZR "heat capacity" assumes the form

$$\frac{\partial \langle \mathcal{H}_{NZ} \rangle}{\partial \gamma} = \frac{\hbar}{2} [N_{Ia} \omega_{Ia}^2 + N_{Ib} \omega_{Ib}^2] \quad (3.52)$$

Normalizing to one electron spin we obtain, for each "i" nuclear species, the relative nuclear "heat capacity" term $[(N_I/N_S) \omega_I^2]$ mentioned above.

This feature will not only diminish the maximum achievable γ_{eq} , but also the energy rate exchange between EZR and nZR , thus increasing T_{1nZ} and the time required to achieve thermal equilibrium under microwave irradiation, the so-called "polarization time" T_{pot} . Indeed since, as already mentioned, the temperature of SSR (or the "inhomogeneous broadened" SSR) is transmitted to NZR through cross-relaxation, if more than one kind of nuclei is present, per unit time, not all possible electron-electron-nucleus three particles flip-flops would involve one single nuclear species. Thus, the "cooling power" of the EZR has to be shared among more particles yielding to a less efficient DNP mechanism. Dealing with "broad-band" radicals keeping the nZR heat capacity small represents a fundamental task for achieving high nuclear polarization.

A schematic that summarize DNP via TM mechanism is reported in Figure 3.8.

3.4.3 "Low temperature case": the Borghini model

At low temperature the basic idea of increasing the nuclear polarization by cooling down the EZR through microwave irradiation close to the electron Larmor frequency is still valid, but, unfortunately, there exists no generalization of Provotorov equations when the linear expansion of Boltzmann's exponentials $\exp(-\beta\mathcal{H})$ into $(1 - \beta\mathcal{H})$ is not valid. The root of the problem is the lack of a theory able to predict the temperature of nZR upon off-resonance saturation of the ESR resonance line [3]. A special solution was proposed by Borghini for a simplified model of the ESR line [23]. The Borghini

model describes DNP via TM in case of radicals with an ESR spectrum characterized by anisotropy of the g-tensor and/or the A-tensor. The ESR line shape is assumed to be made of narrow individual spin packets each of them with a resonance frequency ω_{Si} (see Section 3.3.1). In this case the inverse spin temperatures α , β and γ refer, respectively, to the reservoir of electron Zeeman energy evaluated at the average resonance frequency ω_{0S} (analog of *EZR*), to the reservoir of the electronic offset energy *OZR* (the difference between the individual resonance frequency of the packet and the average value, $\Delta_i = \omega_{Si} - \omega_{0S}$), and to *NZR*. It is assumed that the contribution of the electron dipolar interaction to the ESR line width is negligible (a separate energy reservoir is not considered). However, the dipolar interaction plays an important role by inducing, between the various spin packets, a spectral diffusion fast enough to maintain, at all times, a single spin temperature inside the offset Zeeman Hamiltonian \mathcal{H}_{OZ} , which describes the distribution of the spin packets. Moreover the coupling between *OZR* and *NZR* is again considered strong (infinitely fast cross-relaxation) such as to have $\beta = \gamma$ at any time. So there is no *SSR*, and the idea is to cool *OZR*, to a certain spin temperature that is, then, transmitted to *NZR* since the energy quanta between the two reservoirs are comparable. This process is limited by electron and nuclear spin-lattice relaxation T_{1S} and T_{1I} .

Considering g-anisotropy only and $\vec{B}_0 = B_0 \hat{z}$, the Hamiltonian of the spin system writes [3]:

$$\mathcal{H} = \omega_{0S} S_Z - \sum_i \Delta_i S_{Zi} + \omega_I I_Z \quad (3.53)$$

Expressing the ESR line shape following the spin packet model described in Section 3.3.1, but in the offset frequency scale $\Delta = \omega - \omega_{0S}$ such as

$$\int_{-\infty}^{+\infty} f(\Delta) d\Delta = 1 \quad \int_{-\infty}^{+\infty} \Delta f(\Delta) d\Delta = 0 \quad (3.54)$$

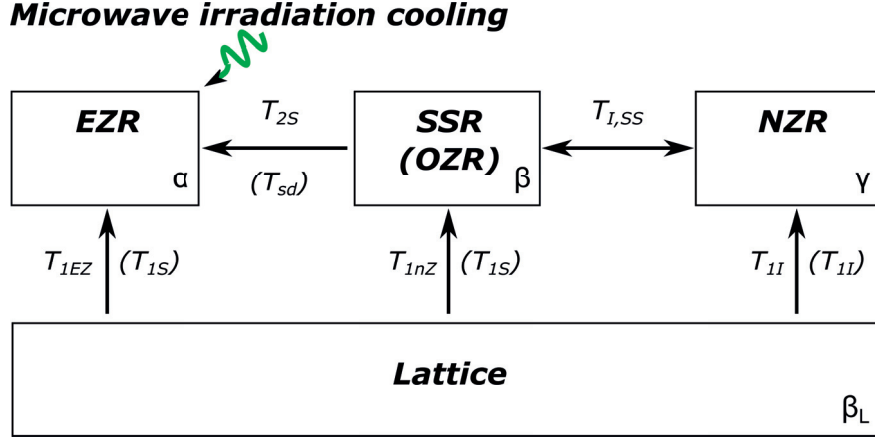


Figure 3.8: Diagram of the TM mechanism. The arrows indicate the heat flow. Terms reported in parenthesis refer to the "low temperature case".

the energy content of *EZR* and *OZR* can be expressed as:

$$\langle \mathcal{H}_{EZ} \rangle = \int_{-\infty}^{+\infty} f(\Delta) \hbar \omega_{0S} P_S(\Delta) d\Delta \quad (3.55)$$

$$\langle \mathcal{H}_{OZ} \rangle = \int_{-\infty}^{+\infty} f(\Delta) \hbar \Delta P_S(\Delta) d\Delta \quad (3.56)$$

where $P_S(\Delta)$, representing the polarization of the electron spin packet resonating at Δ , is assumed to have at any moment the particular form

$$P_S = -\tanh\left(\frac{\alpha\omega_{0S} - \beta\Delta}{2}\right) \quad (3.57)$$

Working through the equations, it can be demonstrated that shining microwaves at a frequency $\omega_{mw} = \omega_{0S} - \Delta_0$ such as to saturate a particular spin packet resonating at Δ_0 , a dynamic cooling of the *OZR* can be obtained [3]. Apart from the value of Δ_0 , the other important parameter is the strength ω_1 of the microwave field (see equations

(3.29) and (3.30)) expressed by the saturation rate

$$r_S = \pi\omega_1^2 T_{1S} \quad (3.58)$$

The original Borghini model was developed under the hypothesis of strong microwave irradiation ($r_S \gg 1$) such as to have the spin packet Δ_0 completely saturated ($P_{S0} = 0$). Expressing the energy content of NZR as

$$\langle \mathcal{H}_{NZ} \rangle = \frac{N_I}{N_S} \hbar\omega_I P_I \quad (3.59)$$

under this condition, we are left with a single spin temperature only ($\alpha = \beta = \gamma$) and, imposing steady state conditions, the Borghini relation is obtained [3]:

$$\int_{-\infty}^{+\infty} (\Delta_0 - \Delta) f(\Delta) \tanh\left(\frac{\gamma(\Delta_0 - \Delta)}{2}\right) d\Delta = -\Delta_0 P_{0S} + \frac{N_I}{N_S} \omega_I \frac{T_{1S}}{T_{1I}} P_I \quad (3.60)$$

where $P_{0S} = -\tanh(\beta_L \omega_{0S}/2)$ and $P_I = \tanh(\gamma \omega_I/2)$ are the thermal equilibrium electronic polarization and the nuclear DNP enhanced polarization, respectively.

The Borghini relation is the low temperature equivalent of (3.48): it represents an integral equation for γ that can be solved numerically if the ESR line shape $f(\Delta)$ is known; in this case no nuclear leakage is considered. The hypothesis of a strong microwave field is not essential to the TM process described above; a model under partial saturation of the Δ_0 spin packet, analog to Provotorov equations at high temperature, was recently proposed [70]. Moreover is important to notice that the Borghini model does not give any information about the dynamics of the process.

Chapter 4

High field DNP: the breakdown of the Thermal Mixing regime¹

“Gutta cavat lapidem.”

P. Ovidius

In the present Chapter, the effect of the magnetic field on the DNP process in case of “broad-line” radicals is investigated. Temperature, paramagnetic centers concentration and target nuclear species (^{13}C) concentration are kept constant. The DNP performances in the same sample prepared with three different levels of deuteration (and thus three different levels of nuclear Zeeman “heat capacity”) are studied as a function of the polarizer magnetic field strength in the framework of spin-temperature theory.

¹Partially adapted from A. Capozzi et al., “High field dynamic nuclear polarization: the role of proton-assisted ^{13}C spin diffusion”, Journal of Physical Chemistry C, 2015, submitted.

4.1 Introduction

In Section 2.5, dissolution-DNP was described as a two step process: first, the nuclear polarization in a frozen sample containing the molecule of interest is enhanced by DNP in a dedicated "pre-polarizer"; second the frozen sample is rapidly transformed into a room-temperature solution and brought to a detection NMR spectrometer (or MRI scanner) for the actual measurement. Since the pre-polarizer is distinct from the measurement device, its magnetic field and sample temperature can be chosen independently of those in the MR spectrometer or scanner.

As already mentioned the original pre-polarizer (see Figure 2.6) [8, 138] worked at 94 GHz ESR frequency; now 140 GHz is the standard frequency of a clinically-compatible commercial instrument [9], and in research laboratories 197 GHz machines have started to appear [34, 69].

For the efficiency of the DNP process, it is necessary that the combination of solvent, radicals and molecules of interest forms a glass (see Section 2.5.1), as opposed to a cluster of microcrystals that can result from rapid freezing of e.g. pure water. Ideally, the structure of the glass is just a "snapshot of a liquid configuration", with its positional and orientational disorder. For this reason, a glassing agent (e.g. ethanol and glycerol) is often added to the sample preparation prior to freezing.

As a rule, increasing the field slows down the dynamics of the DNP process (see Section 3.3.2 about nuclear spin relaxation in particular Figure 3.5), which can be, at least in part, compensated by increasing the radical concentration. However, solubility and homogeneity become more problematic at higher concentrations, especially in mixed solvents.

The most common DNP process, certainly for nitroxyl radicals, is TM (see Section 3.4). Since usually we are only interested in hyperpolarizing low-gamma nuclei such as ^{13}C , it is a waste of "cooling power" if a large quantity of high-gamma nuclei

(in practice 1H) is present in the sample, because it increases the "heat capacity" of the nuclear Zeeman system. It is thus advantageous to deuterate the solvent [81, 99]. However, in a recent publication using a 197 GHz pre-polarizer, it was found that for a particular application of the method some of the common wisdom does not hold [34]: for glycerol/water solvents, a partial deuteration worked better than full deuteration. The purpose of the present study is to investigate the field-dependence of this phenomenon in the pre-polarizer stage. We have studied ^{13}C and 1H DNP in samples of a single molecular solvent composition (60:40 water/glycerol in volume) and a fixed concentration of nitroxyl radicals (50 mM TEMPOL), for three degrees of deuteration of the solvent, and at three magnetic fields. The ^{13}C nuclei are provided by sodium acetate (3 M), 99 % labeled in the carbonyl position. We will discuss the results within the framework of the "Borghini model" (see Section 3.4.3).

4.2 Experimental methods

4.2.1 Samples preparation

1.8×10^{21} spins/cm³ (i.e. 3 M) of sodium [$1-^{13}C$]acetate and 3.0×10^{19} spins/cm³ (i.e. 50 mM) of TEMPOL (4-hydroxy-2,2,6,6-tetramethylpiperidine 1-oxyl) nitroxyl radical were dissolved in a 60:40 H₂O:glycerol (v/v) solution with three different degrees of deuteration (100%: sample "FD"; 50%: sample "HH"; 0%: sample "FP"). For the HH sample, both solvents volume were 50% deuterated (30:30:20:20 H₂O:D₂O:glycerol: d_8 -glycerol). All chemicals were purchased from Sigma – Aldrich, Buchs, Switzerland.

These sample compositions have not been optimized for any of the three magnetic fields considered, but the chosen radical concentration gives a reasonably fast build-up of the ^{13}C polarization at each field and the water/glycerol ratio supplies about the same amount (3.3×10^{22} spins/cm³) of 1H (or 2H) nuclei from both solvents. Moreover,

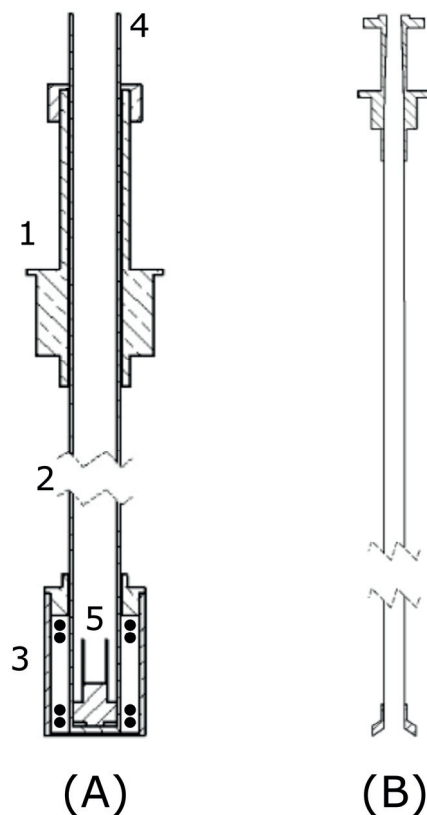


Figure 4.1: Schematic drawings of the cryostat inserts. (A) The main insert (1, 2, 3) with the fiberglass sample-holder insert (4), and sample-cup (5) in place. To see just the main insert, imagine sliding upwards the tube (4), including the sample-cup (5). The main insert top flange (1) fits into the central access of the polarizer cryostat and through stainless steel thin tubes (2) retains the microwave cavity (3). The NMR saddle coil sits inside the cavity (represented by the four black dots), outside the sample-holder insert. (B) The microwave insert: its main part is a circular tube, its top part a transition from rectangular to circular waveguide, its bottom part a small cylindrical microwave horn.

we found these samples to be stable and reproducible.

The containers in which the solutions were mixed were sealed and placed in a water bath at 40 °C for 1 h to obtain homogeneous liquid samples. After thermalization to room temperature, a polytetrafluoroethylene (PTFE) sample-cup was filled with 300 μ L of solution and immediately immersed in a polystyrene box containing liquid nitrogen in order to obtain a frozen glassy block suitable to perform DNP. For best results at low temperatures the preferred method is to freeze individual droplets in order to minimize

B_0 [T]	ESR [GHz]	^1H NMR [MHz]	^{13}C NMR [MHz]
3.4	94.88	143.90	36.18
5	140.12	212.50	53.44
7	197.06	298.89	75.16

Table 4.1: ESR and NMR frequencies at the three nominal field values.

the sample heat capacity,² but here we work at 1.5 K and sample blocks are more easily reproduced across the three different polarizers used. A similar sample preparation method has been used before [81].

The polystyrene box was then moved in proximity of the DNP machine and the sample cup was loaded inside the polarizer (already filled with liquid helium) by means of the fiberglass “sample-holder” insert (see [40, 39] for details about the sample handling and DNP polarizer components). At that point the waveguide was inserted concentrically inside the latter and the microwave source connected. A sketch of the sample-holder insert and microwave insert is reported in Figure 4.1.

4.2.2 Solid state DNP measurements

Solid state DNP measurements were performed using three similar custom-built polarizers [40] operating at the nominal field values of 3.4 T, 5 T and 7 T (see Table 4.1 for a summary of the different resonance frequencies). At all fields DNP was performed at 1.50 ± 0.05 K. That temperature was reached by pumping the liquid helium bath inside the polarizer cryostat around 10 mbar by means of a 40 m³/h rotatory vane pump (Trivac D65B-Leybold, Zurich, Switzerland), after the sample was loaded. The microwave sources were, at 94 GHz, a VCOM-10/94/2/200, at 140 GHz, a VCOM-6/140/1/60, and at 197 GHz, a VCOM-5/197/0.5/60 (ELVA-1, St. Petersburg, Russia).

The ^{13}C polarization time evolution was monitored using a home-made NMR setup (see Figure 4.2), applying a small $\sim 3^\circ$ radiofrequency (rf) pulse every 5 min. Once the

²We here intend the thermodynamic heat capacity, not the one related to the spin system.

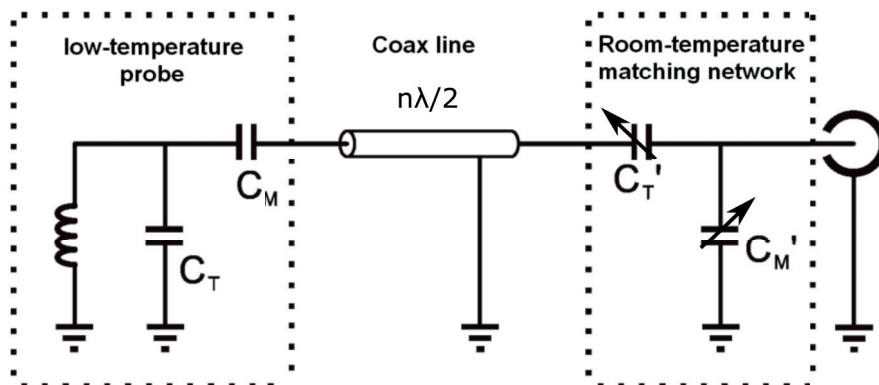


Figure 4.2: Low temperature NMR probe mounted on the main insert (see Figure 4.1A) and remote room-temperature tuning/matching network. Small arrows indicate variable capacitors.

maximum polarization was reached (within 10 % of the plateau level), a 10-fold stronger rf pulse (30°) was applied. Microwaves were then switched off and the NMR signal destroyed by applying a comb of rf pulses. Then, the longitudinal relaxation of the sample was measured by applying the small rf pulse, used for monitoring the polarization build-up, every 30 min. After waiting for a sufficiently long time to reach thermal equilibrium (within 10 % of the plateau level), another strong rf pulse was applied to measure the reference signal corresponding to the nuclear Boltzmann polarization.

The 1H NMR signal was also recorded for each sample in a separate set of experiments. The polarization time evolution and DNP enhancement were measured as described above, with the difference that the repetition time between the rf pulses was reduced to 2 min during the polarization (microwaves on) and 15 min during relaxation (microwaves off), because of the faster dynamics of protons. Moreover, the bottom of the sample-holder insert was replaced by one entirely made of PTFE to avoid any signal contamination from surrounding protons.

The NMR coils, placed inside the microwave cavity (see Figure 4.1A), were single-tuned saddle coils pre-tuned and -matched by means of ceramic chip capacitors (ATC-100B, American Technical Ceramic, USA). Proper matching ($50\ \Omega$) and fine tuning to

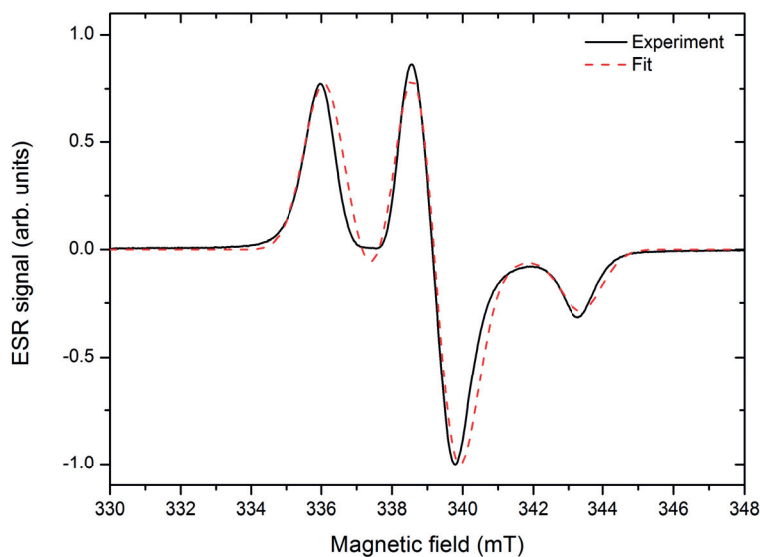


Figure 4.3: HH sample ESR X-band measurement (black continuous line) and relative fit (red dashed line) using the PEPPER routine of the software package EASYSPIN [128].

the appropriate nuclear Larmor frequency (see Table 4.1), at the different fields, were achieved by means of an external serial tuning/matching circuit, following the scheme shown in Figure 4.2 (see [39] for details).

4.2.3 Calculated ESR spectra

The parameters used to calculate the TEMPOL powder ESR spectra at the three different magnetic fields were obtained from X-band ESR measurements performed at 77 K (see Section 5.2.1 for details about measurements). The reference spectrum was obtained from 24 μL of HH sample solution, poured in a synthetic quartz cold finger (Wilmad, 150 mL Suprasil dewar ask type WG-850-B-Q) filled with liquid nitrogen. The cold finger was subsequently inserted into the ESR spectrometer cavity (EMX, Bruker Biospin, Rheinstetten Germany) for measurements. The results were fitted using the PEPPER routine of the software package EASYSPIN [128]. An example is shown in Figure 4.3. Apart from a phenomenological $FWHM$ Gaussian line broadening = 40 MHz, the results for the principal values of the g-tensor = [2.0095; 2.0066; 2.0018]

B_0 [T]	Sample	$\varepsilon_{^{13}\text{C}}$	$\varepsilon_{^1\text{H}}$	$T_{pol,^{13}\text{C}}$ [s]	$T_{pol,^1\text{H}}$ [s]	$T_{rel,^{13}\text{C}}$ [s]	$T_{rel,^1\text{H}}$ [s]
3.4	FD	100	95	110	26	1396	408
3.4	HH	79	78	247	73	2250	800
3.4	FP	52	54	432	190	2442	1054
5	FD	105	110	850	65	4280	2300
5	HH	83	90	1512	245	5800	4000
5	FP	66	68	1834	340	6310	3630
7	FD	60	94	6600	103	35000	4519
7	HH	110	74	3750	380	18500	10442
7	FP	100	76	5410	630	25500	11219

Table 4.2: Summary of experimental results for ^{13}C and ^1H nuclei in the three samples (FD, HH and FP) at three magnetic field values B_0 . The estimated error margins are 10 %.

and A-tensor = [20.58; 17.58; 101.10] MHz were in good agreement with results reported at 2.5 T [62].

4.3 Experimental results

A summary of the results determined by experimental measurements is presented in Table 4.2; the standard deviation was typically around 10 %. All data reported, for both ^{13}C and ^1H nuclei, were obtained with the microwave frequency fixed at the negative extremum of the ^{13}C microwave spectrum (see Figure 4.5 and Figure 4.8) and with the minimum nominal output microwave power giving the best enhancement (see Appendix A).

The polarization time constant T_{pol} and the relaxation time constant T_{rel} were evaluated by fitting the NMR signal integral time evolution (data not shown) to the exponential law $S(t) = S_0 + S_\infty [1 - \exp(-t/T_{cost})]$ where $S(t)$, S_0 , S_∞ and T_{cost} represent, respectively, the signal amplitude as a function of time, the signal amplitude at $t = 0$ (first point recorded), the signal amplitude at $t = \infty$ (plateau) and the time constant. The correction due to the rf pulse was in all cases negligible.

We prefer to report the DNP enhancement (ε) rather than the polarization level

because it is directly deduced from raw data. ε was obtained by computing the ratio between the NMR signal corresponding to the maximum polarization during microwave irradiation (polarized steady state) and the one corresponding to Boltzmann thermal equilibrium, both obtained by integration after a 30° rf pulse i.e. $\varepsilon = \text{Int}(DNP - signal)_{30^\circ} / \text{Int}(Boltzmann - signal)_{30^\circ}$.

4.4 Discussion

4.4.1 Relation with earlier results

As described in Section 3.4.3 the original Borghini model [23] discusses only stationary states, and was developed within the hypothesis of very strong microwave irradiation ($r_S \rightarrow \infty$, see equation (3.58)) such that the spin packet Δ_0 is completely saturated ($P_{S0} = 0$). Moreover, the thermal mixing rate $1/T_{I,SS}$ is supposed to be fast, and the nuclear spin-lattice relaxation rate $1/T_{1I}$ extremely slow. In that case, only one spin temperature parameter remains, similar to the Redfield model [120]. It was remarked [23] that this approximation can only yield an upper limit of the achievable nuclear polarization. We will refer to this result as the Redfield-Borghini limit. That experimentally the Redfield-Borghini limit cannot be reached by increasing the microwave power is thought to be due to dielectric heating of the sample by the microwaves, but the effect is difficult to model [22, 31]. Another result that is only valid in the Redfield-Borghini limit is the field-independent enhancement of nuclear polarization shown in [40].

Experimental ^{13}C microwave spectra at 94 GHz and 140 GHz (that showed very similar enhancements) could be fitted with two sets of two parameters (including finite values for r_S) [70], but there is no fundamental reason that the same enhancement should be found at 197 GHz.

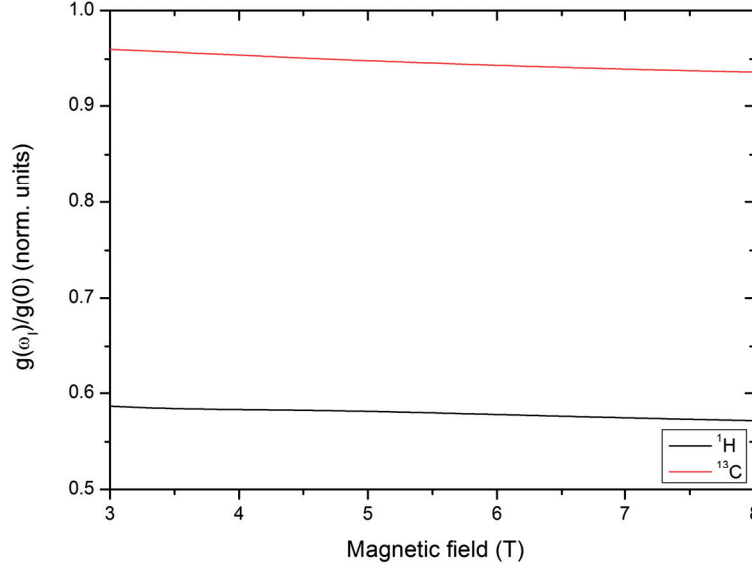


Figure 4.4: Magnetic field dependence of the normalized TEMPOL ESR line autocorrelation function $g(\omega_I)/g(0)$ (see equation (3.40)) evaluated for the Larmor frequency of ^1H (black line) and ^{13}C nuclei (red line).

The definition of r_S together with the expression of the electron spin-lattice relaxation time (see equation (3.31)) suggests that at higher field a higher microwave power is needed to achieve the same dynamic cooling because of the shortening of T_{1S} . The nominally 60 mW/197 GHz microwave source that we have used here can probably not reach the optimum. Moreover, its sweep range does not cover the best frequency for negative nuclear polarization (see Figure 4.8). However, the relative results that we find here should be independent of these limitations.

For what concerns the dynamics, if it is assumed that all nuclei have very short thermal mixing times, then during build-up (and also during decay) of the nuclear polarizations, all nuclei (and the electronic offset reservoir) have at each instant the same spin temperature: this was found to be the case for deuterons and protons in one of the earliest studies of this question [21] (actually, only build-up curves are shown in that paper).

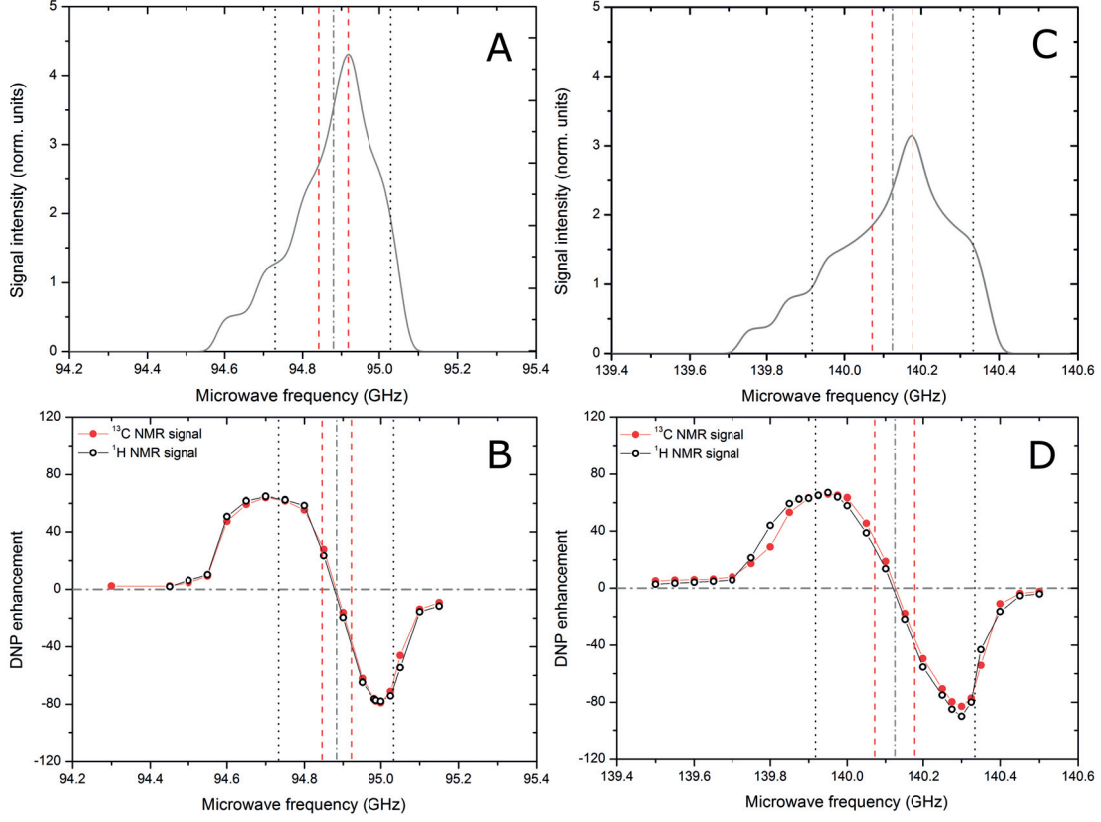


Figure 4.5: Calculated TEMPOL ESR powder spectrum at 3.4 T (A) and 5 T (C). HH sample 1.5 K DNP microwave spectrum measured at 3.4 T (B) and 5 T (D) for both ^{13}C nuclei (red dots) and ^1H nuclei (black circles); each data point represents the steady state DNP enhancement ε calculated as explained in Section 4.2.2; the line connecting the points is drawn only to guide the eye; FP and FD samples showed almost identical spectra (except for the DNP enhancement value) confirming that TM takes place at the two lower fields. In all panels the two red dashed vertical lines and the two black dotted vertical ones indicate, respectively, the ^{13}C and ^1H Larmor frequencies with respect to the ESR spectrum center of gravity (gray dot-dashed vertical line).

For samples of the type that we use here, it has already been shown [81] that at 3.4 T the dynamics of the carbons is slower than that of the protons; we now find the latter result to be valid at higher fields as well. This implies that the carbon and proton thermal mixing times $T_{SS,I}$ are different. If for simplicity one assumes that dynamic cooling is very fast, then the nuclear dynamics are proportional to the factor $N_I\gamma_I$ reported in equations (3.37) and (3.39).

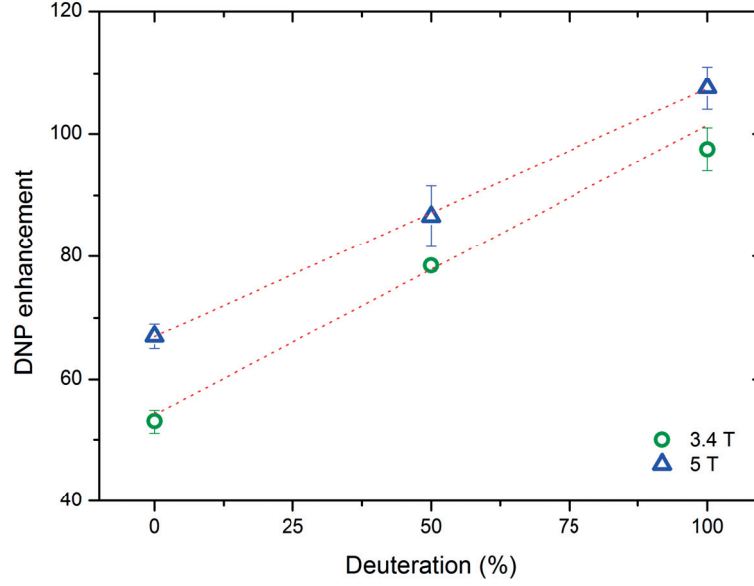


Figure 4.6: DNP “best enhancement” at 3.4 T (green circles) and 5 T (blue triangles). For each sample (specified by the level of deuteration on the horizontal axes) the data points reported correspond to the average between the ^{13}C and ^1H enhancement and the error bar is the standard deviation. At both field a linear relation was found between DNP enhancement and level of deuteration (dotted red line).

In the latter equation there is also an additional nuclear dependence through the autocorrelation function $g(\omega_I)$ that roughly compensate for γ_I , but its effect is not comparable to the difference in concentration (about 40 times) between ^{13}C and ^1H nuclei in the samples considered (see Figure 4.4).

The fact that the DNP polarization time constant is shortened for increasing nuclear spins concentration has been experimentally demonstrated at 94 GHz for ^{13}C [40, 96]. Changing the carbon concentration at otherwise constant sample composition does not change the nuclear Zeeman total heat capacity expressed in equation (3.52) significantly (as confirmed from the value of the steady state DNP enhancement in [40, 96]), so this is a pure dynamic effect.

4.4.2 Data analysis at 3.4 T and 5 T

At each of these fields and for each of the three samples the proton and carbon microwave spectra are very similar (see Figure 4.5), which is the typical signature of DNP by dynamic cooling and thermal mixing. Another typical result, plotted in Figure 4.6, is the effect of deuteration on the enhancement. At 3.4 T, the linear relation and the doubling of the enhancement upon deuteration has also been found in [81], and the effect has been studied experimentally for several radicals in [99]. This shows that the main influence of deuteration on the stationary enhancement is to change the nuclear-Zeeman heat-capacity of the solvent. Looking at equation (3.52), if among the N_I NMR active nuclear spins composing the solvent x are protons and $(1 - x)$ are deuterons, both with inverse spin temperature γ the associated heat-capacity writes:

$$\left[\frac{\partial \langle \mathcal{H}_{NZ} \rangle}{\partial \gamma} \right]_{\text{solvent}} = \frac{\hbar}{2} N_I [x \omega_{1H}^2 + (1 - x) \omega_{2H}^2] \quad (4.1)$$

Increasing the deuteration also makes the dynamic faster. For a given dynamic cooling capacity (determined by the finite value of the r_S factor at constant radical concentration), the "lighter" the total NZR , the faster γ will increase (see equation (3.47)). The observed relaxation of the nuclear polarization is not necessarily a measure for the parameter T_{1I} , because the $T_{I,SS}$ mechanism is also present during relaxation. So, nuclear relaxation can proceed through two parallel channels: the "direct" (or leakage) T_{1I} , and the serial relaxation that first takes place via interaction with the electronic offset reservoir ($T_{I,SS}$), and then to the lattice through (T_{1S}). The two channels have different field and temperature dependencies, so their relative efficiency varies with B_0 and τ_L . The relaxation data in Table 4.2 have been obtained from saturation recovery, not as a decay of DNP-enhanced nuclear polarizations.

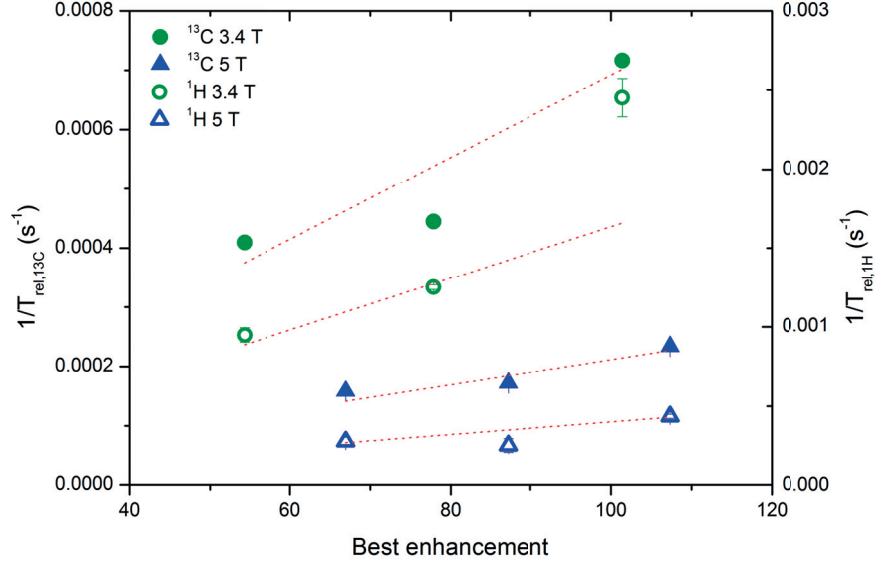


Figure 4.7: For each sample $1/T_{rel}$, of both ^{13}C and 1H , was plotted as a function of the DNP “best enhancement” shown in Figure 4.6. Each data set was fitted through a straight line passing from the origin. The behavior pictured here represents a test of the hypothesis that more efficient thermal mixing (faster relaxing sample) leads to higher enhancement.

We can thus postulate the following approximate relation:

$$\frac{1}{T_{rel}} \approx \frac{1}{T_{1I}} + \frac{1}{T_{1S} + T_{I,SS}} \quad (4.2)$$

The last term of equation (4.2) is conceptually similar to the nZR relaxation expressed in equation (3.47). If T_{1S} is short and T_{1I} is long with respect to $T_{I,SS}$, then the relaxation time in equation (4.2) is a measure of the efficiency of TM. We test in Figure 4.7 the hypothesis that more efficient TM will lead to larger enhancements. There is a strict correlation, and to a reasonable approximation the relation is linear. It can also be expected that for a given value of the r_S parameter, a faster TM will lead to a faster build-up, so that samples with the fastest dynamics also have the highest stationary enhancement. Altogether, the DNP behavior of these water/glycerol-based samples at these two fields does not show any unexpected features.

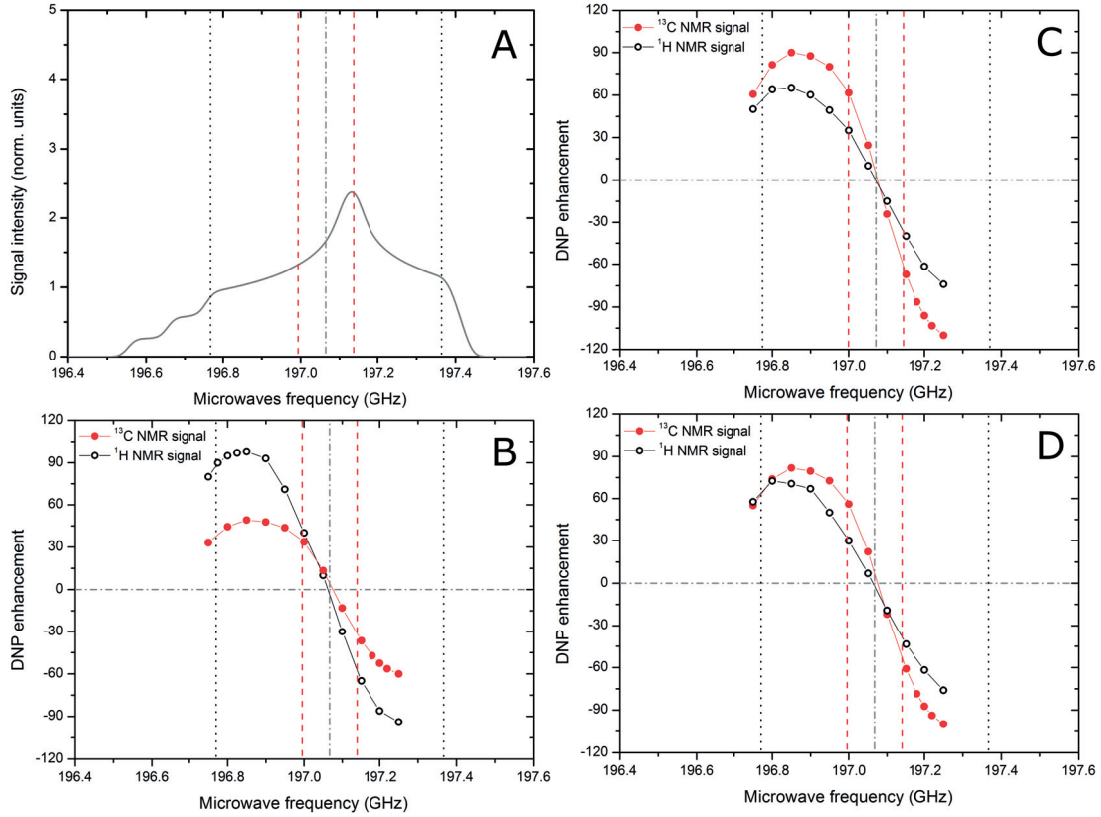


Figure 4.8: Calculated TEMPOL ESR powder spectrum at 7 T (A). FD sample (B), HH sample (C) and FP sample (D) 1.5 K DNP microwave spectrum measured at 7 T for both ^{13}C nuclei (red dots) and ^1H nuclei (black circles); each data point represents the steady state DNP enhancement ε calculated as explained in Section 4.2.2; the line connecting the points is drawn only to guide the eye; at this field, for each of the three samples, the ^{13}C and ^1H enhancements were different showing that pure TM is no longer observed at 7 T. In all panels the two red dashed vertical lines and the two black dotted vertical ones indicate, respectively, the ^{13}C and ^1H Larmor frequencies with respect to the ESR spectrum center of gravity (grey dot-dashed vertical line).

4.4.3 Data analysis at 7 T

The ^1H and ^{13}C microwave spectra for the three samples are reported in Figure 4.8. It is clear that they do not satisfy the essential result of a Borghini model for a "broad-line" radical: in the steady state the DNP enhancements of the two nuclei are not equal.

If we consider the nuclei individually, we still observe from the data in Table 4.2 that there is a correlation between enhancement and dynamics, similar to what is

reported Figure 4.7; but in terms of deuteration, the sequence is now different for the two nuclei. Within the experimental precision, the proton data can be said to follow the standard sequence upon deuteration, but the carbon polarization is clearly not optimal at full deuteration. A similar effect has been reported in [34], for a series of samples labeled GlyDD66, GlyHD66 and GlyHH66. The 66 in the labels refers to the radical concentration in mM; and the DD, HD and HH are equivalents of our FD, HH and FP labels. The enhancements at 7 T and 1 K were (in round numbers) 90, 140 and 90. However, at the same 66 mM concentration of radical the enhancements in ethanol-based samples, although fairly modest in absolute value, were better at full deuteration (roughly 45), than for the mixed proton/deuteron composition (roughly 30). Further data in that paper [34] show a much stronger variation of optimal enhancement with radical concentration than what has been reported earlier at 94 GHz [81]. Because of the limited frequency range available from our 197 GHz source it is difficult to analyze in detail what mechanism might cause this remarkable solvent specificity; but we can propose a physical process that for ^{13}C would favor protonation.

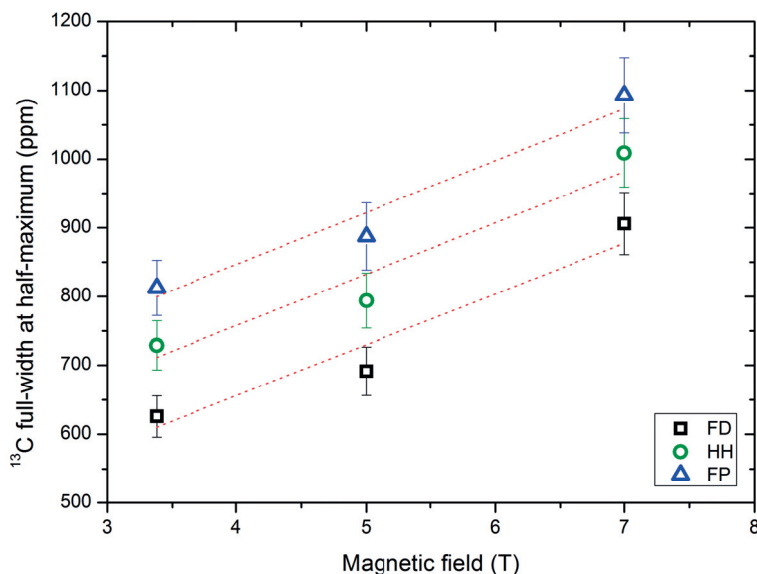


Figure 4.9: Effect of chemical shift anisotropy (CSA) and solvent deuteration on the ^{13}C NMR line width. For all sample the full-width at half-maximum (FWHM) is plotted as a function of the magnetic field; a linear fit was imposed for each dataset (dotted red line). The CSA is reflected by the value of the slope of the linear fit that for all samples was found to be constant and equal to 75 ± 15 ppm/T. An estimation of the dipolar broadening due to ^{13}C heteronuclear coupling with the $^1\text{H}(^2\text{H})$ nuclei composing the solvent is represented by the different intercept of the three lines: 360 ± 96 ppm, 458 ± 100 ppm and 544 ± 80 ppm for the FD, HH and FP sample respectively. These values correspond to a local dipolar field of 0.35 ± 0.2 mT, 0.47 ± 0.03 mT and 0.55 ± 0.03 mT.

Whatever the exact DNP mechanism, it is likely that nuclear spin diffusion is important to establish the stationary state. The chemical shift anisotropy (CSA) pattern for ^{13}C in acetate has a width of about 140 ppm [115], and strictly Zeeman-conserving flip-flops between neighbors are unlikely, since in a glass the orientation of the CSA tensors for neighboring molecules are uncorrelated [130]. The difference can be made up by a change in the heteronuclear proton-carbon dipolar coupling, a phenomenon known as proton-assisted carbon spin-diffusion (where no flip of a proton is supposed). Because of the simultaneous effect of working at higher field in slowing down the thermal mixing time $T_{I,SS}$ (see Figure 3.5B) and increasing the carbon line width, the carbon dynamics becomes very slow in a fully deuterated solvent, possibly up to a point where ^{13}C thermal mixing is no longer effective. In that case protonation gives an advantage.

The balance between solvent heat capacity, equation (4.1), and proton-assisted carbon spin diffusion then results in an optimum at partial deuteration.

That indeed the observed ^{13}C NMR line width depends on field and on degree of protonation is shown in Figure 4.9. The constant slopes show a 75 ppm CSA effect on the $FWHM$, quite compatible with a 140 ppm total width of a resolved CSA structure. The intercepts FD: HH: FP, indicating the field independent broadening, are in a ratio 0.35 : 0.47 : 0.55 mT. On the other hand a theoretical calculation of the heteronuclear dipolar broadening contributions to the ^{13}C solid state NMR line (see Appendix A) for the three samples FD: HH: FP are in a ratio 0.12 : 0.36 : 0.50 mT. While the FP and HH broadening values, even though slightly smaller, are in good agreement with the intercept values, the FD one does not. Indeed a more detailed analysis should take into account that, supposing perfectly deuterated solvents, the FD sample has residual protons very close to the acetate ^{13}C nucleus residing on the CH_3 methyl group. Its contribution to the line broadening is not easy to model, because of the rotation tunneling phenomenon characterizing methyl groups at low temperature [38].

Chapter 5

UV-induced non-persistent radicals for DNP¹

“We all know that light travels faster than sound. That’s why certain people appear bright until you hear them speak.”

A. Einstein

In the present Chapter, non-persistent radicals arising from UV-light illumination of frozen pyruvic acid (PA) at liquid nitrogen temperature are investigated in some depth for applications in dissolution-DNP. After the first pioneering work [49], aiming mostly at demonstrating the applicability of the technique to *in vivo* metabolic imaging, we herein focus on the versatility and potentiality of the UV-radical itself.

Providing an exact theoretical analysis of the PA photochemistry is complex and far beyond the scope of this thesis. The reader should refer to existing literature (e.g.

¹Partially adapted from A. Capozzi et al., "Photoinduced Nonpersistent Radicals as Polarizing Agents for X-Nuclei Dissolution Dynamic Nuclear Polarization", J. Phys. Chem. C 2015, 119, 22632-22639.

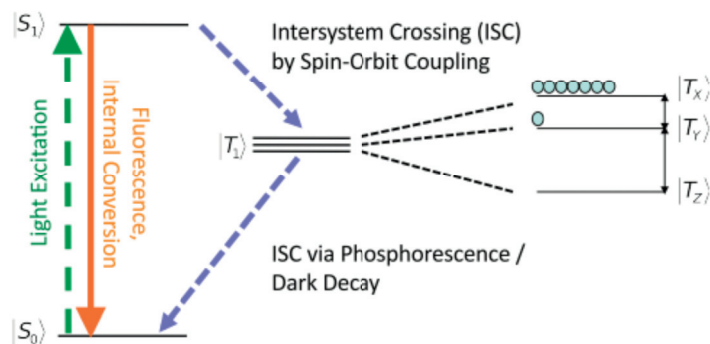


Figure 5.1: Simplified Jablonski diagram of the lowest energy levels of electronic states of a molecule ordered by their spin multiplicity (singlet and triplet states, therein the fine-split sublevels), showing the possible photo-physical processes of excitation and decay of an intermediate paramagnetic triplet state [48].

[59, 58]). The analysis of the radical species and factors that influence its generation is mostly based on the interpretation of measured ESR spectra.

5.1 Introduction

Many organic molecules dissolved in glassy solvents at low temperatures exhibit phosphorescence upon irradiation with UV-light [95]. The lifetime of this phenomenon varies from few ms to about 30 s and was attributed by Lewis and Kasha [91] to the radiative decay from the lowest excited triplet state $|T_1\rangle$ (spin multiplicity 1) of the molecule to the ground singlet state $|S_0\rangle$ (spin multiplicity 0). The triplet state is populated via radiationless transitions, called "Inter System Crossing" (ISC), from the lowest excited singlet state $|S_1\rangle$, into which the molecule reverts following the initial UV-light excitation. The evolution between different multiplicity spin states is driven by spin-orbit coupling. The situation is summarized in Figure 5.1.

Among those molecules numerous studies have been performed on α -keto acids, with particular focus on PA (see e.g. [88, 108]). α -keto acids are organic compounds especially important in biology as they are involved in the Krebs citric acid cycle and

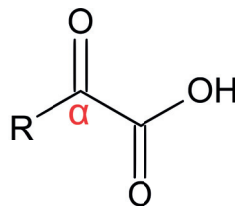


Figure 5.2: α -keto acid general chemical structure; R represents a chemical non-reactive residual group that specifies the molecule.

in glycolysis. They contain a carboxylic group and an adjacent ketone group placed in correspondence of the first carbon from the carboxylic acid (α -position). The general chemical structure is reported in Figure 5.2, where R represents a chemical non-reactive residual group that specifies the molecule. In the case of PA the residual group is a methyl group (CH_3). In the context of dissolution-DNP, some members of the α -keto acids family have been used as HP substrates to study *in vivo* metabolism in real time (e.g. [56, 77]).

It has been widely demonstrated that under UV-light illumination PA can transform in intermediate radicals that can be, at least partially, stabilized at liquid nitrogen temperature [59, 58]. The generation of those paramagnetic species has been explained by photo-excitation of the $n - \pi^*$ transition (300 – 350 nm) of the α -carbonyl group, followed by efficient ISC to an excited triplet state with a yield reported to be close to unity [32, 88]. This latter molecular state has a lifetime long enough to be chemically reactive and form radicals. Hydrogen abstraction and/or electron transfer have been described. Both pathways are critically dependent on the environment of the photo-excited molecule (e.g. purity and kind of solvent) [88, 5]. Thus two kinds of radical can be obtained: a lactyl-like radical (product of a hydrogen abstraction) or a pyruvyl-like radical (produced by a proton coupled electron transfer). In both pathways, either a second α -keto acid or a solvent molecule can be considered as the partner for the radical reaction. The two mechanisms are reported, in a very simplified version, in Figure 5.3.

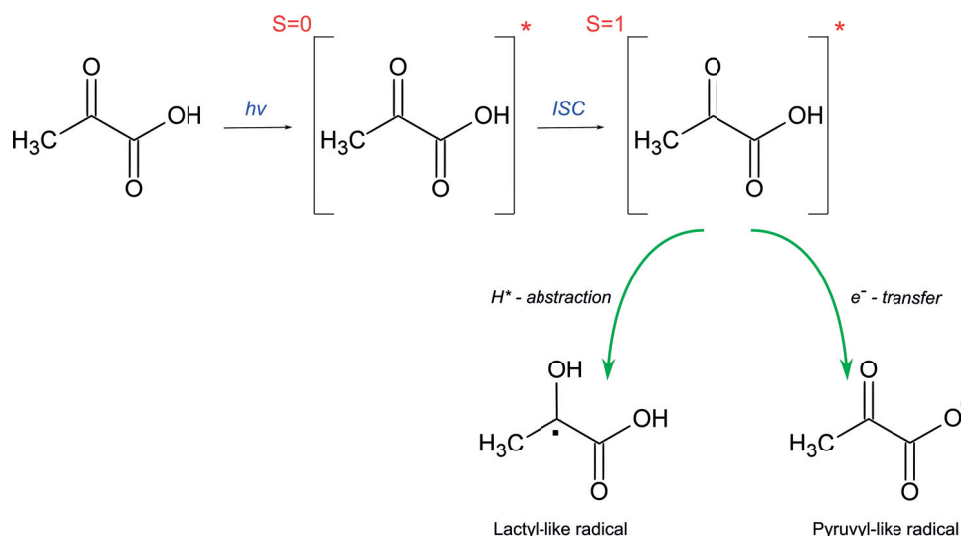


Figure 5.3: Very simplified version of the mechanism yielding to radicals generation from an excited triplet state of a PA molecule. The parenthesis superscript represents the spin multiplicity of the molecular state.

Alternatively to the initiation of a photochemical reaction the excited triplet state can decay to the singlet ground state generating the classic phosphorescence light emission process mentioned above.

It was recently shown that by shining UV-light for one hour on neat PA frozen pellets immersed in liquid nitrogen it is possible to generate a concentration of photo-induced radicals that is large enough to highly enhance the ^{13}C polarization of the substance via DNP. These radicals are non-persistent, indeed they recombine upon dissolution and no-paramagnetic impurities are left in the HP solution employed for HP MRI and MRS [49]. The method offers an elegant alternative to the filtering or the artificial scavenging of the persistent radicals routinely used in dissolution-DNP experiments [105, 111]. Indeed, as already pointed out in Chapter 2, the main drawback of each hyperpolarization technique is the nuclear T_1 -limited lifetime of the HP state which, in the case of dissolution-DNP, is reduced by the presence of the unpaired electrons used for the polarization transfer to the nuclei. Moreover for medical applications, the radicals need to be removed from the final HP solution prior to injection.

In this Chapter, after investigating more deeply the nature and main features of the UV-induced radicals from the ESR point of view, we show that they can be created in frozen solutions containing a fraction of PA and used to efficiently polarize ^{13}C - or ^6Li -salts, as well as ^{129}Xe nuclei therein dissolved. Emphasis is given to the fact that the use of these non-persistent radicals prevents the loss of a substantial part of the liquid state nuclear polarization under unfavorable HP solution transfer conditions.

5.2 UV-radicals for X-nuclei dissolution-DNP

5.2.1 Experimental methods

a. Samples preparation

ESR samples - By means of a micropipet ($1 - 20\ \mu\text{L}$ range), three $8.0 \pm 0.5\ \mu\text{L}$ drops of neat or diluted (in H_2O , EtOH or THF) PA, neat $[1-^{13}\text{C}]\text{PA}$, neat $[2-^{13}\text{C}]\text{PA}$ and neat fully deuterated PA ($d_4\text{-PA}$) were poured, one by one, inside a synthetic quartz dewar (Wilmad 150 mL Suprasil Dewar Flask type WG-850-B-Q) filled with liquid nitrogen. Samples were irradiated for up to 70 min (turning the dewar of 90° every 10 min) using a 1024 mW maximum output power 365 nm LED array (Hamamatsu LC-L5). Once the irradiation process was completed, the dewar was inserted into the ESR spectrometer cavity for measurements.

Carbon DNP samples - To a 2.25 M sodium $[1-^{13}\text{C}]\text{acetate}$ solution, prepared in $\text{H}_2\text{O}:\text{EtOH}$ 1:1 (v/v), was added an amount of PA or $d_4\text{-PA}$ corresponding to 30 % of the total volume to obtain a final 1.5 M acetate concentration. The UV-irradiation procedure was performed as described above for 1 h on about 25 frozen beads ($\sim 200\ \mu\text{L}$ of solution). An additional sample containing nitroxyl radicals as paramagnetic centers was prepared by adding 50 mM of TEMPOL to a $\text{H}_2\text{O}:\text{EtOH}$ 1:1 (v/v) solution

containing 1.5 M of sodium $[1 -^{13}\text{C}]$ acetate.

Xenon DNP samples - following methods that will be extensively described in Chapter 6, liquid xenon was embedded in a 2-methyl-1-pentanol:PA (or d_4 -PA) mixture (with the acid corresponding to 10 % of the final volume) to yield 5 M xenon samples. Once frozen in liquid nitrogen, the samples were extracted from the cold finger and placed into the quartz dewar filled with liquid nitrogen in order to perform UV irradiation for 1 h.

Lithium DNP samples - To a 4.5 M $^6\text{LiCl}$ solution, prepared in $\text{H}_2\text{O}:\text{EtOH}$ 1:1 (v/v), was added an amount of PA corresponding to 30 % of the total volume to obtain a final 3 M lithium concentration. About 200 μL of sample (25 frozen beads) were irradiated at low temperature with UV light for 1 h.

Xenon gas was purchased from Carbagas, Lausanne, Switzerland; all the other chemicals were obtained from Sigma-Aldrich, Buchs, Switzerland.

b. Low-temperature X-band ESR methods

An X-band spectrometer (EMX, Bruker Biospin, Rheinstetten, Germany) was used for all ESR experiments. The tail of the quartz dewar, filled with liquid nitrogen, was placed inside the resonator cavity of the spectrometer. A series of reference ESR signals arising from three $8.0 \pm 0.5 \mu\text{L}$ frozen beads of ethanol containing TEMPO (2,2,6,6-Tetramethylpiperidoxyl) radical at various known concentrations (between 25 mM and 100 mM) were used to calibrate the radical concentration as a function of signal integral (see Appendix B, Figure B.1). The same parameters were kept for all ESR measurements, i.e., center of the magnetic field sweep: 338 mT; sweep range: 30 mT; sweep time: 20 s; modulation frequency: 6 kHz; modulation amplitude: 0.2 mT; microwave output power: 0.063 mW. Parameters were optimized in order to work in the linear range of the detector diode of the ESR spectrometer and to avoid spurious line broad-

ening effects. All measured ESR spectra were fitted using the PEPPER routine of the MATLAB®-based software EASYSPIN [128].

c. Sample transfer into the DNP polarizer

Once the low-temperature UV-irradiation was completed, the frozen beads were quickly transferred from the cold finger into a polystyrene box containing liquid nitrogen. Afterward, the handling of the sample was standard: a polytetrafluoroethylene (PTFE) sample cup was pre-cooled in liquid nitrogen, and the beads were placed inside the cup before it was rapidly inserted into the cryostat prefilled with liquid helium (see [39] for details). The handling of the sample is not problematic since the radicals are stable at liquid nitrogen temperature (77 K). A precise evaluation of their temporal degradation as a function of temperature has however not yet been performed. It must nevertheless be noted that it was possible to perform DNP experiments on irradiated samples stored for months in liquid nitrogen without observing consistent differences in maximum ^{13}C polarization or build-up time constant compared to samples prepared the same day.

d. Solid state and liquid state DNP methods

Solid state DNP measurements were performed using two different custom-built polarizers: one operating at 5 T and coupled to a 14.1 T rodent MRI scanner (Varian, USA) [71], and the other operating at 7 T and coupled to a 9.4 T rodent MRI scanner (Varian, USA) [34, 35]. The 5 T polarizer was used for the ^{13}C and ^{129}Xe DNP experiments whereas the ^6Li DNP experiments were performed using the 7 T polarizer.

Samples containing sodium $[1 - ^{13}\text{C}]$ acetate were polarized at 1.50 ± 0.05 K and 1.15 ± 0.05 K by shining microwaves at a frequency ranging from 139.500 GHz to 140.500 GHz with a nominal output power of 55 mW (ELVA-1, St. Petersburg, Russia). The ^{13}C polarization time evolution was monitored using the home-made NMR setup

already described in Chapter 4 (see also [39] for details), applying a 3° radiofrequency (rf) pulse at 53.44 MHz every 5 min. Once the maximum polarization was reached, a 30° rf pulse was applied and, once the microwaves were switched off and after waiting for a sufficiently long time for complete relaxation of the sample nuclear spin magnetization, an identical 30° rf pulse was applied to measure the reference signal corresponding to the nuclear Boltzmann polarization. The DNP enhancement was obtained by computing the ratio between the two NMR signal integrals. Once polarized, the samples were dissolved and automatically transferred into an injection pump (equipped with a rf probe tuned at 150.25 MHz) located inside a non-actively shielded 14.1 T rodent MRI scanner. The setup and procedures were similar to what reported in [35, 39], with the notable differences that the length of the plastic tube for the transfer of the HP solution was 10 m instead of 5 m and the solution transfer time was set to 5 s instead of 2 s. The ^1H NMR signal was recorded as well, while polarizing the $[1-^{13}\text{C}]$ acetate samples, but in separated experiments. The ^1H signal evolution and DNP enhancement were measured as described above, with the difference that the NMR hardware components (coil, filter and power amplifier) were adapted to 212.50 MHz and the bottom of the insert supporting the sample was entirely made of PTFE to avoid any signal contamination from surrounding protons.

Samples containing ^{129}Xe were also polarized at 5 T and 1.50 ± 0.05 K. Microwaves were shined at a frequency corresponding to the optimal DNP conditions for each radical (139.875 GHz for UV-irradiated PA, 139.925 GHz for UV-irradiated d_4 -PA and 140.300 GHz for TEMPOL see Appendix B, Figure B.2). The ^{129}Xe polarization time evolution and DNP enhancement were measured using a procedure identical to the one used for the ^{13}C experiments, with the difference that the NMR frequency was set to 58.79 MHz.

The ^6Li samples were polarized at 1.50 ± 0.05 K in the 7 T DNP setup. The mi-

microwave frequency was set to the value corresponding to the maximum DNP enhancement (196.750 GHz see Appendix B, Figure B.2) and the nominal output power was 55 mW (ELVA-1, St. Petersburg, Russia). The ${}^6\text{Li}$ polarization time evolution was monitored, using a slightly modified version (adjusted for ${}^6\text{Li}$) of the home-made NMR setup already described in Chapter 4 for ${}^{13}\text{C}$ (see [39] for details), by applying a 5° rf pulse at 43.97 MHz every 5 min. Because of the prohibitively long T_1 , the solid state ${}^6\text{Li}$ DNP enhancement was not evaluated. Once dissolved, the ${}^6\text{Li}$ spin-lattice relaxation time and maximum liquid state polarization were evaluated using a rf probe (tuned at 58.89 MHz) located around a custom-made injection pump, as described in [34, 35, 39]. The HP ${}^6\text{Li}$ signal decay was monitored by applying a 10° rf pulse every 10 s. The thermally polarized NMR signal was measured using the same 10° pulse (16 averages with a repetition time $TR = 5T_1$). The DNP enhancement was obtained by computing the ratio between the signal integral of the first measured spectrum and the thermally polarized spectrum.

5.2.2 Results and discussion

ESR measurements

X-band ESR spectra of UV-irradiated neat PA, $[1-{}^{13}\text{C}]\text{PA}$, $[2-{}^{13}\text{C}]\text{PA}$ and $d_4\text{-PA}$ were collected in order to better understand the nature of the radical species and its spin multiplicity. Results are reported in Figure 5.4. The analysis of panel A, panel B and panel C allows to determine the molecular structure of the photo-induced radical. The three spectra were fitted assuming a $S = 1/2$ spin system; in each of the three cases a tensor $\tilde{g} = [2.0041; 2.0037; 2.0042]$ and a phenomenological dipolar broadening around 1.02 mT turned out to give the best result. More interesting is how the hyperfine coupling changes as a function of the ${}^{13}\text{C}$ labeling of the PA molecule. For

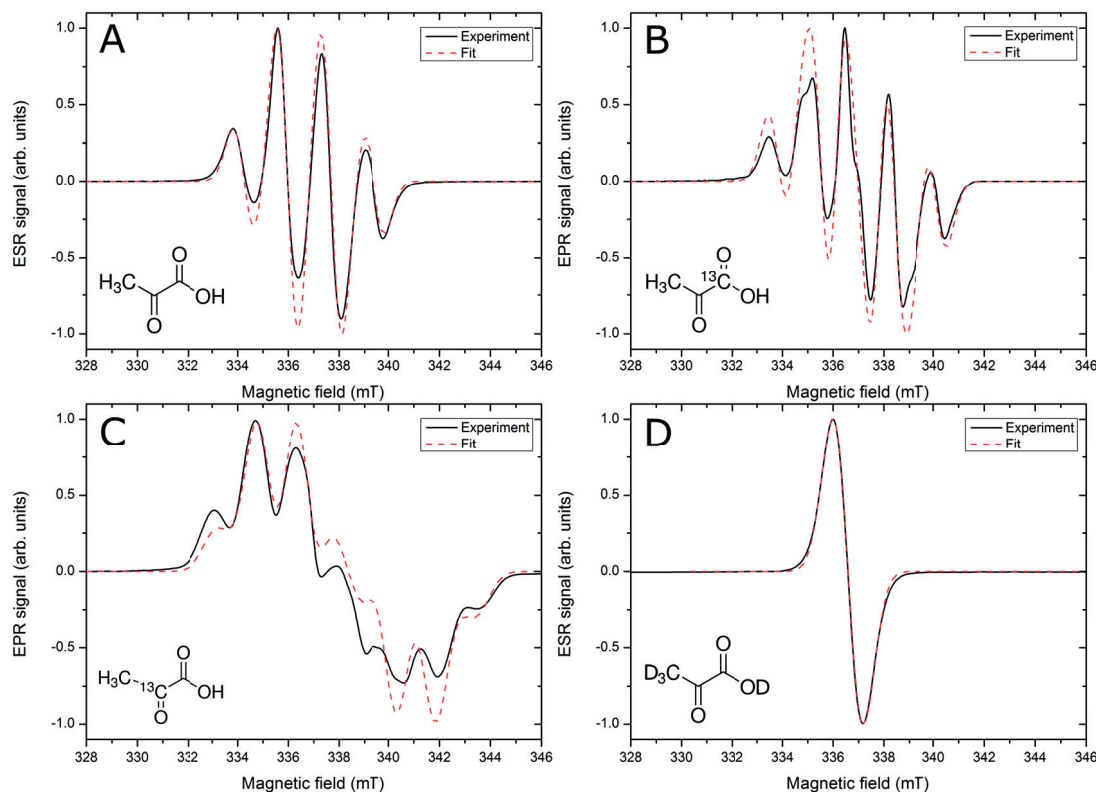


Figure 5.4: X-band ESR spectrum of UV-irradiated neat natural abundance PA (panel A), $[1-^{13}\text{C}]$ PA (panel B), $[2-^{13}\text{C}]$ PA (panel C) and d_4 -PA (panel D) measured at 77 K in $8.0 \pm 0.5 \mu\text{L}$ frozen beads after 60 min UV-light illumination. The measured spectrum (black line) was fitted (dashed red line) in order to evaluate in each case the principal values of the g-tensor, A-tensor and line broadening. In the insets is reported the structural formula of the different molecules.

natural abundance PA an isotropic hyperfine tensor $A_{CH_3}^{\sim} = 1.71 \text{ mT}$ resulting from the coupling of the electron with the three ^1H nuclei of the methyl-group gave the four features spectrum reported in panel A. For $[1-^{13}\text{C}]$ PA the coupling with the ^{13}C nucleus of the carbonyl-group was also considered through a second, slightly smaller, isotropic hyperfine tensor $A_{^{13}\text{C}}^{\sim} = 1.07 \text{ mT}$, giving the result reported in panel B. Panel C pictures the ESR spectrum arising from UV-irradiated $[2-^{13}\text{C}]$ PA; the strong coupling with the ^{13}C nucleus of the ketone-group was expressed by means of the axial tensor $A_{^{13}\text{C}}^{\sim} = [1.75; 1.75; 5.14] \text{ mT}$; the coupling tensor relative to the methyl-group protons presented a slightly axial symmetry as well $A_{CH_3}^{\sim} = [1.43; 1.43; 1.71] \text{ mT}$. From the

analysis of the ESR spectra reported in panels A to C is important to observe that the photo-generation process of the radicals conserves the number and nature of the carbon atoms borne by the PA molecule. Going back to panel C, even though the calculated spectrum cannot exactly reproduce the measured one, a main feature stands out: the coupling with the ^{13}C is about five times larger than in the $[1-^{13}\text{C}]\text{PA}$ case. It is therefore reasonable to think that the photo-induced radical is of the lactyl-like type (see Figure 5.3) with the unpaired electron located on the α -position of the PA molecule. The spectrum relative to UV-irradiated d_4 -PA is reported in panel D. Unlike what has been reported in the literature [59, 58], it was not possible to fit the measured single ESR line assuming a $S = 1$ spin system; the only reasonable fit was obtained for very small values of the zero-field splitting interaction ($\tilde{D} = 0.07\text{ mT}$ and $\tilde{E} = 0.15\text{ mT}$) in contradiction with the fact that, at X-band frequencies, the latter should represent the dominant interaction in systems with $S > 1/2$ [125]. On the other hand, assuming $S = 1/2$ not only the g-tensor and the dipolar broadening were identical to the former three cases, but the isotropic hyperfine tensor relative to the three deuterons, borne by the methyl-group, was found to be $A_{CD3}^{\sim} = 0.26\text{ mT}$. The latter is 6.57-fold smaller than the natural abundance PA A_{CH3}^{\sim} , in good agreement with the proportion between ^1H and ^2H gyromagnetic ratios ($\gamma_{1\text{H}}/\gamma_{2\text{H}} = 6.51$ see Table 2.1).

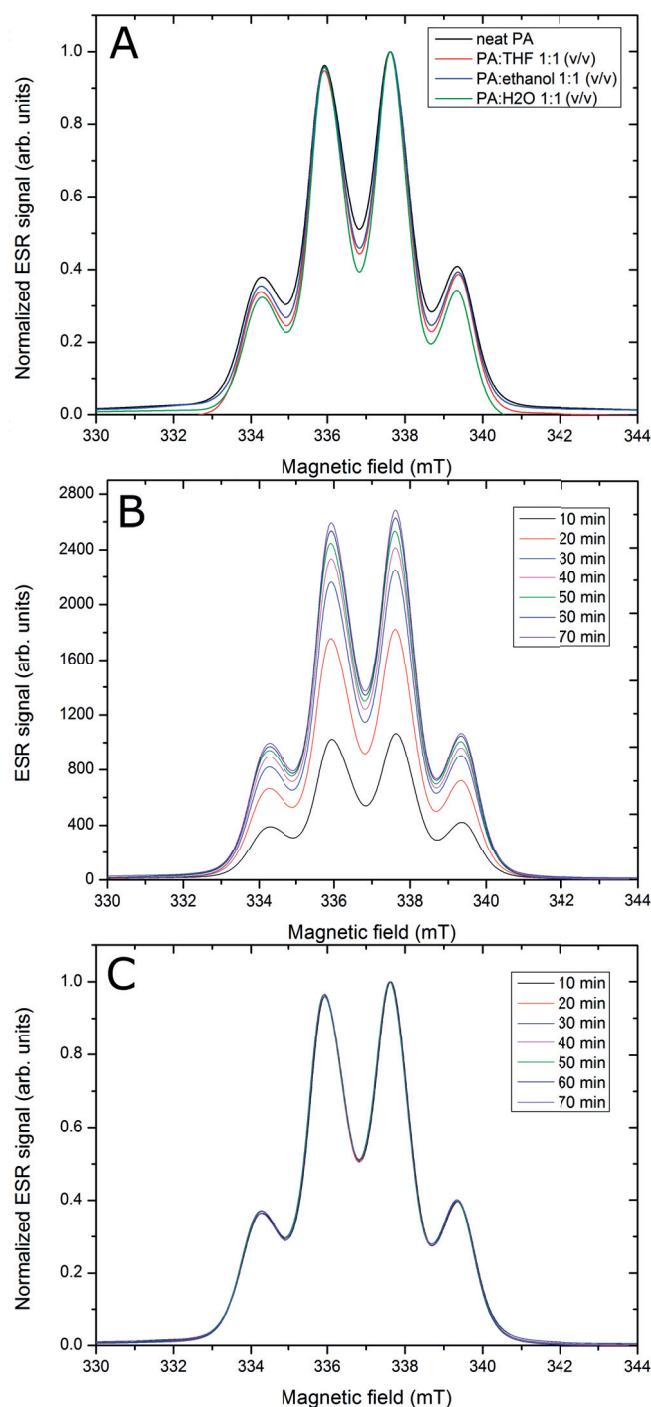


Figure 5.5: Normalized integrated X-band ESR spectrum of UV-irradiated neat PA, PA:H₂O 1:1 (v/v), PA:EtOH 1:1 (v/v) and PA:THF 1:1 (v/v) measured at 77 K after 1 h of irradiation (A). Integrated X-band ESR spectrum of UV irradiated neat PA as a function of the irradiation time in arbitrary units (B) and normalized to 1 (C).

The effect of the chemical environment on the UV-radical structure was investigated on natural abundance PA. Independently of the solvent nature, all the UV-irradiated PA solutions showed very similar ESR spectra (see Figure 5.5A), suggesting that, in all cases, the signal arises from an electron located on a PA molecular orbital. Moreover, it was observed that the broadening of the spectral line is independent of the radical concentration. A representative example is reported in panel B and C of Figure 5.5, where UV-irradiated neat PA ESR spectra, measured at 77 K as a function of the illumination time, are presented. A spectrum was measured after each consecutive 10 min of UV-irradiation and reported in arbitrary units and normalized to 1, respectively. The comparison between the two pictures clearly demonstrates that, if the ESR signal, and thus the radical concentration, increases as a function of the irradiation time, the same does not apply to the line broadening. On the other hand, the latter appeared to be slightly different in the case of UV-irradiated PA solutions, most probably due to the dipolar local magnetic field associated to the different solvents (see Figure 5.5A). The solvent plays a much more important role for what concerns the radical yield. The radical concentration as a function of the UV-irradiation time is shown in Figure 5.6A for neat PA, PA:EtOH 1:1 (v/v) and PA:THF 1:1 (v/v) frozen beads. In all cases, a plateau was reached after about 1 h of UV-irradiation. We suggest that a polar solvent such as ethanol (H_2O relative polarity = 0.654 [92]) increases the radical yield (25.0 ± 1.5 mM) compared to neat PA (15.0 ± 0.7 mM), while a less polar one such as THF (H_2O relative polarity = 0.207 [92]) diminishes it (9.0 ± 0.5 mM). Samples prepared by diluting PA in equal volume with water (27.0 ± 1.5 mM of radical concentration after 1 h UV-irradiation) exhibited a behavior similar to the samples containing ethanol [49].

It has to be noted that PA molecules have the tendency to appear as hydrogen-bond dimers and dimerization increases at low temperature [58].

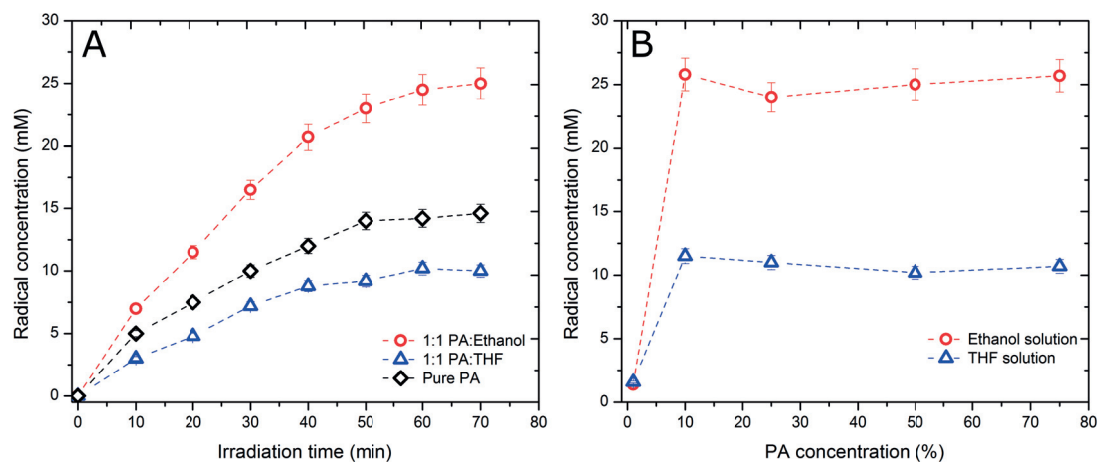


Figure 5.6: (A) Radical concentration generated by low-temperature (77 K) UV irradiation as a function of the illumination time for frozen beads of neat PA (black diamonds), PA:EtOH 1:1 (v/v) (red circles), and PA:THF 1:1 (v/v). (B) Radical concentration generated after 60 min low-temperature (77 K) UV irradiation as a function of the PA concentration in the frozen beads of ethanol (red circles) and THF (blue triangles) solutions. Dashed lines serve as guide for the eyes.

From experimental evidence (see Figure 5.5A), it seems that the solvent is not directly involved in the mechanism generating the UV-induced radical from the excited triplet state of the PA molecule. Thus, we tentatively propose that the photo-reaction involves dimers (or oligomers) of PA molecules only and the solvent polarity affects the formation and available amount of the latter.

A central point for DNP applications is the determination of the minimum PA-to-solvent ratio necessary to obtain a sufficient radical concentration, following UV-irradiation, in particular if PA is not the target substrate to be hyperpolarized. To elucidate this point, the radical concentration was measured, after 1 h of UV-irradiation, as a function of the PA dilution in EtOH and THF solutions (Figure 5.6B). For both solvents, it was observed that the radical concentration is independent of the PA dilution for any PA concentration above 10 % of the total volume, corresponding to a minimum of 1.4 M. A dramatic reduction of the radical concentration was however observed in solutions containing only 1% of PA (i.e. 0.14 M).

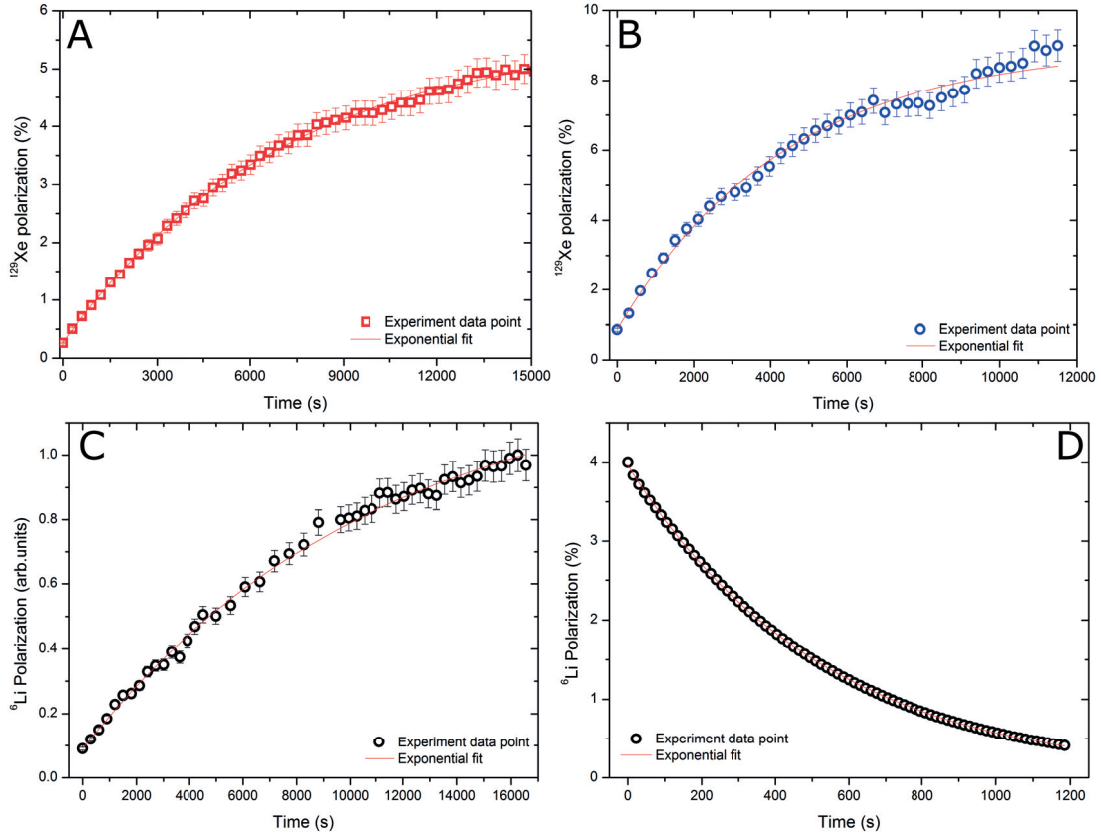


Figure 5.7: Solid state ^{129}Xe polarization build-up curves measured at 5 T and 1.5 K in 5 M xenon samples prepared in (A) a 2-methyl-1-pentanol/PA mixture (10% of PA in the final volume) and (B) a 2-methyl-1-pentanol/ d_4 -PA mixture (10% of d_4 -PA in the final volume). Solid state ^6Li DNP build-up curve measured at 7 T and 1.5 K in a 3 M $^6\text{LiCl}$ sample prepared in $\text{H}_2\text{O}:\text{EtOH}$ 1:1 (v/v) with 30% UV-irradiated PA (A). Liquid state ^6Li signal decay measured in an injection pump placed inside a 9.4 T rodent MRI scanner (B).

DNP measurements

In addition to UV-irradiated natural abundance PA, it is also herein proposed to use UV-irradiated d_4 -PA as DNP polarizing agent because it has been shown that narrower ESR line radicals (see Figure 5.4) lead to higher ^{13}C polarization [40]. In the following, we report experimental results demonstrating that UV-irradiated PA and d_4 -PA can be used as efficient polarizing agent for enhancing the polarization of ^{129}Xe as well as ^6Li and ^{13}C in LiCl and sodium $[1-^{13}\text{C}]\text{acetate}$ frozen solutions, respectively.

As already mentioned ^{129}Xe DNP experiments were performed at 5 T and 1.5 K. A

solid state ^{129}Xe polarization of $5.0 \pm 0.2\%$ was measured after 3 h, about 1.5 times higher than what was obtained using nitroxyl radicals as polarizing agent (see Chapter 6). A representative ^{129}Xe polarization build-up curve is shown in Figure 5.7A. The lithium sample was polarized for 5 h at 1.5 K in our original (now set to 7 T) polarizer and subsequently dissolved prior to transfer into the 9.4 T rodent MRI scanner (Varian/Magnex, Palo Alto, CA, USA) coupled to the polarizer [34]. A liquid state polarization of $4.0 \pm 0.5\%$ was measured in the infusion pump placed inside the scanner bore following the protocol described in a former publication [35]. Even though the polarization value was lower than what is reported in the literature for samples prepared with nitroxyl radicals [63], a remarkably long relaxation time of $519 \pm 25\text{ s}$ was determined, equivalent to the room-temperature ^6Li T_1 measured in thermally-polarized $^6\text{LiCl}$ aqueous solutions at 9.4 T [14]. Results are reported in panel C and D of Figure 5.7.

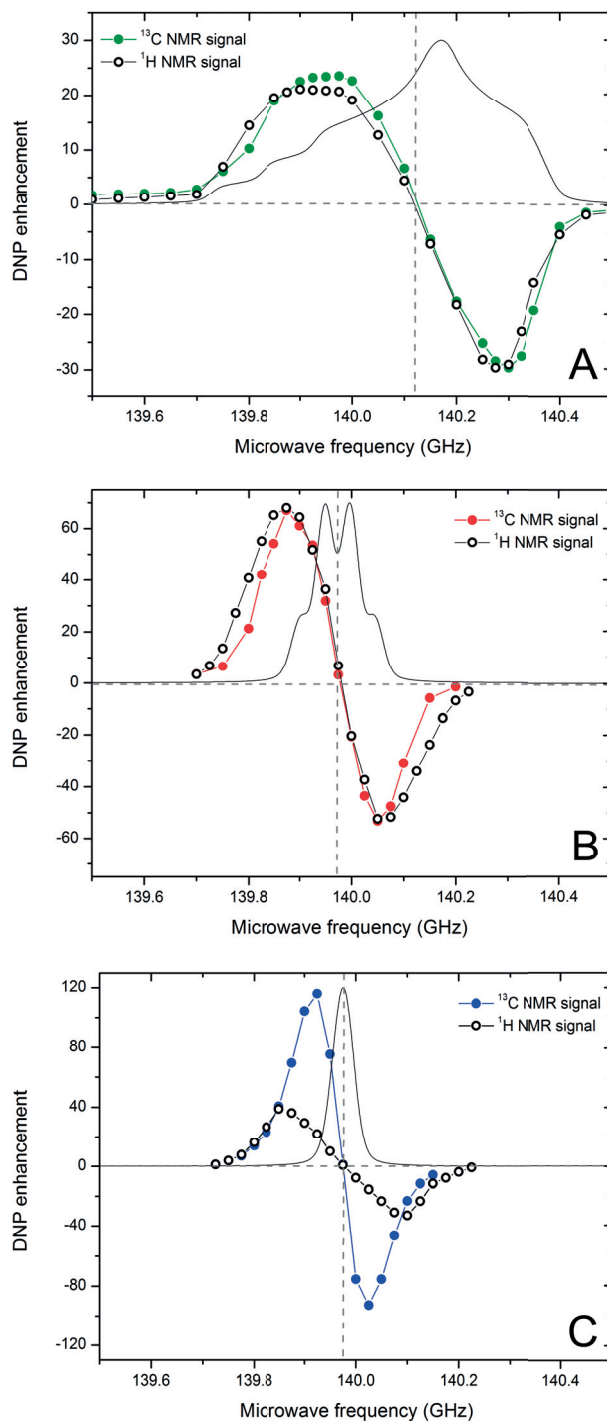


Figure 5.8: ^{13}C and ^1H DNP microwave spectra measured at 5 T and 1.5 K in 1.5 M sodium $[1-^{13}\text{C}]$ acetate samples prepared in $\text{H}_2\text{O}:\text{EtOH}$ 1:1 (v/v) mixtures containing TEMPOL (A), UV-irradiated PA (B), or UV-irradiated d_4 -PA (C). The calculated ESR spectrum, using parameters extrapolated from X-band measurements (see Figure 5.4) for each of the three radical types is superimposed (solid grey lines). The vertical grey dashed lines represents the center of gravity of the ESR spectra.

To investigate in more detail the DNP properties of the UV-induced radicals, sodium $[1-^{13}\text{C}]$ acetate samples were studied. Our analysis relies on the measure of the ^1H and ^{13}C DNP microwave spectra of the three samples reported in Figure 5.8. In a simplified version of the spin temperature theory of DNP [40], radicals are divided into two groups: “narrow ESR line” and “broad ESR line” radicals. Those belonging to the first group will polarize ^{13}C (and other low-gamma nuclei) quite efficiently through the TM mechanism (see Section 3.4), but have poor results in terms of ^1H nuclei polarization because there is smaller chance for the electrons to cross-polarize the latter because of the limited ESR line width with respect to the ^1H Larmor frequency; moreover the optimal microwave irradiation frequency is usually not identical for carbons and protons [138]. Therefore, if the microwave irradiation is set to the optimal frequency for ^{13}C polarization, only a small portion of the electronic “polarization power” is lost to protons. It is thought that this is the reason why the widely-used trityl radicals polarize ^{13}C remarkably well, especially in presence of protonated solvents [99]. Conversely, a “broad ESR line” radical such as a nitroxyl radical will divide its “polarizing power” over all the nuclei present in the sample, that are supposed to reach the same spin temperature at each microwave frequency, leading to lower DNP performance on the targeted low-gamma nuclear species. In good agreement with the latter radical-type definition, the sample containing TEMPOL (Figure 5.8A) exhibits essentially identical spectra for both nuclei, similar to what has been found for the nitroxyl radical porphyrin [24]. At each irradiation frequency ^1H and ^{13}C reach the same polarization enhancement in the stationary state. In a comparative study of five radicals, it was found that replacement of protons in the solvent by deuterons leads to a two- or three-fold improvement of ^{13}C -DNP for “broad-line” radicals, while the reverse effect was found for “narrow-line” radicals [99]. It has been also demonstrated for sodium $[1-^{13}\text{C}]$ acetate dissolved in water/ethanol doped with TEMPO, that the proton and carbon spin temperatures

decrease and remain essentially identical to one other with increasing degree of deuteration [81]. As a consequence, the composition of the sample reported in Figure 5.8A is not optimal for a “broad-line radical”, and a doubling of the enhancement is expected upon deuteration. Further improvement could also be obtained by optimizing the water/ethanol ratio as well as the radical and acetate concentration [81]. The choice of a protonated matrix for the present measurements was made to allow a fair comparison, based on the physical DNP mechanism, between radicals with different ESR line width. The ^1H microwave spectrum in Figure 5.8B is slightly broader than the corresponding ^{13}C spectrum, but the DNP maxima appear at the same frequency for both nuclei. It is therefore likely that the kind of radicals present in this sample exhibits a “broad-line” behaviour, for which deuteration could improve the maximum achievable ^{13}C polarization. From a theoretical standpoint, the sample corresponding to Figure 5.8C is the most interesting. Compared to what was shown in [24] and [138], this is an intermediate case for which the two microwave spectra are clearly distinct, although the proton spectrum is not well-resolved. The ratio between the best ^1H and ^{13}C enhancements is about 3, which is smaller than what was reported in [138] for trityl radicals. At the frequencies corresponding to the extrema of the ^{13}C microwave spectrum of Figure 5.8C, the ^1H enhancement is rather low because most of the “cooling power” delivered by microwaves is spent on polarizing the low-gamma nuclei, in particular ^{13}C . In this case, deuteration is not expected to improve carbon polarization. The difference in maximum ^{13}C polarization enhancement between the samples reported in panel B and C of Figure 5.8 is most likely linked to the two competing effects found in [99].

A similar behavior was found for ^{129}Xe when the UV-irradiated d_4 -PA radical was used: instead of the $5.0 \pm 0.2\%$ polarization mentioned above for the protonated radical, we obtained $9.5 \pm 0.4\%$ with its deuterated form (see Figure 5.7B).

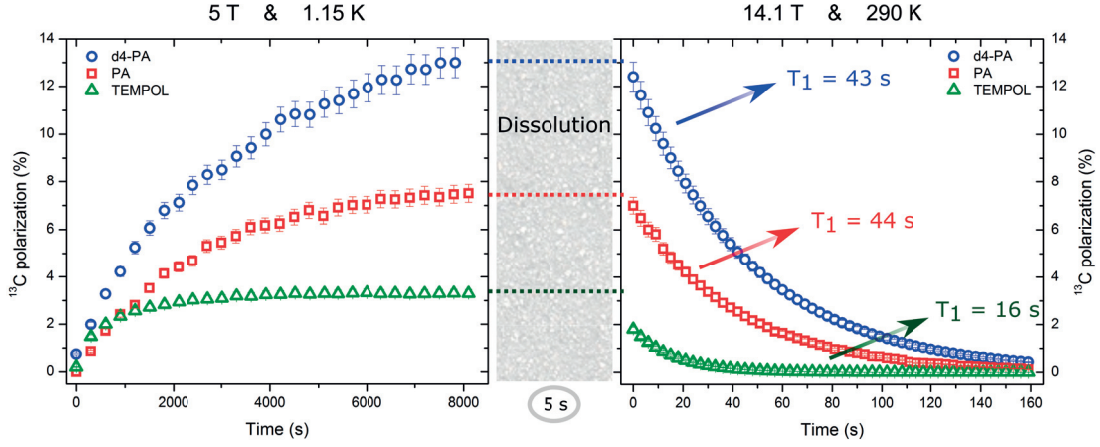


Figure 5.9: ^{13}C DNP build-up curves recorded in a 5 T/1.15 K polarizer (left panel) and room-temperature relaxation curves measured, after dissolution and transfer, in an injection pump placed inside a 14.1 T MR scanner (right panel). The samples consisted in 1.5 M sodium $[1-^{13}\text{C}]$ acetate dissolved in $\text{H}_2\text{O}:\text{EtOH}$ mixtures containing UV-irradiated PA (red squares), UV-irradiated d_4 -PA (blue circles), or TEMPOL (green triangles). Colored dashed lines prolong the NMR signal obtained at the end of the DNP process to visually underline the polarization losses during the transfer; arrows in the right panel indicate the measured sodium $[1-^{13}\text{C}]$ acetate T_1 of each sample in the 14.1 T MR scanner.

It is therefore expected that all low-gamma nuclei will follow this trend. The acetate samples were also used for investigating one crucial point of the dissolution-DNP technique: the transfer of the HP solution from the polarizer to the NMR/MRI system. To minimize the transfer time, the dissolved sample can be driven through a plastic tube from one instrument to the other using compressed He gas [8, 27, 39, 138]. An ill-defined combination of several liquid state relaxation mechanisms may cause loss of polarization along the way and it is generally believed that the path should not pass through regions of very low or very rapidly changing magnetic field values (the so-called adiabatic condition). The above-mentioned issue has been recently studied in some detail for ^1H and ^{13}C [106]. As the UV-induced radical species are entirely quenched when the temperature of the sample is raised up during the dissolution process, there is a disappearance of the main relaxation mechanism causing polarization losses, namely paramagnetic relaxation.

Radical	UV PA	UV d_4 -PA	TEMPOL
Rad. conc. [mM]	25.2 ± 1.3	24.5 ± 1.2	50.0 ± 2.5
Pol. time [s]	2700 ± 270	2950 ± 295	880 ± 88
Solid state pol. [%]	7.4 ± 0.7	13.0 ± 1.3	3.3 ± 0.3
Liquid state pol [%]	7.0 ± 0.3	12.4 ± 0.6	1.8 ± 0.1
Relax. time [s]	44 ± 2	43 ± 2	16 ± 1

Table 5.1: The main parameters concerning the DNP and subsequent dissolution and relaxation of the three acetate samples are reported. From left to right we have in the order the kind of radical, the radical concentration, the polarization build-up time constant, the maximum ^{13}C polarization achieved in the solid state, the maximum ^{13}C polarization measured in the 14.1 T MRI scanner after the HP solution was transferred and the acetate T_1 .

In the herein reported hyperpolarized ^{13}C experiments, the HP solution was transferred into the bore of a non-actively shielded 14.1 T rodent MRI scanner (Varian/Magnex, Palo Alto, CA, USA) from the polarizer located outside of the massive iron shielding structure of the scanner. The ^{13}C polarization build-up measured in the 5 T/1.15 K polarizer is displayed in the left-hand panel of Figure 5.9 (the microwave frequency was set to the optimal frequency determined by the ^{13}C microwave spectrum shown in Figure 5.8). The central panel of the figure pictures the unknown fate of the polarization during the 5 s that it takes to transfer the solution from the polarizer into the infusion pump placed inside the 14.1 T scanner bore [39], where the acetate liquid state ^{13}C polarization decay was monitored (Figure 5.9, right panel) [35]. The essential result is that the polarization created by the two non-persistent radicals was almost entirely maintained throughout the transfer across the complex field path between the polarizer and the scanner (about 5% relative difference between solid state and liquid state ^{13}C polarization); conversely, the sample containing TEMPOL suffered a clear polarization loss of around half of its solid state value. A correlation is that the acetate liquid state ^{13}C T_1 measured in the 14.1 T scanner for the sample containing nitroxyl radicals is much shorter (16.2 ± 0.1 s) than for the other two samples in which the UV-induced radicals quenched at the time of dissolution. Indeed the dissolved UV-irradiated samples

exhibited a T_1 value nearly identical to the value measured for melted non-irradiated PA beads in a 600 MHz high-resolution system (45 ± 2 s). Numerical results are summarized in Table 5.1.

Chapter 6

Hyperpolarized Xenon gas via sublimation-DNP¹

“Entia non sunt multiplicanda praeter necessitatem.”

W. Ockham

In the present Chapter, we will investigate the role played by the solvent, used to form the sample glassy matrix, and by the target nucleus concentration on the efficiency of the dynamic nuclear polarization process. The study is carried out in the context of xenon DNP because of the extreme sensitivity of the ^{129}Xe nucleus towards the surrounding physico-chemical environment. We show that the optimization of the latter together with the addition of a sublimation step allows to produce HP ^{129}Xe gas with polarization levels suitable for biomedical imaging standards. Sublimation-DNP represents a promising alternative technique to the well-established SEOP (see Section 2.3) for the production of HP gases.

¹Partially adapted from A. Capozzi et al., "Optimal Glass-Forming Solvent Brings Sublimation Dynamic Nuclear Polarization to ^{129}Xe Hyperpolarization Biomedical Imaging Standards", J. Phys. Chem. C 2015, 119, 5020-5025.

6.1 Introduction

Among the several nuclear spins that can be efficiently hyperpolarized (HP), ^{129}Xe holds a special place because it is in a gaseous phase in standard conditions of temperature and pressure (298.15 K, 1.00 bar). The application field of HP ^{129}Xe ranges from material science and structural chemistry to medicine [15, 93, 109]. Its value for investigating human lung function has been extensively demonstrated [37], and is more and more established because of the uncertain long-term availability of ^3He [133]. While other contrast agents based on hyperpolarized gases are being developed [80, 126], the long T_1 of ^{129}Xe and its large chemical shift dispersion opened many applications beyond ventilation imaging [109]. Because of its great affinity for hydrophobic molecular environment, HP ^{129}Xe is also a compelling blood tracer for *in vivo* perfusion imaging [36, 47, 140]. Its large chemical shift and T_1 strongly depend on its environment, which make it an attractive candidate for molecular imaging [16, 124, 129]. The availability of hyperpolarized ^{129}Xe is often asserted as the limiting factor to a wider spread of all these applications [133]. The standard technique to hyperpolarize ^{129}Xe - spin exchange optical pumping (SEOP), described in Section 2.3 - can lead to remarkably large maximum ^{129}Xe polarization of up to 95 % (in “stopped flow” or “batch” mode) in diluted gas mixtures containing a small amount of xenon. However, the apparent or usable ^{129}Xe hyperpolarization rate (taking into account the dilution in N_2 gas) is limited to about 30 % [112]. For larger throughputs ($> 2\text{ L/h}$ “continuous flow”), the reported average polarization is around 20 % [122]. This robust technique always requires a dedicated system and is more technically demanding for the “continuous flow” SEOP [64, 123].

In 2010, A. Comment et al. demonstrated that dissolution-DNP could be employed for the production of HP xenon in standard conditions. This only required a minimal hardware modification of the original setup [40] to separate xenon from the other

residual gases (in practice helium used to push HP xenon out of the polarizer) and the sample solvent (the so called cryo-collection). This technique is called sublimation-DNP [41]. The intrinsic advantage of DNP over SEOP is that the volume of xenon that can be produced in a single experiment is potentially much larger due to the more than 500 times higher density of solid xenon as compared to the xenon gas phase. However, the homogeneity of the solid state xenon preparations is a critical feature required for DNP and the achievable polarization level can be dramatically limited in inhomogeneous samples, questioning the practical application of this technique [83]. We herein show that the maximum xenon volume and achievable ^{129}Xe polarization strongly depends on the physico-chemical properties of the glass-forming agent in which xenon is embedded, and that sublimation-DNP could compare favorably with SEOP when sample preparation is optimized.

6.2 Experimental methods

As already explained in Section 2.5, the DNP sample has to be characterized, in the solid state, by an amorphous (or glassy) phase. This feature not only insures a homogeneous distribution of radicals, but also promotes spectral diffusion (see Section 3.3.1) by forcing nearest neighbor molecules to be randomly oriented with respect to one another and thus strong interactions between electron spins with large resonance frequency difference. This feature is undoubtedly the most critical feature to efficiently perform solid state DNP [11, 13]. In the case of xenon, the amorphous solid is formed by a host frozen solvent in which liquid xenon has been dissolved [41, 83]. In addition to be glass forming, the solvent has to dissolve the adapted concentration of radicals (typically tens of mM). Its melting point has to be in a range compatible with the xenon triple point (161.40 K and 0.82 bar) [92]. Three solvents with different polarity and suitable melting

Solvent	Ethanol	2-methyl-1-propanol	2-methyl-1-pentanol
Melting point [K]	159	165	143
log P _{OW}	−0.180	0.683	1.702
Xe sol. threshold [M]	1.5	5	8.2
¹²⁹ Xe freq. shift [ppm]	119	85	51
¹ H density [nuclei/cm ³]	6.18×10^{22}	6.51×10^{22}	6.82×10^{22}

Table 6.1: Main physico-chemical properties of the three solvents considered in the present study. The partition coefficient log P_{OW} at 25 °C is an indication of the polarity of the solvent [92]; the xenon solubility threshold (ST) represents the highest xenon concentration generating a homogeneous solid state NMR spectrum for a given solvent; the frequency shift is defined as the spectral separation in the solid state ¹²⁹Xe NMR between the sharp peak always appearing at 58.788 MHz and corresponding to pure solid xenon, and the broad down-field peak.

point were chosen for the present study (see Table 6.1). Besides 2-methyl-1-propanol, which was used in the original study [41], ethanol and 2-methyl-1-pentanol were also investigated. For each solvent, five samples with different xenon concentration (between 1 M and 10 M) were prepared. The sample preparation procedure is sketched in Figure 6.1. The xenon gas bottle was connected to a custom-designed glass cold finger equipped with a pressure gauge and an overpressure valve (panel A). 500 μ L of solvent doped with TEMPO (2,2,6,6-Tetramethylpiperidoxyl) nitroxyl radicals were placed in the glass cold finger (panel B). The radical concentration was adjusted to obtain a final value of 50 mM in the frozen sample. The cold finger was filled with a well-defined volume of xenon gas at adjustable pressure (panel C); the desired xenon concentration in the sample was obtained by varying the xenon gas pressure above the liquid between 0.5 bar and 5 bar (corresponding to a gas volume at atmospheric pressure between 20 mL and 200 mL). To force xenon gas to condense and diffuse throughout the solvent, the temperature of the cold finger was gradually lowered using cold nitrogen gas (panel D); a magnetic stirrer was used to homogenize the liquid mixture. At the end of the process, the pressure dropped to zero, meaning that essentially all the xenon was incorporated into the solvent (panel E). The cold finger was then plunged into liquid nitrogen before extracting the frozen sample (panel F). A sample volume of about 0.40 mL (out of

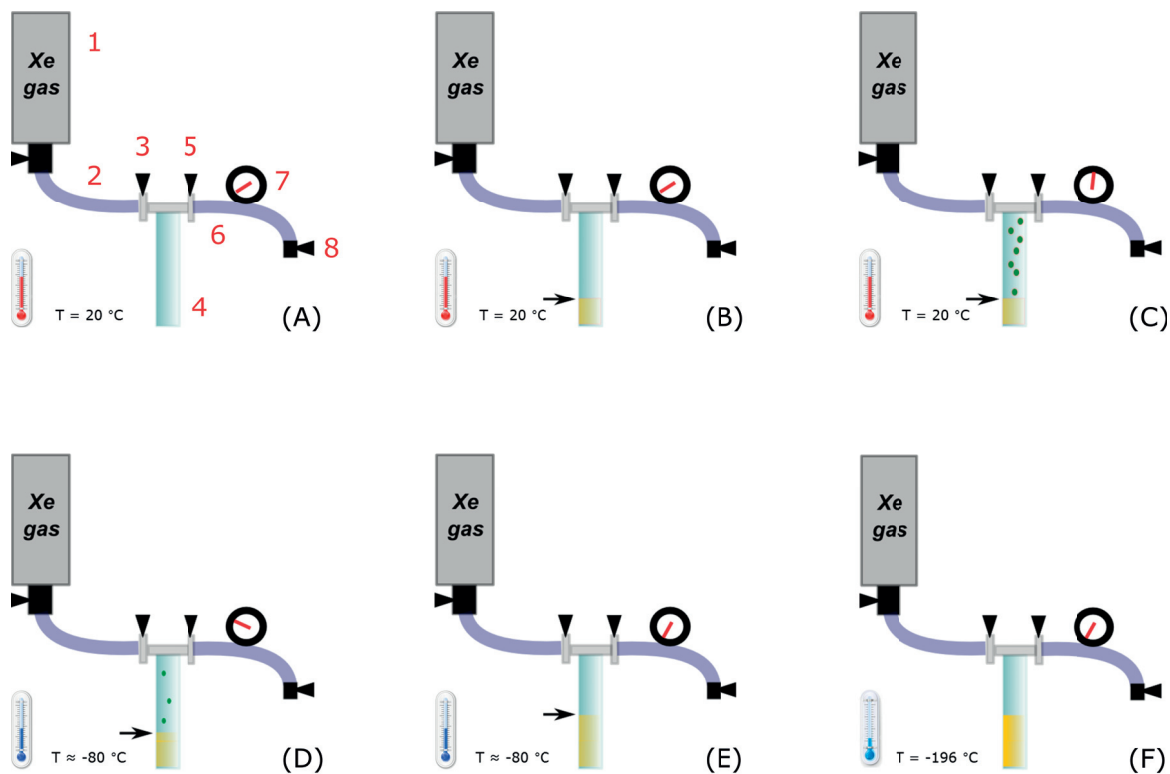


Figure 6.1: Panel A pictures the experimental setup composed by a natural abundance xenon gas bottle (1), one leak-tight plastic pipe (2), one gas inlet valve (3), a custom-designed glass cold finger (4), one gas outlet valve (5), a second leak-tight plastic tube (6), one pressure gauge (7), one over pressure valve (8). For the description of the sample preparation procedure (panel B to panel F) refer to the text.

0.53 mL – 0.86 mL, depending on the applied xenon pressure) was rapidly transferred into the DNP polarizer. All samples were polarized in the 5 T home-built DNP polarizer following methods previously described in Chapter 4 and Chapter 5 (see [40, 39, 71] for details). Unless differently stated, the experiments were performed at 1.50 ± 0.05 K using 55 mW microwave output power at 140.3 GHz (according to the DNP microwave spectrum relative to TEMPO, see Figure 5.8A). The ^{129}Xe polarization build-up was monitored using a dedicated home-built NMR spectrometer and a remotely tuned and matched low temperature ^{129}Xe probe by applying a 2° flip-angle rf pulse every 5 min. Once the polarization plateau was reached, a 20° flip-angle pulse was applied and the signal integral was compared to the one measured with the same pulse after relaxation

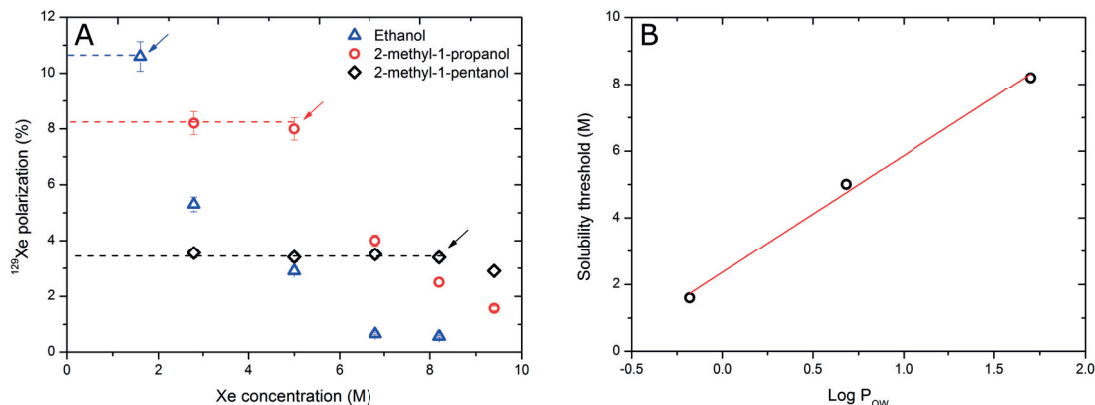


Figure 6.2: (A) Solid state ^{129}Xe polarization obtained by DNP at 5 T and 1.50 ± 0.05 K in natural-abundance xenon dissolved in different solvents, namely ethanol (blue triangles), 2-methyl-1-propanol (red circles), and 2-methyl-1-pentanol (black diamonds) doped with 50 mM TEMPO. For each solvent, an arrow points to the “solubility threshold” (ST) defined as the maximum xenon concentration for which the solid state ^{129}Xe NMR spectrum is characterized by a single peak; in samples containing a xenon concentration lower than ST, the maximum polarization is independent of the concentration as highlighted by the dotted lines. (B) Solubility threshold plotted as a function of the log P_{OW} characteristic of each one of the three solvents (see Table 6.1); data were fitted using a linear regression (red line, $R^2 = 0.992$).

to thermal equilibrium. The solid state DNP enhancement factor ε was obtained from the ratio of these two measurements. The ^{129}Xe enhanced polarization was deduced by multiplying the theoretical one corresponding to Boltzman thermal equilibrium at 5 T and 1.5 K by ε .

6.3 Results and discussion

The maximum ^{129}Xe polarization was measured as a function of xenon concentration in the three different solvents (see Figure 6.2A). For an amount of gas below a certain solvent-dependent threshold (denominated ST for “solubility threshold”), the maximum achievable polarization is essentially independent of the xenon concentration, but it dramatically drops when it is larger than ST. The ST for ethanol, 2-methyl-1-propanol and 2-methyl-1-pentanol was determined to be 1.5 M, 5 M and 8.2 M respectively. These values correlate nicely with the polarity of the solvents (Figure 6.2B), which is quantified

by their partition coefficient through the $\log P_{OW}$ at 298.15 K (-0.180 for ethanol, 0.683 for 2-methyl-1-propanol and 1.702 for 2-methyl-1-pentanol [92]). If an amount of xenon larger than the solvent ST is incorporated into the sample, the solid state ^{129}Xe NMR spectrum exhibits a striking feature: a sharp peak superimposed onto the relatively broad peak characteristic of samples containing a xenon concentration below the ST. As an example, the ^{129}Xe NMR spectrum corresponding to a sample prepared with 8.2 M of xenon dissolved in 2-methyl-1-propanol is given in Figure 6.3: a broad (full-width at half-maximum $\text{FWHM} = 11.5 \pm 0.5 \text{ kHz}$) peak was observed at 58.783 MHz, 85 ppm away from a sharp ($\text{FWHM} = 0.9 \pm 0.1 \text{ kHz}$) up-field peak at 58.788 MHz. This spectral feature was also observed even in the absence of radicals (Figure 6.2-purple curve), confirming that the frequency shift is a characteristic of the solvent. In the radical-doped samples, the evolution of the two peaks under microwave irradiation is dramatically different, the sharp peak exhibiting a nearly four-fold smaller maximum ε and a longer build-up time constant as compared to the broad peak (see Appendix C). Similar spectra were also measured for the other two solvents (see Figure D.2).

The broad peak corresponds to the ^{129}Xe signal from xenon homogeneously dissolved into the glass-forming solvent while the sharp peak, which always appears at the same frequency (58.788 MHz) in all samples for all solvents, is attributed to the resonance of ^{129}Xe in pure xenon crystals formed during sample preparation and embedded into the glassy matrices [51]. The presence of these crystalline structures could be visually observed since, unlike for homogeneous samples which are transparent and resistant to mechanical stress, the inhomogeneous samples show a certain degree of opalescence and tend to crumble. It was also observed that the larger the frequency shift between the two peaks, which depends on the solvent, the smaller the ε associated with the sharp peak. This can be explained by the fact that a larger frequency shift difference leads to a smaller probability of flip-flop transitions between ^{129}Xe spins of the two

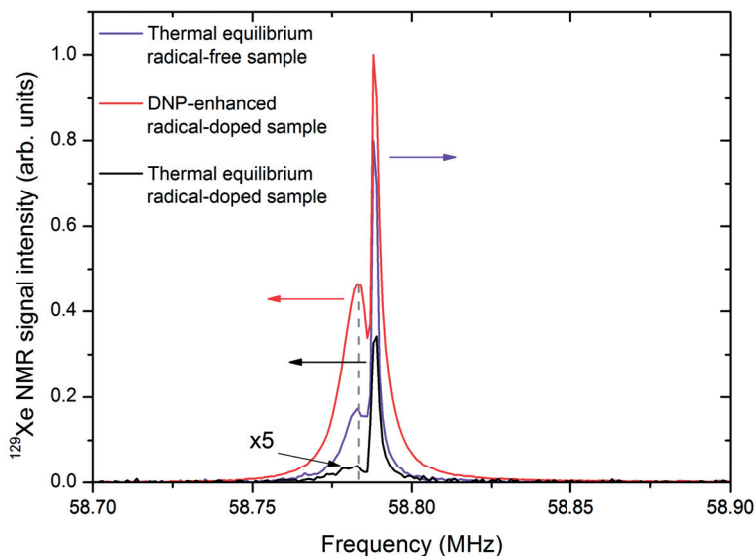


Figure 6.3: Solid state ^{129}Xe NMR signal measured at 5 T and 1.50 ± 0.05 K in a sample containing 8.2 M natural-abundance xenon dissolved in 2-methyl-1-propanol with or without radical (50 mM TEMPO). Both samples were measured at thermal equilibrium (purple and black curves), and the radical-doped was also measured after 90 min of microwave irradiation (red curve). Note that the frequency shift difference between the two peaks is identical in all three measurements and that the intensity of the purple spectrum is not scaled relatively to the red and black spectra.

different compartments. The xenon spins that are associated with the sharp peak are polarized via spin diffusion [83, 117], and they act as a “load” for the entire nuclear spin system leading to a reduction in DNP efficiency and hence resulting in a lower global enhancement factor. For all samples containing a xenon concentration below the ST, the ^{129}Xe solid state NMR spectrum exhibited a symmetric shape but its line width and mean frequency shift were dependent on the solvent (Figure 6.4A). The line width is dominated by the dipolar broadening induced by the solvent ^1H spins (see Appendix C). The frequency shift increases with increasing solvent polarity, i.e., decreases with increasing $\log P_{\text{OW}}$ (Figure 6.4B), because the electron shielding in xenon dissolved in isotropic solvent is an increasing function of the permanent electric dipole of the solvent (ethanol = 1.69 D, 2-methyl-1-propanol = 1.64 D, and 2-methyl-1-pentanol = 1.48 D) [75, 139].

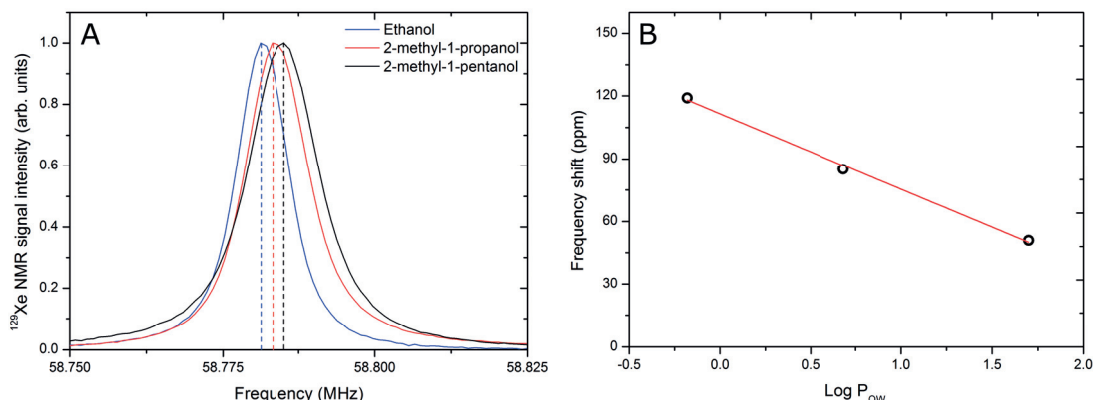


Figure 6.4: (A) DNP-enhanced solid state ^{129}Xe NMR spectra measured in samples containing 50 mM TEMPO and a xenon concentration corresponding to the ST of each of the three solvents considered in the present study, i.e., 8.2 M for 2-methyl-1-pentanol (black line), 5 M for 2-methyl-1-propanol (red line), and 1.5 M for ethanol (blue line). (B) ^{129}Xe frequency shift from the reference resonance of pure solid xenon as a function of the $\log P_{\text{OW}}$ for the three solvents along with a linear fit ($R^2 = 0.995$).

A complete characterization of the strong dependence of the maximum achievable polarization on solvent characteristics is beyond the scope of this work, but it is clear that the ^1H density in the glassy frozen matrix plays a role when broad ESR line width radicals such as TEMPO are used (see Section 3.4 for the "heat capacity" concept). As already pointed out in Chapter 4 and 5, reducing proton density through deuteration leads to increased maximum ^{13}C polarization at 5 T when nitroxyl radicals are used. Among the three solvents considered in the present study, the longer the alcohol chain the larger the ^1H concentration (see Table 6.1). We observed that solvent deuteration also leads to increased ^{129}Xe polarization: the maximum ^{129}Xe polarization obtained at 1.50 ± 0.05 K and 5 T in a 1.5 M xenon sample increased from 10.6 ± 0.5 % to 18.1 ± 0.9 % when ethanol was replaced by d_6 -ethanol (see Figure 6.5).

The ^{129}Xe polarization in this sample was further improved by reducing the working temperature to 1.15 ± 0.05 K to reach a ^{129}Xe nuclear polarization of about 30 ± 1 % ($\varepsilon = 295 \pm 10$) within 90 min (see Figure 6.6A). 15 mL of hyperpolarized xenon gas at atmospheric pressure was extracted following the previously described sublimation

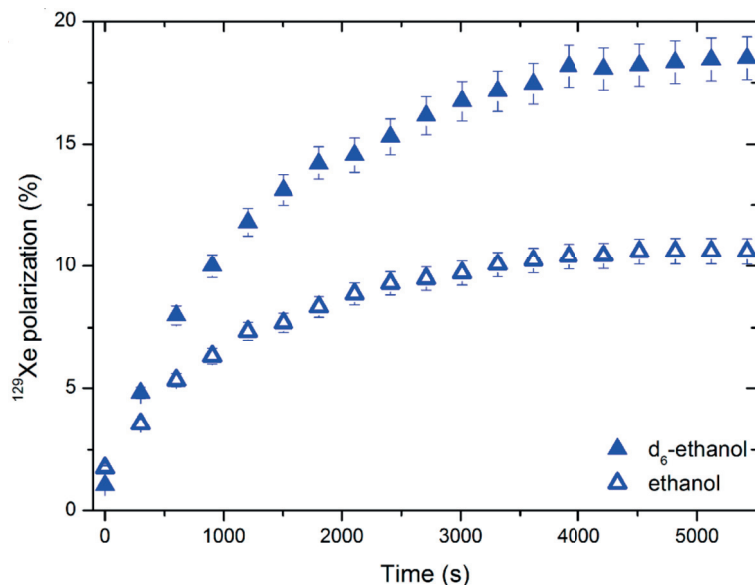


Figure 6.5: ^{129}Xe polarization evolution measured at 5 T and 1.50 ± 0.05 K under microwave irradiation at 140.3 GHz with 55 mW output power in samples prepared with ethanol or d_6 -ethanol containing 50 mM TEMPO and 1.5 M xenon.

procedure [41]. A 10 mL Luer lock plastic syringe was filled with the hyperpolarized gas and measured in the distant 9.4 T rodent MRI scanner (Varian, USA) located about 30 m away from the 5 T DNP polarizer and equipped with a ^{129}Xe Alderman-Grant rf coil (Figure 6.6B). Pulse calibration was performed on a 9.00 bar xenon gas sample placed in a high-pressure 10 mm NMR tube (Wilmad, USA). A single loop ^1H surface coil placed inside the ^{129}Xe volume coil was used for shimming on a water phantom. Before the acquisition, the syringe containing the HP gas was pressurized to 5.00 bar. Time evolution of the HP ^{129}Xe signal was measured using a series of 9° rf pulses with a repetition time (TR) of 10 s. After having corrected for the effect of the rf pulses (similar to what is described in Appendix B), a T_1 of 80 ± 2 s was deduced (Figure 6.6C). A ^{129}Xe image of the syringe was acquired using a frequency selective 3D balanced steady state free precession (bSSFP) sequence [49] with a flip angle of 22° and a TR of 5 ms (Figure 6.6D). The ^{129}Xe polarization at the time of the MRI measurements was lower than the value measured in the solid state. Because of the cryo-collection procedure

employed after dissolution to separate xenon gas from the helium used for propelling out from the polarizer the HP sample [41], up to half of the ^{129}Xe polarization can be lost [82]. Moreover the gas was transported from the polarizer to the 9.4 T scanner in a non-optimized receptacle (plastic syringe without permanent magnet). These losses were however determined to be less than 50 %. To provide the reader with a fair comparison between sublimation DNP and SEOP techniques, we calculated the main parameters proposed by P. Nikolaou et al. (Table 1 of [112]). The maximum ^{129}Xe polarization $P_{Xe}(max) = P_{Xe}(app)$, measured in the sample prepared with ethanol is 30 % (the partial pressure factor being equal to 1 for sublimation-DNP), is lower than the maximum values reached by SEOP. The calculated maximum magnetization $M_{Xe}(max)$ is nevertheless similar ($M_{Xe}(max) = 13.4 \pm 0.4$ mM for the sample prepared with ethanol)² because, unlike for SEOP, there is no inherent need to mix the xenon gas with nitrogen or helium for the production of HP ^{129}Xe by sublimation-DNP. In our experiments, the extracted batch volume after 90 min of polarization was 14.1 mL for the sample containing ethanol, 48.7 mL for the sample with 2-methyl-1-propanol, and 79.1 mL for the sample with 2-methyl-1-pentanol, corresponding to a production rate of 0.009 L/h, 0.032 L/h, and 0.053 L/h, respectively. This low production rate could however be improved by increasing the solid state sample volume.

²In ref. [112] the maximum magnetization $M_{Xe}(max)$ is defined as the product between the xenon concentration C and the maximum polarization $P_{Xe}(max)$. In our case $C = 44.9$ mM (corresponding to xenon gas concentration at room temperature and atmospheric pressure), while $P_{Xe}(max) = 30 \pm 1$. Thus $M_{Xe}(max) = C \cdot P_{Xe}(max) = 13.4 \pm 0.4$ mM.

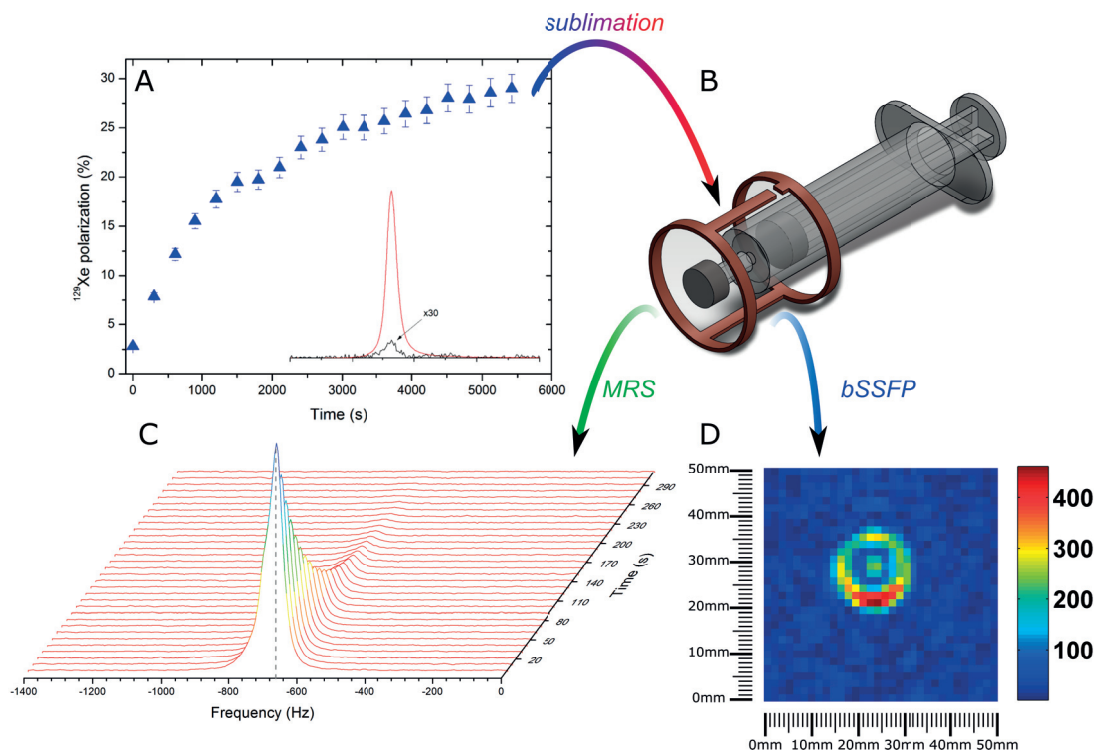


Figure 6.6: (A) ^{129}Xe polarization build-up curve measured at 5 T and 1.15 ± 0.05 K in a 1.5 M xenon sample dissolved in d_6 -ethanol containing 50 mM TEMPO; inset: DNP-enhanced (red) and thermal equilibrium (black) ^{129}Xe NMR spectra measured to determine the ^{129}Xe polarization. (B) Phantom composed of a 10 mL plastic syringe inserted into a ^{129}Xe Alderman-Grant coil for measuring the hyperpolarized gas signal at 9.4 T in the rodent MRI scanner; a ^1H surface coil (not shown) was used for shimming. (C) HP ^{129}Xe NMR spectra measured every 10 s following a 9° flip-angle rf pulse; the frequency reference was set to the resonance measured in a 9×10^5 Pa phantom. (D) ^{129}Xe image representing a 20 mm thickness transversal section of the syringe shown in (B) obtained using a frequency selective bSSFP sequence with a flip angle of 22° and a TR of 5 ms; the color scale is in arbitrary units. The spatial resolution is $1.7 \text{ mm} \times 1.7 \text{ mm}$ (no interpolation) corresponding to a $50 \text{ mm} \times 50 \text{ mm}$ field of view and a 32×32 k-space matrix.

Indeed for human lung MRI applications or to establish a centralized production of HP ^{129}Xe gas, it should be possible to increase the sample volume by a factor up to 20 without any dramatic loss in polarization level or increase in polarization time, as was the case for samples containing ^{13}C -labeled compounds [43, 114]. This would allow producing batches of 300 mL – 1600 mL HP xenon gas, depending on the solvent used for the sample preparation. Note that, although residual vapor of ethanol or

other alcohol widely and routinely used in clinical environment should not be a major issue, the purity of the extracted gas would have to be checked prior to move to human applications.

Chapter 7

Conclusions and perspectives

“Acta est fabula.”

O. Augustus

Dissolution-DNP is a powerful and versatile technique allowing to hyperpolarize a variety of nuclear species to levels suitable for clinical and pre-clinical applications. The efficiency of the process is influenced by several features ranging from fundamental physics to technology development. The main results of the present work are summarized and discussed in this concluding Chapter.

7.1 The influence of the magnetic field on the DNP process

In Chapter 4, the dependence of the DNP process efficiency on the magnetic field strength was studied. From fundamental considerations of DNP, namely dynamic cooling and thermal mixing processes, two qualitative predictions can be made: in the

stationary state, all nuclei present in the sample polarize to the same spin temperature (if the ESR line is wide enough so that equation (3.40) has a sizable value for all nuclei), and for the solute molecules a higher polarization will be obtained if the solvent is deuterated (because at constant dynamic cooling power, the heat capacity in equation (4.1) diminishes). We found that for acetate dissolved in glycerol/water solvents using TEMPOL as radical, these general predictions apply to the DNP of ^{13}C and ^1H for a value of the magnetic field up to 5 T.

We confirmed that for ^{13}C , when a 7 T field is applied, a complete deuteration of the glassing matrix does not necessary lead to higher nuclear polarization in DNP samples doped with nitroxyl radicals (see also [34]). We also showed that the concept of equal spin temperatures for ^{13}C and ^1H is no more valid. These effects are specific to the glycerol/water-based matrix, since it is known from the literature that for ethanol/water solvents at 7 T, the maximum achievable ^{13}C polarization benefits from preparation of the DNP sample with D_2O and d_6 -ethanol, instead of their protonated counterparts [34]. Moreover the fully deuterated ethanol/water solvent shows equal spin temperatures for carbon and proton nuclei [69].

It should be noted that in order to highlight the very peculiar behavior of the DNP in glycerol/water solvents at 7 T, we only need qualitative arguments and we have attempted to explain the quantitative polarizations that have been reported. The existing DNP theories do not contain parameters that are explicitly molecular-specific; but implicitly it is required that a good homogeneous glass is formed. Very tentatively, we might suggest that glycerol/water has some peculiarities in this respect that only show up at the highest fields, when all processes slow down considerably, so that a very homogeneous distribution of the components (water, glycerol, radicals, solute) becomes important for the DNP process efficiency; but we did not pursue a detailed study on the mesoscopic properties of each specific glassy matrix.

The overall conclusion of our findings is that, when broad-line radicals are used, high-field DNP requires a more careful analysis of the sample composition effect, in order to achieve high and fast direct low-gamma nuclei polarization. On the other hand, DNP by cross-polarization could represent a valid alternative in the same experimental conditions [69]. Because of the fast dynamics and high enhancement shown by protons, transferring 1H nuclei polarization to low-gamma ones allows to achieve larger spin order in a shorter time for e.g. ^{13}C and 6Li [25, 94].

7.2 UV-induced non-persistent radicals

In Chapter 5, it was shown that radicals created by UV-irradiation of pyruvic acid exemplify a low-cost and versatile way for polarizing X-nuclei in molecules that can be co-dissolved, together with a fraction of PA, in a medium with a polarity comparable to that of water. Moreover, the self-quenching property of these radicals upon dissolution offers a promising solution for simplifying the HP liquid transfer procedure from the polarizer to a high-field MRI scanner with minimal polarization losses. An additional advantage of the automatic elimination of the radical species (potentially toxic) during dissolution could in principle be to simplify the quality control procedure required for clinical applications. Even though at the present stage of the work the radical concentration obtained after UV-irradiation of PA is still rather low to efficiently perform DNP at high magnetic field, other biocompatible solvent systems are under investigation to improve the radical yield. Furthermore we are directing our efforts in the research or synthesis of new molecules with the same photochemical properties than PA, but with a more isolated molecular environment at the site of the unpaired electron. A reduced hyperfine coupling between the latter and surrounding nuclei would produce a sharper ESR line radical species, as in the case of d_4 -PA. Increasing the radical yield, or even

the discovery of other UV-induced radicals, will provide a more generic improvement of the method for a widespread use of non-persistent radicals for DNP. Concerning the practical applications of this new technique, it is important to note that the liquid state measurements were done inside an injection pump designed for *in vivo* rodent experiments, meaning that all liquid state values reported for ^{13}C and ^6Li nuclei correspond to the polarization levels at the time of injection and, although these values are not the highest obtained to date, they are sufficient for performing *in vivo* studies and, after dissolution, the HP liquid samples have the advantage to be free of radicals [49].

Moreover the radical distribution inside the DNP sample's frozen beads, after low-temperature UV-irradiation, is still unknown. The non-mono-exponentiality behavior of the polarization build-up, upon microwave irradiation, could suggest that radical molecules are induced only on the surface of the bead, polarizing nuclear spins in close vicinity; then the nuclear polarization is transferred to the core through spin diffusion.

Furthermore, we believe that the UV-radicals unique property of self-quenching, when the temperature is increased, could represent the first step towards the development of a simple way to handle and store nuclear polarization, by means of the generation of highly polarized radical-free solid samples. Indeed, it is reported in the literature that the ESR signal arising from low-temperature UV-irradiated PA disappears around 190 K, temperature related to the onset of ice diffusivity and far below the compound melting point (285 K) [58]. Moreover, M. L. Hirsch et al., with their "brute-force" hyperpolarization method, recently demonstrated that it is possible to extract a radical-free polarized solid-state sample from the cryostat placed inside the superconductive magnet (used for reaching the low-temperature/high field required conditions). Since a ^{13}C T_1 of 1 h (24 h) was measured in frozen $[1-^{13}\text{C}]\text{PA}$ at 2 T and 50 K (10 K) [66] we aim at quenching the UV-radicals in the solid state. It should indeed be possible to take advantage of both the high and relatively fast building (when compared

to "brute force") ^{13}C polarization attainable via DNP and the slow solid state relaxation guaranteed by the absence of paramagnetic impurities.

7.3 HP ^{129}Xe gas via sublimation-DNP

In Chapter 6, we demonstrated that the DNP process efficiency dramatically depends on the homogeneity and content of ^{129}Xe -based samples. The xenon concentration has to be optimized in order to hyperpolarize as much ^{129}Xe spins as possible without challenging the quality of the amorphous phase favored by the glassing agent. The nature of the latter, in terms of isotopic distribution and chemical structure, is crucial: the solid state ^{129}Xe polarization ranged from about 3.5 % to 18 % with a strong dependence on the level of deuteration and the length of the solvent alcohol chain. Fine tuning of these parameters allowed to produce HP ^{129}Xe with a polarization that is competitive with SEOP, reaching the requirements of advanced biomedical applications.

Further improvements in the xenon magnetization level might be obtained by using a narrower ESR line radical such as trityl or UV-induced species (as demonstrated in Chapter 5). In this framework, it could be expected that by using 2-methyl-1-pentanol, or even longer chain alcohols, it should be possible to take advantage of both xenon high solubility and large polarization. Indeed, the larger number of molecular ^1H nuclei, which increases the Zeeman nuclear heat capacity in case of broad ESR line radicals, would not affect the DNP process if narrow ESR line ones are employed. Moreover, replacing natural abundance xenon by ^{129}Xe -enriched xenon would generate a twofold advantage: enhancing the spin diffusion rate inside the glassy matrix, thereby reducing the polarization time constant, and reducing the solid state $^{129}\text{Xe} - ^{131}\text{Xe}$ cross relaxation rate, thus increasing the maximum achievable ^{129}Xe nuclear polarization [85].

From a more practical point of view, it should also be mentioned that the sublimation-

DNP method could be easily implementable on commercially available dissolution-DNP polarizers. These systems are within the same price range as a commercially available SEOP apparatus dedicated to xenon, with the additional advantage of having the capability of polarizing other nuclear species. Nevertheless the gas extraction procedure has still to be optimized in order to reduce polarization losses. We strongly believe that getting rid of the cryo-collection step would solve the problem. A cryogen-free extraction setup is already under investigation. The basic idea would be to quickly dissolve the sample and let it expanding in a vacuum-pumped line eliminating (or at least minimizing as much as possible) the pressurized helium, used for pushing the HP sample out from the cryostat, and replacing the cold-trap at the end of the line with a glass spherical container inside which the HP xenon gas would be collected.

Appendix A

Chapter 4 supplementary material

A.1 Solid state ^{13}C NMR spectral line width

In this section, we present a theoretical calculation of the heteronuclear dipolar broadening contribution to the solid state carbon NMR spectral line width due to the coupling between acetate ^{13}C nuclei and ^1H (^2H) nuclei for different solvent compositions. Following what has been already described in Section 3.2.6, the simplest way to evaluate the contribution of the dipolar local field to the ^{13}C spectrum line width is to consider the square root of the homogeneous second moment. For unlike-spins, assuming a random distribution accross the sample, the "carbon-proton" second moment writes, according to equations (3.23) and (3.24):

$$M_{2,^{13}\text{C}-^1\text{H}} \simeq 7 \left(\frac{\mu_0}{4\pi} \right)^2 \hbar^2 (\gamma_{^{13}\text{C}})^2 (\gamma_{^1\text{H}})^2 (N_{^1\text{H}})^2 = 6.67 \times 10^{-51} (N_{^1\text{H}})^2 \quad (\text{A.1})$$

and the "carbon-deuterium" second moment:

$$M_{2,^{13}\text{C}-^2\text{H}} \simeq 19 \left(\frac{\mu_0}{4\pi} \right)^2 \hbar^2 (\gamma_{^{13}\text{C}})^2 (\gamma_{^2\text{H}})^2 (N_{^2\text{H}})^2 = 4.10 \times 10^{-52} (N_{^2\text{H}})^2 \quad (\text{A.2})$$

The contribution of equations (A.1) and (A.2) to the ^{13}C NMR line width is respectively

$$\sqrt{M_{2,^{13}\text{C}-^1\text{H}}} = 8.10 \times 10^{-20} N_{1\text{H}} \text{ Hz} \cdot \text{cm}^3 \quad (\text{A.3})$$

and

$$\sqrt{M_{2,^{13}\text{C}-^2\text{H}}} = 2.00 \times 10^{-20} N_{2\text{H}} \text{ Hz} \cdot \text{cm}^3 \quad (\text{A.4})$$

with $N_{1\text{H}}$ and $N_{2\text{H}}$ expressed in spins/cm³. Since the solvent solutions of the FP and FD samples considered in Chapter 4 have a ^1H and ^2H nuclear spin concentration of 6.64×10^{22} spins/cm³, the contribution to the line broadening becomes 5.38 kHz for the fully-protonated solvent and 1.33 kHz for the fully-deuterated solvent. On the other hand, the contribution for the HH sample is $\sqrt{\left(\frac{M_{2,^{13}\text{C}-^1\text{H}}}{2}\right) + \left(\frac{M_{2,^{13}\text{C}-^2\text{H}}}{2}\right)} = 3.92$ kHz. In magnetic field units the dipolar broadenings of the three samples FD, HH and FP are 0.12, 0.36 and 0.50 mT, respectively.

A.2 Microwave power calibration

The microwave power calibration was performed at 1.5 K on the three systems. The aim was to find the minimum power giving the best DNP enhancement in order to avoid undesired heating of the sample. In Figure A.1 to Figure A.3 the ^{13}C DNP enhancement is reported as function of the nominal output power. As a consequence, the working nominal power was set to 100 mW at 3.4 T and 55 mW at the other two fields. These values correspond to a microwave B_1 field of about 10^{-2} mT. Even though it is well known that at lower frequency, limiting microwave power loss is easier, the microwave source-to-waveguide coupling system was less efficient at 3.4 T with respect to 5 T and 7 T. This is the reason why at the lower field the required nominal output power is higher.

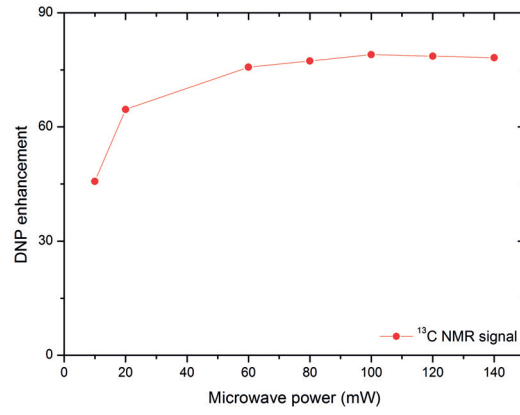


Figure A.1: Microwave power calibration at 3.4 T and 1.5 K performed on the HH sample. The DNP enhancement is reported as a function of the nominal output power.

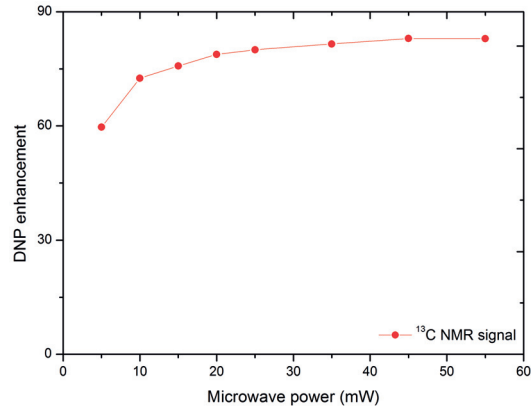


Figure A.2: Microwave power calibration at 5 T and 1.5 K performed on the HH sample. The DNP enhancement is reported as a function of the nominal output power.

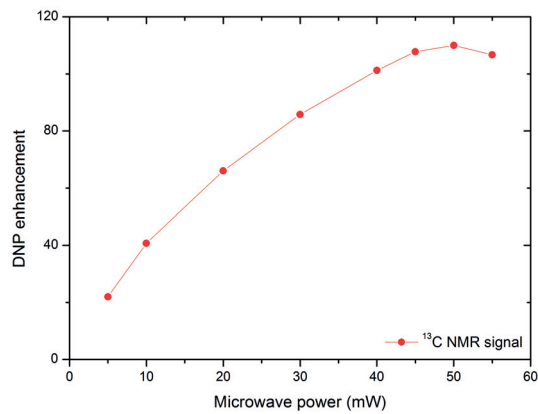


Figure A.3: Microwave power calibration at 7 T and 1.5 K performed on the HH sample. The DNP enhancement is reported as a function of the nominal output power.

Appendix B

Chapter 5 supplementary material

B.1 X-band ESR spectrometer calibration curve

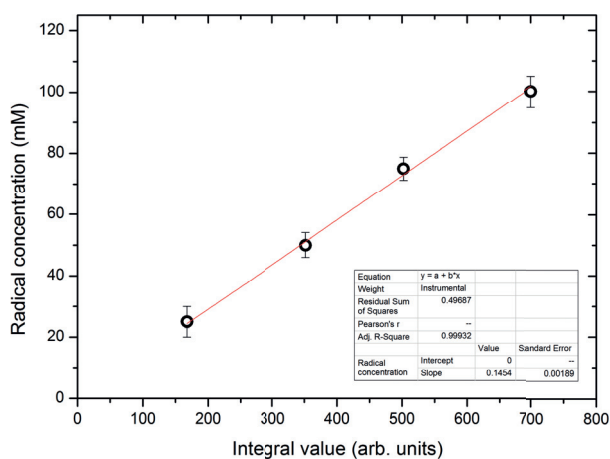


Figure B.1: X-band ESR spectrometer calibration curve. The data (black circles) were measured in reference samples containing known TEMPO concentrations. The integral values of the ESR integrated spectra are reported as a function of the radical concentration. The linear fit (red line; slope: 0.145 ± 0.002) was used to estimate the radical concentration of all UV-irradiated samples.

B.2 5 T ^{129}Xe and 7 T ^6Li (^{13}C) microwave spectra

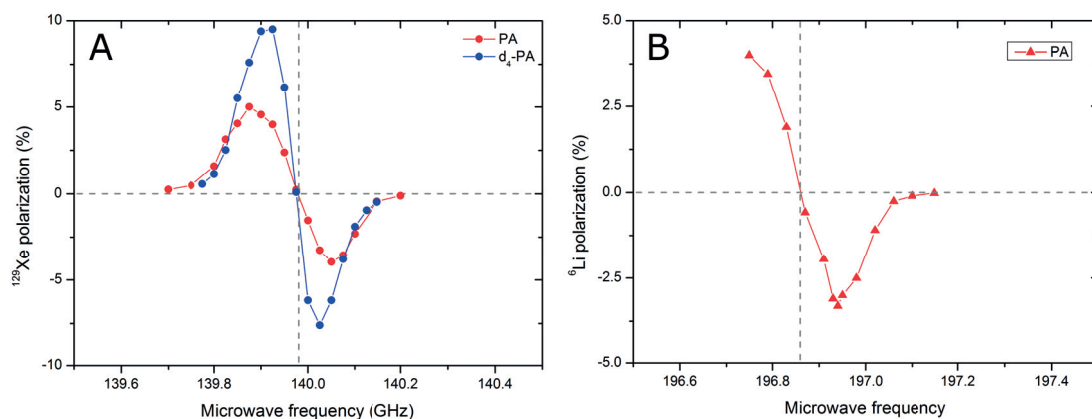


Figure B.2: (A) ^{129}Xe DNP microwave spectra measured at 5 T and 1.5 K on samples containing 5 M xenon dissolved in 2-methyl-1-pentanol:PA 10:1 (v/v) (red dots) and 5 M xenon dissolved in 2-methyl-1-pentanol:PA 10:1 (v/v) (blue dots). (B) ^6Li DNP microwave spectrum measured at 7 T and 1.5 K on 3 M $^6\text{LiCl}$ sample prepared in $\text{H}_2\text{O}:\text{EtOH}$ 1:1 (v/v) with 30 % UV-irradiated PA. Values reported on the vertical axis are rescaled as a function of the maximum liquid state polarization, measured in the 9.4 T MR scanner after dissolution, irradiating the sample at 196.750 GHz. The ^{13}C DNP microwave spectrum measured at 7 T and 1.5 K on $[1\text{-}^{13}\text{C}]\text{PA}:\text{H}_2\text{O}$ 1:1 (v/v) used for the radical free HP solid experiment in Section 5.3 is basically identical.

Appendix C

EasySpin ESR spectra fitting and calculation

Values of the A-tensor (Sys.A) are in MHz; values of the D-tensor and E-tensor (first and second component of Sys.D respectively) are in MHz; the phenomenological dipolar broadening is expressed in mT and represents the FWHM of the Gaussian line convoluted with each resonance of the powder spectrum. See [128] for details.

C.1 X-band TEMPO radical fit

```
% Spin system
[B,spc] = textread('deriv_tempo.txt','%f %f');
Sys.S = 1/2;
Sys.g = [2.0094 2.0065 2.0017];
Sys.Nucs = '14N';
Sys.A = [20.48 17.68 10.1];
Sys.lw = [1.4];
```

```

Exp.mwFreq = 9.520;
Exp.CenterSweep = [338, 30];
Exp.nPoints = 2048;
% Simulation
[xa, ya] = pepper(Sys, Exp);
plot(xa, ya);
hold all spc1 = rescale(spc, ya, 'maxabs');
plot(B, spc1);
xlabel('magnetic field [mT]');
ylabel('normalized intensity');
axis tight;
legend('fit', 'experiment');
title('TEMPO radical');
% fitting
Vary.g = [0.0001 0.0001 0.0001];
Vary.A = [0.1, 0.1, 0.1];
Vary.lw = [0.1];
esfit('pepper', spc1, Sys, Vary, Exp)
spettro = [xa', ya'];
save spettro_tempo_Xband.dat spettro -ascii

```

C.2 X-band UV-irradiated PA fit

```

% Spin system
[B, spc] = textread('deriv_UV_PA.txt', '%f %f');
Sys.S = 1/2;

```

```

Sys.g = [2.0041 2.0037 2.0042];
Sys.Nucs = '1H,1H,1H';
Sys.A = [48];
Sys.lw = [1.02];
Exp.mwFreq = 9.448;
Exp.CenterSweep = [338, 30];
Exp.nPoints = 2048;
% Simulation
[xa,ya] = pepper(Sys,Exp);
plot(xa,ya);
hold all spc1 = rescale(spc,ya,'maxabs');
plot(B,spc1);
xlabel('magnetic field [mT]');
ylabel('normalized intensity');
axis tight;
legend('fit','experiment');
title('UV-irradiated PA radical');
% fitting
Vary.g = [0.0001 0.0001 0.0001];
Vary.A = [0.1, 0.1, 0.1];
Vary.lw = [0.1];
esfit('pepper',spc1,Sys,Vary,Exp)
spettro = [xa', ya'];
save spettro_UV_PA_Xband.dat spettro -ascii

```

C.3 X-band UV-irradiated 1-13C-PA fit

```

% Spin system
[B,spc] = textread('deriv_UV_1-13C-PA.txt','%f %f');
Sys.S = 1/2;
Sys.g = [2.0041 2.0037 2.0042];
Sys.Nucs = '1H,1H,1H,13C';
Sys.A = [48; 48; 48; 30];
Sys.lw = [1.02];
Exp.mwFreq = 9.442;
Exp.CenterSweep = [338, 30];
Exp.nPoints = 2048;
% Simulation
[xa,ya] = pepper(Sys,Exp);
plot(xa,ya);
hold all spc1 = rescale(spc,ya,'maxabs');
plot(B,spc1);
xlabel('magnetic field [mT]');
ylabel('normalized intensity');
axis tight;
legend('fit','experiment');
title('UV-irradiated 1-13C-PA radical');
% fitting
Vary.g = [0.0001 0.0001 0.0001];
Vary.A = [0.1, 0.1, 0.1];
Vary.lw = [0.1];

```

```

esfit('pepper', spc1, Sys, Vary, Exp)
spettro = [xa', ya'];
save spettro_UV_1-13C-PA_Xband.dat spettro -ascii

```

C.4 X-band UV-irradiated 2-13C-PA fit

```

% Spin system
[B, spc] = textread('deriv_UV_2-13C-PA.txt', '%f %f');
Sys.S = 1/2;
Sys.g = [2.0041 2.0037 2.0042];
Sys.Nucs = '1H,1H,1H,13C';
Sys.A = [40 48 ;40 48;40 48;49 144];
Sys.lw = [1.02];
Exp.mwFreq = 9.490;
Exp.CenterSweep = [338, 30];
Exp.nPoints = 2048;
% Simulation
[xa, ya] = pepper(Sys, Exp);
plot(xa, ya);
hold all spc1 = rescale(spc, ya, 'maxabs');
plot(B, spc1);
xlabel('magnetic field [mT]');
ylabel('normalized intensity');
axis tight;
legend('fit', 'experiment');
title('UV-irradiated 2-13C-PA radical');

```

```

% fitting
Vary.g = [0.0001 0.0001 0.0001];
Vary.A = [0.1, 0.1, 0.1];
Vary.lw = [0.1];
esfit('pepper', spc1, Sys, Vary, Exp)
spettro = [xa', ya'];
save spettro_UV_2-13C-PA_Xband.dat spettro -ascii

```

C.5 X-band UV irradiated d4-PA ($S = 1/2$) fit

```

% Spin system
[B, spc] = textread('deriv_d4-UV_PA.txt', '%f %f');
Sys.S = 1/2;
Sys.g = [2.0041 2.0037 2.0042];
Sys.Nucs = '1H,1H,1H';
Sys.A = [7.3];
Sys.lw = [1.02];
Exp.mwFreq = 9.554;
Exp.CenterSweep = [338, 30];
Exp.nPoints = 2048;
% Simulation
[xa, ya] = pepper(Sys, Exp);
plot(xa, ya);
hold all spc1 = rescale(spc, ya, 'maxabs');
plot(B, spc1);
xlabel('magnetic field [mT]');

```

```

ylabel('normalized intensity');
axis tight;
legend('fit','experiment');
title('UV-irradiated d4-PA radical');
% fitting
Vary.g = [0.0001 0.0001 0.0001];
Vary.A = [0.1, 0.1, 0.1];
Vary.lw = [0.1];
esfit('pepper',spc1, Sys, Vary, Exp)
spettro = [xa', ya'];
save spettro_UV_d4-PA_Xband.dat spettro -ascii

```

C.6 X-band UV-irradiated d4-PA ($S = 1$) fit

```

% Spin system
[B, spc] = textread('deriv_d4-UV_PA.txt', '%f %f');
Sys.S = 1/2;
Sys.g = [2.0041 2.0037 2.0042];
Sys.Nucs = '1H,1H,1H';
Sys.A = [7.1];
Sys.D = [2.7 4.3];
Sys.lw = [1.02];
Exp.mwFreq = 9.554;
Exp.CenterSweep = [338, 30];
Exp.nPoints = 2048;
% Simulation

```

```

[xa, ya] = pepper(Sys, Exp);
plot(xa, ya);
hold all spc1 = rescale(spc, ya, 'maxabs');
plot(B, spc1);
xlabel('magnetic field [mT]');
ylabel('normalized intensity');
axis tight;
legend('fit', 'experiment');
title('UV-irradiated d4-PA radical');
% fitting
Vary.g = [0.0001 0.0001 0.0001];
Vary.A = [0.1, 0.1, 0.1];
Vary.D = [0.1, 0.1];
Vary.lw = [0.1];
esfit('pepper', spc1, Sys, Vary, Exp)
spettro = [xa', ya'];
save spettro_UV_d4-PA_S_1_Xband.dat spettro -ascii

```

C.7 TEMPO radical calculated spectrum at 3.4 T

```

%This script calculates the integrated 3.4 T
%ESR spectrum of the TEMPO radical
%embedded in a glassy matrix

%Spin System
Sys.S = 1/2;

```



```

Sys.g = [2.0094 2.0065 2.0017];
Sys.Nucs = '14N';
Sys.A = [20.48 17.68 101];
Sys.lw = [1.4];
%Experimental Parameters
Field = 3380;
Exp.mwFreq = 94.8;
Exp.CenterSweep = [Field , 50];
Exp.Harmonic = 0;
Exp.nPoints = 2048;
%Simulation
[xma,ya] = pepper(Sys,Exp);
a = xma/1000*13.9962*2.0023;
xGHz = wrev(a);
plot(xGHz,ya);
xlabel('MW Frequency [GHz] ');
ylabel('Normalized Intensity ');
title('TEMPO radical 3e4 T ');
axis tight;
spettro = [xGHz', ya'];
save spettro3e4T.dat spettro -ascii;

```

C.8 TEMPO radical calculated spectrum at 5 T

```

%This script calculates the integrated 5 T
%ESR spectrum of the TEMPO radical

```

```

%embedded in a glassy matrix

%Spin System
Sys.S = 1/2;
Sys.g = [2.0094 2.0065 2.0017];
Sys.Nucs = '14N';
Sys.A = [20.48 17.68 101];
Sys.lw = [1.4];
%Experimental Parameters
Field = 4991;
Exp.mwFreq = 140;
Exp.CenterSweep = [Field , 50];
Exp.Harmonic = 0;
Exp.nPoints = 2048;
%Simulation
[xma,ya] = pepper(Sys,Exp);
a = xma/1000*13.9962*2.0023;
xGHz = wrev(a);
plot(xGHz,ya);
xlabel('MW Frequency [GHz] ');
ylabel('Normalized Intensity ');
title('TEMPO radical 5 T ');
axis tight;
spettro = [xGHz', ya'];
save spettro_TEMPO_5T.dat spettro -ascii;

```

C.9 UV-PA radical calculated spectrum at 5 T

```
%This script calculates the integrated 5 T
%ESR spectrum of the UV-irradiated PA radical
%embedded in a glassy matrix
```

```
%Spin System
```

```
Sys.S = 1/2;
```

```
Sys.g = [2.0041 2.0037 2.0042];
```

```
Sys.Nucs = '1H,1H,1H';
```

```
Sys.A = [48];
```

```
Sys.lw = [1.02];
```

```
%Experimental Parameters
```

```
Field = 4991;
```

```
Exp.mwFreq = 140;
```

```
Exp.CenterSweep = [Field , 50];
```

```
Exp.Harmonic = 0;
```

```
Exp.nPoints = 2048;
```

```
%Simulation
```

```
[xma,ya] = pepper(Sys,Exp);
```

```
a = xma/1000*13.9962*2.0023;
```

```
xGHz = wrev(a);
```

```
plot(xGHz,ya);
```

```
xlabel('MW Frequency [GHz]');
```

```
ylabel('Normalized Intensity');
```

```
title('UV-PA 5 T');
```

```

axis tight;
spettro = [xGHz', ya'];
save spettro_UV_PA_5T.dat spettro -ascii;

```

C.10 UV-d4-PA radical calculated spectrum at 5 T

```

%This script calculates the integrated 5 T
%ESR spectrum of the UV-irradiated d4-PA radical
%embedded in a glassy matrix

```

```

%Spin System
Sys.S = 1/2;
Sys.g = [2.0041 2.0037 2.0042];
Sys.Nucs = '1H,1H,1H';
Sys.A = [7.3];
Sys.lw = [1.02];
%Experimental Parameters
Field = 4991;
Exp.mwFreq = 140;
Exp.CenterSweep = [Field, 50];
Exp.Harmonic = 0;
Exp.nPoints = 2048;
%Simulation
[xma, ya] = pepper(Sys, Exp);
a = xma/1000*13.9962*2.0023;
xGHz = wrev(a);

```

```

plot(xGHz, ya);
xlabel('MW Frequency [GHz] ');
ylabel('Normalized Intensity ');
title('UV-d4-PA 5 T ');
axis tight;
spettro = [xGHz', ya'];
save spettro_UV_d4PA_5T.dat spettro -ascii;

```

C.11 TEMPO radical calculated spectrum at 7 T

```

%This script calculates the integrated 7 T
%ESR spectrum of the TEMPO radical
%embedded in a glassy matrix

```

```

%Spin System
Sys.S = 1/2;
Sys.g = [2.0094 2.0065 2.0017];
Sys.Nucs = '14N';
Sys.A = [20.48 17.68 101];
Sys.lw = [1.4];
%Experimental Parameters
Field = 7020;
Exp.mwFreq = 197;
Exp.CenterSweep = [Field, 50];
Exp.Harmonic = 0;
Exp.nPoints = 2048;

```

```

%Simulation

[xma,ya] = pepper(Sys,Exp);
a = xma/1000*13.9962*2.0023;
xGHz = wrev(a);
plot(xGHz,ya);
xlabel('MW Frequency [GHz] ');
ylabel('Normalized Intensity ');
title('TEMPO radical 7 T ');
axis tight;
spettro = [xGHz', ya'];
save spettro_TEMPO_7T.dat spettro -ascii;

```

Appendix D

Chapter 6 supplementary material

D.1 Polarization build-up time constant

For all samples, the ^{129}Xe polarization time constant was obtained by fitting the NMR signal time evolution under microwave irradiation to the expression $P(t) = P_0 + P_\infty [1 - \exp(-t/T_{pol})]$ where $P(t)$, P_0 , P_∞ and T_{pol} represent respectively the polarization as a function of time, the polarization thermal equilibrium value, the polarization steady-state value under microwave irradiation and the polarization time constant. All numerical results are reported in Table D.1, Table D.2 and Table D.3.

For samples containing a xenon concentration equal or below the ST, the polarization time constant increases with decreasing xenon concentration. A similar behaviour has previously been reported for DNP-enhanced ^{13}C samples and it is attributed to the dependence of spin diffusion on nuclear spin concentration [40, 96]. Note that the accuracy of the mono-exponential fit decreases for samples containing a xenon concentration exceeding the solvent ST, and the dependence of the polarization time constant on xenon concentration exhibit an ill-defined trend for those samples (see Figure D.1).

Xe concentration [M]	Polarization time constant [s]	R^2
2.8	1950 ± 51	0.99910
5	1541 ± 49	0.99902
6.8	1357 ± 45	0.99895
8.2	956 ± 39	0.99863
9.4	789 ± 20	0.99839

Table D.1: DNP polarization time constant and R^2 value obtained from the mono-exponential fit of the ^{129}Xe polarization evolution measured at 5 T and 1.50 ± 0.05 K under microwave irradiation at 140.3 GHz with 55 mW output power in samples prepared with 2-methyl-1-pentanol containing 50 mM TEMPO and different xenon concentrations. The data for the sample containing a xenon concentration corresponding to the solubility threshold (ST) of 2-methyl-1-pentanol is presented in red font.

Xe concentration [M]	Polarization time constant [s]	R^2
2.8	1756 ± 56	0.99806
5	1160 ± 34	0.99831
6.8	900 ± 40	0.99670
8.2	938 ± 63	0.99390
9.4	1147 ± 77	0.99255

Table D.2: DNP polarization time constant and R^2 value obtained from the mono-exponential fit of the ^{129}Xe polarization evolution measured at 5 T and 1.50 ± 0.05 K under microwave irradiation at 140.3 GHz with 55 mW output power in samples prepared with 2-methyl-1-propanol containing 50 mM TEMPO and different xenon concentrations. The data for the sample containing a xenon concentration corresponding to the solubility threshold (ST) of 2-methyl-1-propanol is presented in red font.

Xe concentration [M]	Polarization time constant [s]	R^2
1.5	1297 ± 32	0.99917
2.8	1237 ± 74	0.99669
5	1743 ± 82	0.99780
6.8	1295 ± 48	0.99610
8.2	627 ± 16	0.99549

Table D.3: DNP polarization time constant and R^2 value obtained from the mono-exponential fit of the ^{129}Xe polarization evolution measured at 5 T and 1.50 ± 0.05 K under microwave irradiation at 140.3 GHz with 55 mW output power in samples prepared with ethanol containing 50 mM TEMPO and different xenon concentrations. The data for the sample containing a xenon concentration corresponding to the solubility threshold (ST) of ethanol is presented in red font.

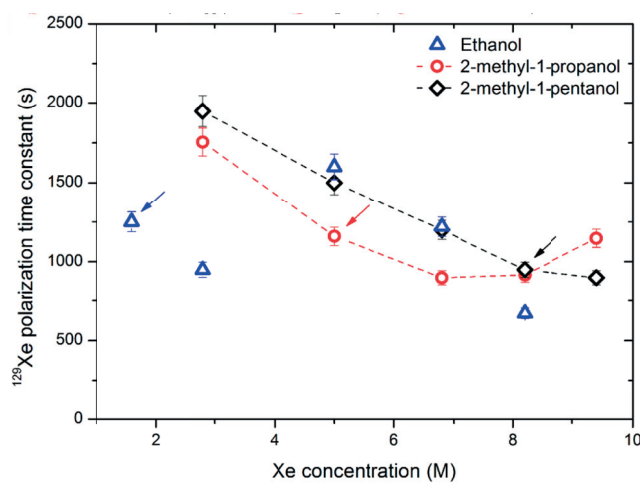


Figure D.1: ^{129}Xe polarization polarization time constant as a function of xenon concentration. Measurements were performed at 5 T and 1.50 ± 0.05 K under microwave irradiation at 140.3 GHz with an output power of 55 mW. Dashed lines connecting the data points are drawn as guide for the eyes; small arrows indicate the xenon concentration corresponding to the ST of each solvent.

D.2 Supplementary xenon solid state spectra

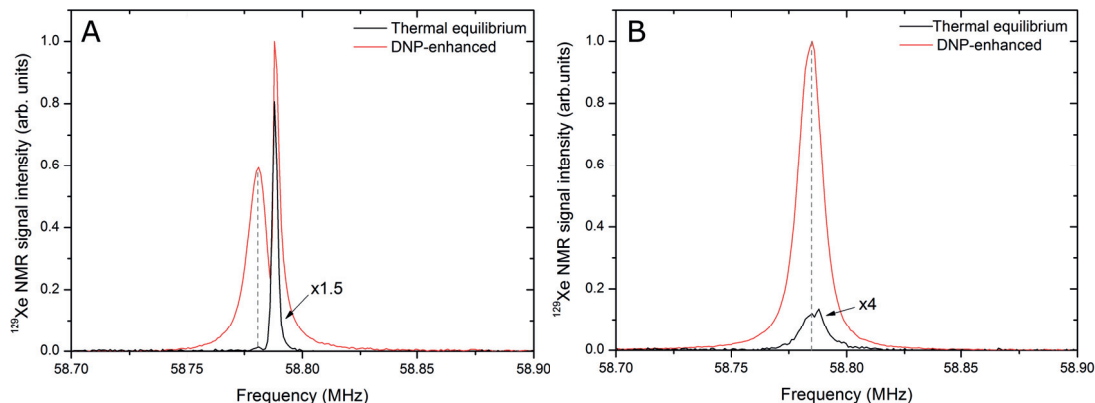


Figure D.2: (A) solid state ^{129}Xe NMR signal measured at 5 T and 1.50 ± 0.05 K with a 20° rf pulse in a 8.2 M natural-abundance xenon sample dissolved in ethanol containing 50 mM TEMPO at thermal equilibrium (black curve), and after 90 min of microwave irradiation at 140.3 GHz with 55 mW output power (red curve). The frequency shift between the sharp up-field peak (58.788 MHz) and the broad down-field peak (58.781 MHz) is identical for both spectra (7 kHz corresponding to 119 ppm). Note that the sharp peak is less enhanced than in the sample prepared with 2-methyl-propanol (Figure 2), which is most likely due to the larger frequency shift difference (119 vs. 85 ppm). (B) solid state ^{129}Xe NMR signal measured at 5 T and 1.50 ± 0.05 K with a 20° rf pulse in a 9.4 M natural-abundance xenon sample dissolved in 2-methyl-1-pentanol containing 50 mM TEMPO at thermal equilibrium (black curve), and after 90 min of microwave irradiation at 140.3 GHz with 55 mW output power (red curve). The frequency shift (3 kHz corresponding to 51 ppm) between the sharp up-field peak (58.788 MHz) and the broad down-field peak (58.785 MHz) is slightly visible in the thermal equilibrium spectrum.

D.3 Solid state xenon NMR spectral line width

In this section, an in-depth analysis of the line width of the solid state ^{129}Xe NMR spectra measured in samples containing a xenon concentration equal to the ST of each one of the three solvents is presented. Following what has been already described in Section 3.2.6 for the nuclear case, the simplest way to evaluate the contribution of the dipolar local field to the ^{129}Xe spectrum line width is to consider the square root of the homogeneous second moment. In each sample we have two contributions, one coming from like-spins (the dipolar coupling between ^{129}Xe nuclei themselves), and

one coming from unlike-spins (the coupling between ^{129}Xe nuclei and the solvent ^1H nuclei). Assuming a random distribution of the spins across the sample, according to equations (3.23) and (3.24) the "xenon-xenon" second moment writes:

$$M_{2,^{129}\text{Xe}-^{129}\text{Xe}} \simeq 16 \left(\frac{\mu_0}{4\pi} \right)^2 \hbar^2 (\gamma_{^{129}\text{Xe}})^4 (N_{^{129}\text{Xe}})^2 = 1.35 \times 10^{-51} (N_{^{129}\text{Xe}})^2 \quad (\text{D.1})$$

and the "xenon-proton":

$$M_{2,^{129}\text{Xe}-^1\text{H}} \simeq 7 \left(\frac{\mu_0}{4\pi} \right)^2 \hbar^2 (\gamma_{^{129}\text{Xe}})^2 (\gamma_{^1\text{H}})^2 (N_{^1\text{H}})^2 = 7.94 \times 10^{-51} (N_{^1\text{H}})^2 \quad (\text{D.2})$$

The contribution of equations (D.1) and (D.2) to the line width writes respectively

$$\sqrt{M_{2,^{129}\text{Xe}-^{129}\text{Xe}}} = 3.67 \times 10^{-20} N_{^{129}\text{Xe}} \text{ Hz} \cdot \text{cm}^3 \quad (\text{D.3})$$

and

$$\sqrt{M_{2,^{129}\text{Xe}-^1\text{H}}} = 8.91 \times 10^{-20} N_{^1\text{H}} \text{ Hz} \cdot \text{cm}^3 \quad (\text{D.4})$$

with $N_{^{129}\text{Xe}}$ and $N_{^1\text{H}}$ expressed in spins/cm³. The ^{129}Xe NMR line broadening contribution given by equations (D.3) and (D.4) (like- and unlike-spins respectively) for the three samples reported in Figure 6.4A is compared with the measured *FWHM* of the spectrum. Results are reported in Table D.4. It is clear that the contribution to the line width coming from like-spins coupling is negligible (confirmed experimentally by the sharp peak characterizing inhomogeneous ^{129}Xe spectra), so the main source of broadening comes from the $^{129}\text{Xe} - ^1\text{H}$ dipolar coupling. Even though there is no perfect numerical match between calculated and measured values, the important feature is, in both cases, the scaling behavior of the line broadening with increasing ^1H nuclei concentration in the solvent. The measured *FWHM* of the three different samples was thus plotted as a function of the solvent $N_{^1\text{H}}$ (see Figure D.3). In good agreement with

equation (D.4), the correlation was found to be linear ($R^2 = 0.981$).

Sample	1.5 M Xe ethanol	5 M Xe 1-propanol	8.2 M 1-pentanol
$N_{^{129}\text{Xe}}$ [spins/cm ³]	0.23×10^{21}	0.79×10^{21}	1.30×10^{21}
$N_{^1\text{H}}$ [spins/cm ³]	6.18×10^{22}	6.51×10^{22}	6.82×10^{22}
Broadening $_{^{129}\text{Xe}-^{129}\text{Xe}}$ [kHz]	0.01	0.03	0.05
Broadening $_{^{129}\text{Xe}-^1\text{H}}$ [kHz]	5.51	5.80	6.07
Measured $FWHM$ [kHz]	10.24 ± 0.40	12.37 ± 0.35	13.84 ± 0.47

Table D.4: Comparison between calculated and measured FWHM for the three samples reported in Figure 6.4A; the ^{129}Xe density was determined experimentally during samples preparation and the ^1H density was taken from the literature [92].

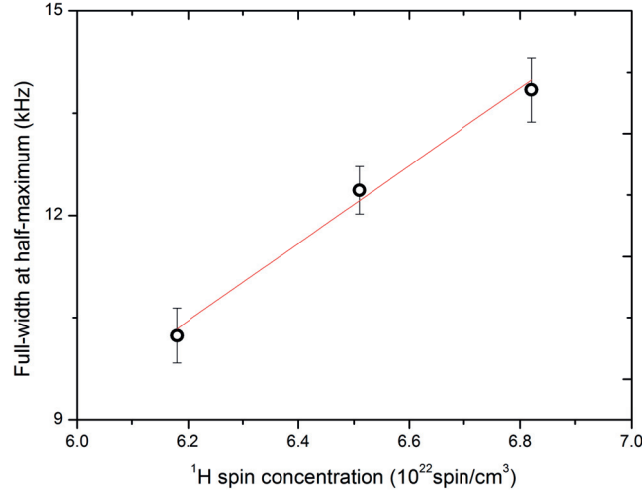


Figure D.3: Measured $FWHM$ for the three samples shown in Figure 6.4A as a function of the ^1H spins density of the solvent. A linear function was used for fitting the experimental data (red line).

Bibliography

- [1] A. Abragam. *The principles of nuclear magnetism*. University Press, Oxford, 1961.
- [2] A. Abragam. Overhauser effect in nonmetals. *Physical Review*, 98(6):1729, 1955.
- [3] A. Abragam and M. Goldman. *Order and disorder*. Clarendon Press, Oxford, 1982.
- [4] A. Abragam and M. Goldman. Principles of dynamic nuclear-polarization. *Reports on Progress in Physics*, 41(3):395–467, 1978.
- [5] A. Abragam, P. A. Leermakers, and G. F. Vesley. Photolysis of pyruvic acid in solution. *Journal of Organic Chemistry*, 28(4):1160–&, 1963.
- [6] A. Abragam and W. G. Proctor. Spin temperature. *Physical Review*, 109(5):1441, 1958.
- [7] R. W. Adams, J. A. Aguilar, K. D. Atkinson, M. J. Cowley, P. I. Elliott, S. B. Duckett, G. R. Green, I. G. Khazal, J. López-Serrano, and D. C. Williamson. Reversible interactions with para-hydrogen enhance NMR sensitivity by polarization transfer. *Science*, 323(5922):1708–1711, 2009.
- [8] J. H. Ardenkjaer-Larsen, B. Fridlund, A. Gram, G. Hansson, L. Hansson, M. H. Lerche, R. Servin, M. Thaning, and K. Golman. Increase in signal-to-noise ratio

- of $> 10,000$ times in liquid-state NMR. *Proceedings of the National Academy of Sciences of the United States of America*, 100(18):10158–10163, 2003.
- [9] J.-H. Ardenkjaer-Larsen, A. M. Leach, N. Clarke, J. Urbahn, D. Anderson, and T. W. Skloss. Dynamic nuclear polarization polarizer for sterile use intent. *NMR in biomedicine*, 24(8):927–932, 2011.
- [10] J.-H. Ardenkjaer-Larsen, S. Macholl, and H. Johannesson. Dynamic nuclear polarization with trityls at 1.2 K. *Applied Magnetic Resonance*, 34(3-4):509–522, 2008.
- [11] V. A. Atsarkin. Experimental investigation of manifestations of spin-spin interaction reservoir in a system of EPR lines connected with cross relaxation. *Soviet Physics JETP-USSR*, 32(3):421–425, 1971.
- [12] V. A. Atsarkin. Verification of the spin-spin temperature concept in experiments on saturation of EPR. *Soviet Phys.-JETP*, 31(6):1012–1018, 1970.
- [13] V. A. Atsarkin and M. I. Rodak. Temperature of spin-spin interactions in EPR. *Uspekhi Fizicheskikh Nauk*, 107(1):3–17, 1972.
- [14] R. Balzan. *Methods for Molecular Magnetic Resonance Imaging and Magnetic Resonance Spectroscopy using Hyperpolarized Nuclei*. PhD thesis, EPFL, 2013.
- [15] K. Bartik, P. Choquet, A. Constantinesco, G. Duhamel, J. Fraissard, J.-N. Hyacinthe, J. Jokisaari, E. Locci, T. J. Lowery, M. Luhmer, et al. Xenon NMR as a probe for microporous and mesoporous solids, polymers, liquid crystals, solutions, flames, proteins, imaging. *L'Actualite chimique*, (287):16–34, 2005.
- [16] P. Berthault, G. Huber, and H. Desvaux. Biosensing using laser-polarized xenon

- NMR/MRI. *Progress in Nuclear Magnetic Resonance Spectroscopy*, 55(1):35–60, 2009.
- [17] N. D. Bhaskar, J. Camparo, W. Happer, and A. Sharma. Light narrowing of magnetic resonance lines in dense, optically pumped alkali-metal vapor. *Physical Review A*, 23(6):3048, 1981.
 - [18] N. Bloembergen. On the interaction of nuclear spins in a crystalline lattice. *Physica*, 15(3):386–426, 1949.
 - [19] N. Bloembergen, E. M. Purcell, and R. V. Pound. Relaxation effects in nuclear magnetic resonance absorption. *Physical Review*, 73(7):679, 1948.
 - [20] N. Bloembergen, S. Shapiro, P. S. Pershan, and J. O. Artman. Cross-relaxation in spin systems. *Physical Review*, 114(2):445, 1959.
 - [21] W. de Boer, M. Borghini, K. Morimoto, T. O. Niinikoski, and F. Udo. Dynamic polarization of protons, deuterons, and carbon-13 nuclei: Thermal contact between nuclear spins and an electron spin-spin interaction reservoir. *Journal of Low Temperature Physics*, 15(3-4):249–267, 1974.
 - [22] M. Borghini. Mechanism of nuclear dynamic polarization by electron-nucleus dipolar coupling in solids. Technical report, European Organization for Nuclear Research, Geneva (Switzerland), 1971.
 - [23] M. Borghini. Spin-temperature model of nuclear dynamic polarization using free radicals. *Physical Review Letters*, 20(9):419–&, 1968.
 - [24] M. Borghini and F. Udo. Dynamic polarization of ^{13}C nuclei in 1-Butanol. *Physics Letters A*, 43(2):93–94, 1973.

- [25] A. Bornet, R. Melzi, A. J. P. Linde, P. Hautle, B. van den Brandt, S. Jannin, and G. Bodenhausen. Boosting dissolution dynamic nuclear polarization by cross polarization. *Journal of Physical Chemistry Letters*, 4(1):111–114, 2013.
- [26] L.-S. Bouchard, S. R. Burt, M. S. Anwar, K. V. Kovtunov, I. V. Koptug, and A. Pines. NMR imaging of catalytic hydrogenation in microreactors with the use of para-hydrogen. *Science*, 319(5862):442–445, 2008.
- [27] S. Bowen and C. Hilty. Rapid sample injection for hyperpolarized NMR spectroscopy. *Physical Chemistry Chemical Physics*, 12(22):5766–5770, 2010.
- [28] S. Bowen and C. Hilty. Time-resolved dynamic nuclear polarization enhanced NMR spectroscopy. *Angewandte Chemie*, 120(28):5313–5315, 2008.
- [29] C. R. Bowers and D. P. Weitekamp. Parahydrogen and synthesis allow dramatically enhanced nuclear alignment. *Journal of the American Chemical Society*, 109(18):5541–5542, 1987.
- [30] C. R. Bowers and D. P. Weitekamp. Transformation of symmetrization order to nuclear-spin magnetization by chemical reaction and nuclear magnetic resonance. *Physical Review Letters*, 57(21):2645, 1986.
- [31] E. Boyes, B. Craven, R. Gamet, P. J. Hayman, et al. Measurements of the effect of absorbed power on the polarization attainable in a butanol target. Technical report, Liverpool Univ.(England), 1971.
- [32] D. Budac and P. Wan. Photodecarboxylation - mechanism and synthetic utility. *Journal of Photochemistry and Photobiology a-Chemistry*, 67(2):135–166, 1992.
- [33] T. R. Carver and C. P. Slichter. Polarization of nuclear spins in metals. *Physical Review*, 92(1):212, 1953.

- [34] T. Cheng, A. Capozzi, Y. Takado, R. Balzan, and A. Comment. Over 35% liquid-state ^{13}C polarization obtained via dissolution dynamic nuclear polarization at 7 T and 1 K using ubiquitous nitroxyl radicals. *Physical Chemistry Chemical Physics*, 15(48):20819–20822, 2013.
- [35] T. Cheng, M. Mishkovsky, J. A. M. Bastiaansen, O. Ouari, P. Hautle, P. Tordo, B. van den Brandt, and A. Comment. Automated transfer and injection of hyperpolarized molecules with polarization measurement prior to in vivo NMR. *NMR in Biomedicine*, 26(11):1582–1588, 2013.
- [36] A. Cherubini and A. Bifone. Hyperpolarized xenon in biology. *Progress in Nuclear Magnetic Resonance Spectroscopy*, 42(1-2):1–30, 2003.
- [37] Z. I. Cleveland, G. P. Cofer, G. Metz, D. Beaver, J. Nouns, S. S. Kaushik, M. Kraft, J. Wolber, K. T. Kelly, H. P. McAdams, and B. Driehuys. Hyperpolarized ^{129}Xe MR imaging of alveolar gas uptake in humans. *PLoS One*, 5(8):e12192 1–8, 2010.
- [38] S. Clough and J. R. Hill. Temperature dependence of methyl group tunnelling rotation frequency. *Journal of Physics C: Solid State Physics*, 7(1):L20, 1974.
- [39] A. Comment, B. van den Brandt, K. Uffmann, F. Kurdzesau, S. Jannin, J. A. Konter, P. Hautle, W. T. Wenckebach, R. Gruetter, and J. J. van der Klink. Principles of operation of a DNP prepolarizer coupled to a rodent MRI scanner. *Applied Magnetic Resonance*, 34(3-4):313–319, 2008.
- [40] A. Comment, B. van den Brandt, K. Uffmann, F. Kurdzesau, S. Jannin, J. A. Konter, P. Hautle, W. T. H. Wenckebach, R. Gruetter, and J. J. van der Klink. Design and performance of a DNP prepolarizer coupled to a rodent MRI scanner. *Concepts in Magnetic Resonance Part B-Magnetic Resonance Engineering*, 31B(4):255–269, 2007.

- [41] A. Comment, S. Jannin, J. N. Hyacinthe, P. Mieville, R. Sarkar, P. Ahuja, P. R. Vasos, X. Montet, F. Lazeyras, J. P. Vallee, P. Hautle, J. A. Konter, B. van den Brandt, J. P. Ansermet, R. Gruetter, and G. Bodenhausen. Hyperpolarizing gases via dynamic nuclear polarization and sublimation. *Physical Review Letters*, 105(1):8104 1–4, 2010.
- [42] A. Comment and M. E. Merritt. Hyperpolarized magnetic resonance as a sensitive detector of metabolic function. *Biochemistry*, 53(47):7333–7357, 2014.
- [43] A. Comment, J. Rentsch, F. Kurdzesau, S. Jannin, K. Uffmann, R. B. van Heeswijk, P. Hautle, J. A. Konter, B. van den Brandt, and J. J. van der Klink. Producing over 100 ml of highly concentrated hyperpolarized solution by means of dissolution DNP. *Journal of Magnetic Resonance*, 194(1):152–155, 2008.
- [44] C. Cudalbu, A. Comment, F. Kurdzesau, R. B. van Heeswijk, K. Uffmann, S. Jannin, V. Denisov, D. Kirik, and R. Gruetter. Feasibility of in vivo ^{15}N MRS detection of hyperpolarized ^{15}N labeled choline in rats. *Physical Chemistry Chemical Physics*, 12(22):5818–5823, 2010.
- [45] S. E. Day, M. I. Kettunen, F. A. Gallagher, D.-E. Hu, M. Lerche, J. Wolber, K. Golman, J.-H. Ardenkjaer-Larsen, and K. M. Brindle. Detecting tumor response to treatment using hyperpolarized ^{13}C magnetic resonance imaging and spectroscopy. *Nature medicine*, 13(11):1382–1387, 2007.
- [46] K. B. Dillon. Chapter 2: Nuclear quadrupole resonance spectroscopy. *Specialist Periodical Reports-Spectroscopic Properties of Inorganic and Organometallic C*, 26:202–225, 1993.
- [47] G. Duhamel, P. Choquet, E. Grillon, L. Lamalle, J. L. Leviel, A. Ziegler, and A. Constantinesco. ^{129}Xe MR imaging and spectroscopy of rat brain using arterial

- delivery of hyperpolarized xenon in a lipid emulsion. *Magnetic Resonance in Medicine*, 46(2):208–212, 2001.
- [48] T. R. Eichhorn. Dynamic nuclear polarization with paramagnetic centers created by photo-excitation. 2014.
- [49] T. R. Eichhorn, Y. Takado, N. Salameh, A. Capozzi, T. Cheng, J. N. Hyacinthe, M. Mishkovsky, C. Roussel, and A. Comment. Hyperpolarization without persistent radicals for in vivo real-time metabolic imaging. *Proceedings of the National Academy of Sciences of the United States of America*, 110(45):18064–18069, 2013.
- [50] C. T. Farrar, D. A. Hall, G. J. Gerfen, S. J. Inati, and R. G. Griffin. Mechanism of dynamic nuclear polarization in high magnetic fields. *The Journal of Chemical Physics*, 114(11):4922–4933, 2001.
- [51] R. J. Fitzgerald, M. Gatzke, D. C. Fox, G. D. Cates, and W. Happer. ^{129}Xe spin relaxation in frozen xenon. *Physical Review B*, 59(13):8795–8811, 1999.
- [52] G. J. Gerfen, L. R. Becerra, D. A. Hall, R. G. Griffin, R. J. Temkin, and D. J. Singel. High frequency (140 GHz) dynamic nuclear polarization: polarization transfer to a solute in frozen aqueous solution. *The Journal of chemical physics*, 102(24):9494–9497, 1995.
- [53] S. T. Goertz, J. Harmsen, J. Heckmann, C. Hess, W. Meyer, E. Radtke, and G. Reicherz. Highest polarizations in deuterated compounds. *Nuclear Instruments and Methods in Physics Research Section A: Accelerators, Spectrometers, Detectors and Associated Equipment*, 526(1):43–52, 2004.
- [54] K. Golman, O. Axelsson, H. Jóhannesson, S. Månsson, C. Olofsson, and J. S. Petersson. Parahydrogen-induced polarization in imaging: Subsecond ^{13}C angiography. *Magnetic Resonance in Medicine*, 46(1):1–5, 2001.

- [55] K. Golman, L. E. Olsson, O. Axelsson, S. Månsson, and M. and Petersson J. S. Karlsson. Molecular imaging using hyperpolarized ^{13}C . *British Journal of Radiology*, 76(2):S118–S127, February 2014.
- [56] K. Golman, M. Thaning, et al. Real-time metabolic imaging. *Proceedings of the National Academy of Sciences*, 103(30):11270–11275, 2006.
- [57] J. Granwehr and W. Köckenberger. Multidimensional low-power pulse EPR under DNP conditions. *Applied Magnetic Resonance*, 34(3-4):355–378, 2008.
- [58] M. I. Guzman, A. J. Colussi, and M. R. Hoffmann. Photogeneration of distant radical pairs in aqueous pyruvic acid glasses. *The Journal of Physical Chemistry A*, 110(3):931–935, 2006.
- [59] M. I. Guzman, A. J. Colussi, and M. R. Hoffmann. Photoinduced oligomerization of aqueous pyruvic acid. *The Journal of Physical Chemistry A*, 110(10):3619–3626, 2006.
- [60] E. M. Haacke, R. W. Brown, M. R. Thompson, and R. Venkatesan. *Magnetic resonance imaging: physical principles and sequence design*. Wiley-Blackwel, 1999.
- [61] T. Harris, G. Eliyahu, L. Frydman, and H. Degani. Kinetics of hyperpolarized ^{13}C -1-pyruvate transport and metabolism in living human breast cancer cells. *Proceedings of the National Academy of Sciences*, 106(43):18131–18136, 2009.
- [62] J. Heckmann, W. Meyer, E. Radtke, and G. Reicherz. Electron spin resonance and its implication on the maximum nuclear polarization of deuterated solid target materials. *Physical Review B*, 74(13):134418(1–9), 2006.
- [63] R. B. van Heeswijk, K. Uffmann, A. Comment, F. Kurdzesau, C. Perazzolo, C. Cudalbu, S. Jannin, J. A. Konter, P. Hautle, B. van den Brandt, G. Navon,

- J. J. van der Klink, and R. Gruetter. Hyperpolarized ^6Li as a sensor of nanomolar contrast agents. *Magnetic Resonance in Medicine*, 61(6):1489–1493, 2009.
- [64] F. W. Hersman, I. C. Ruset, S. Ketel, I. Muradian, S. D. Covrig, J. Distelbrink, W. Porter, D. Watt, J. Ketel, J. Brackett, A. Hope, and S. Patz. Large production system for hyperpolarized ^{129}Xe for human lung imaging studies. *Academic Radiology*, 15(6):683–692, 2008.
- [65] C. Hess, J. Herick, A. Berlin, W. Meyer, and G. Reicherz. Measurement of electron spin-lattice relaxation times in radical doped butanol samples at 1 K using the NEDOR method. *Nuclear Instruments and Methods in Physics Research Section A: Accelerators, Spectrometers, Detectors and Associated Equipment*, 694:69–77, 2012.
- [66] M. L. Hirsch, N. Kalechofsky, A. Belzer, M. Rosay, and J. G. Kempf. Brute-force hyperpolarization for NMR and MRI. *Journal of the American Chemical Society*, 137(26):8428–8434, 2015.
- [67] M. J. R. Hoch and E. C. Reynhardt. Nuclear spin-lattice relaxation of dilute spins in semiconducting diamond. *Physical Review B*, 37(16):9222, 1988.
- [68] R. E. Hurd, Y.-F. Yen, A. Chen, and J.-H. Ardenkjaer-Larsen. Hyperpolarized ^{13}C metabolic imaging using dissolution dynamic nuclear polarization. *Journal of Magnetic Resonance Imaging*, 36(6):1314–1328, 2012.
- [69] S. Jannin, A. Bornet, R. Melzi, and G. Bodenhausen. High field dynamic nuclear polarization at 6.7 T: ^{13}C polarization above 70% within 20 min. *Chemical Physics Letters*, 549:99–102, 2012.
- [70] S. Jannin, A. Comment, and J. J. van der Klink. Dynamic nuclear polarization

- by thermal mixing under partial saturation. *Applied Magnetic Resonance*, 43(1-2):59–68, 2012.
- [71] S. Jannin, A. Comment, F. Kurdzesau, J. A. Konter, P. Hautle, B. van den Brandt, and J. J. van der Klink. A 140 GHz prepolarizer for dissolution dynamic nuclear polarization. *Journal of Chemical Physics*, 128(24):241102 1–4, 2008.
- [72] H. Johanneson, S. Macholl, and J. H. Ardenkjaer-Larsen. Dynamic nuclear polarization of $[1\text{-}^{13}\text{C}]$ pyruvic acid at 4.6 T. *Journal of Magnetic Resonance*, 197(2):167–175, 2009.
- [73] H. Johannesson, O. Axelsson, and M.s Karlsson. Transfer of para-hydrogen spin order into polarization by diabatic field cycling. *Comptes Rendus Physique*, 5(3):315–324, 2004.
- [74] H. Johannesson, O. Axelsson, M. Karlsson, and M. Goldman. Methods to convert para-hydrogen spin order into hetero nuclei polarization for in vivo detection. In *Proc 21st Annual Meeting ESMRMB*, 2004.
- [75] J. Jokisaari. NMR of noble-gases dissolved in isotropic and anisotropic liquids. *Progress in Nuclear Magnetic Resonance Spectroscopy*, 26:1–26, 1994.
- [76] R. Kaptein, K. Dijkstra, and K. Nicolay. Laser photo-CIDNP as a surface probe for proteins in solution. *Nature*, 274:293–294, 1978.
- [77] M. Karlsson, P. R. Jensen, J. O. Duus, S. Meier, and M. H. Lerche. Development of dissolution DNP-MR substrates for metabolic research. *Applied Magnetic Resonance*, 43(1-2):223–236, 2012.
- [78] C. Kittel. *Introduction to solid state physics*. Wiley, 2005.

- [79] M. J. Klein. Overhauser nuclear polarization effect and minimum entropy production. *Physical Review*, 98(6):1736, 1955.
- [80] K. V. Kovtunov, M. L. Truong, D. A. Barskiy, O. G. Salnikov, V. I. Bukhtiyarov, A. M. Coffey, K. W. Waddell, I. V. Koptug, and E. Y. Chekmenev. Propane-d(6) heterogeneously hyperpolarized by parahydrogen. *Journal of Physical Chemistry C*, 118(48):28234–28243, 2014.
- [81] F. Kurdzesau, B. van den Brandt, A. Comment, P. Hautle, S. Jannin, J. J. van der Klink, and J. A. Konter. Dynamic nuclear polarization of small labelled molecules in frozen water-alcohol solutions. *Journal of Physics D-Applied Physics*, 41(15):155506 1–10, 2008.
- [82] N. N. Kuzma, B. Patton, K. Raman, and W. Happer. Fast nuclear spin relaxation in hyperpolarized solid ^{129}Xe . *Physical Review Letters*, 88(14):147602, 2002.
- [83] N. N. Kuzma, M. Pourfathi, H. Kara, P. Manasseh, R. K. Ghosh, J. H. Ardenkjaer-Larsen, S. J. Kadlecik, and R. R. Rizi. Cluster formation restricts dynamic nuclear polarization of xenon in solid mixtures. *Journal of Chemical Physics*, 137(10):104508 1–6, 2012.
- [84] M. Kveder, D. Merunka, M. Jokić, J. Makarević, and B. Rakvin. Electron spin-lattice relaxation in solid ethanol: Effect of nitroxyl radical hydrogen bonding and matrix disorder. *Physical review B*, 80(5):052201, 2009.
- [85] S. Lang, I. L. Moudrakovski, C. I. Ratcliffe, J. A. Ripmeester, and G. Santyr. Increasing the spin-lattice relaxation time of hyperpolarized Xe ice at 4.2 K. *Applied Physics Letters*, 80(5):886–887, 2002.
- [86] Y. Lee, G. S. Heo, H. Zeng, K. L. Wooley, and C. Hilty. Detection of living

- anionic species in polymerization reactions using hyperpolarized NMR. *Journal of the American Chemical Society*, 135(12):4636–4639, 2013.
- [87] Y. Lee, H. Zeng, S. Ruedisser, A. D Gossert, and C. Hilty. Nuclear magnetic resonance of hyperpolarized fluorine for characterization of protein-ligand interactions. *Journal of the American Chemical Society*, 134(42):17448–17451, 2012.
- [88] P. A. Leermakers and G. F. Vesley. The photochemistry of α -keto acids and α -keto esters. I. photolysis of pyruvic acid and benzoylformic acid. *Journal of the American Chemical Society*, 85(23):3776–3779, 1963.
- [89] M. H. Lerche, P. R. Jensen, M. Karlsson, and S. Meier. NMR insights into the inner workings of living cells. *Analytical Chemistry*, 87(1):119–132, 2015.
- [90] M. H. Levitt. *Spin dynamics: basics of nuclear magnetic resonance*. John Wiley & Sons, 2001.
- [91] G. N. Lewis and M. Kasha. Phosphorescence and the triplet state. *Journal of the American Chemical Society*, 66(12):2100–2116, 1944.
- [92] D. R. Lide. *CRC Handbook of Chemistry and Physics*. CRC Press /Taylor and Francis, Boca Raton, FL, 90th edition, 2009.
- [93] D. M. L. Lilburn, T. Hughes-Riley, J. S. Six, K. F. Stupic, D. E. Shaw, G. E. Pavlovskaya, and T. Meersmann. Validating excised rodent lungs for functional hyperpolarized ^{129}Xe MRI. *PLoS One*, 8(8):e73468 1–13, 2013.
- [94] A. J. P. Linde, A. Bornet, J. Milani, B. Vuichoud, R. Melzi, S. Jannin, and G. Bodenhausen. Cross polarization from ^1H to quadrupolar ^6Li nuclei for dissolution DNP. *Physical Chemistry Chemical Physics*, 16(45):24813–24817, 2014.

- [95] S. K. Lower and M. A. El-Sayed. The triplet state and molecular electronic processes in organic molecules. *Chemical Reviews*, 66(2):199–241, 1966.
- [96] L. Lumata, Z. Kovacs, C. Malloy, A. D. Sherry, and M. E. Merritt. The effect of ^{13}C enrichment in the glassing matrix on dynamic nuclear polarization of $[1-^{13}\text{C}]$ pyruvate. *Physics in medicine and biology*, 56(5):N85, 2011.
- [97] L. Lumata, Z. Kovacs, A. D. Sherry, C. Malloy, S. Hill, J. van Tol, L. Yu, L. Song, and M. E. Merritt. Electron spin resonance studies of trityl OX063 at a concentration optimal for DNP. *Physical Chemistry Chemical Physics*, 15(24):9800–9807, 2013.
- [98] L. Lumata, M. E. Merritt, C. Khemtong, S. J. Ratnakar, J. van Tol, L. Yu, L. Song, and Z. Kovacs. The efficiency of DPPH as a polarising agent for DNP-NMR spectroscopy. *RSC advances*, 2(33):12812–12817, 2012.
- [99] L. Lumata, M. E. Merritt, and Z. Kovacs. Influence of deuteration in the glassing matrix on ^{13}C dynamic nuclear polarization. *Physical Chemistry Chemical Physics*, 15(19):7032–7035, 2013.
- [100] L. Lumata, M. E. Merritt, C. R. Malloy, A. D. Sherry, and Z. Kovacs. Impact of Gd^{3+} on DNP of $[1-^{13}\text{C}]$ pyruvate doped with trityl OX063, BDPA, or 4-oxo-TEMPO. *The Journal of Physical Chemistry A*, 116(21):5129–5138, 2012.
- [101] L. Lumata, S. J. Ratnakar, A. Jindal, M. E. Merritt, A. Comment, C. Malloy, A. D. Sherry, and Z. Kovacs. BDPA: An efficient polarizing agent for fast dissolution dynamic nuclear polarization NMR spectroscopy. *Chemistry-a European Journal*, 17(39):10825–10827, 2011.
- [102] S. Macholl, H. Jóhannesson, and J.-H. Ardenkjaer-Larsen. Trityl biradicals

- and ^{13}C dynamic nuclear polarization. *Physical Chemistry Chemical Physics*, 12(22):5804–5817, 2010.
- [103] S. Mango. Early target material research with chemical dopants. *Nuclear Instruments and Methods in Physics Research Section A: Accelerators, Spectrometers, Detectors and Associated Equipment*, 526(1):1–6, 2004.
- [104] S. Mansson, E. Johansson, P. Magnusson, C.-M. Chai, G. Hansson, J. S. Petersson, F. Stahlberg, and K. Golman. ^{13}C imaging-a new diagnostic platform. *European Radiology*, 16(1):57–67, January 2006.
- [105] P. Miéville, P. Ahuja, R. Sarkar, S. Jannin, P. R. Vasos, S. Gerber-Lemaire, M. Mishkovsky, A. Comment, R. Gruetter, O. Ouari, et al. Scavenging free radicals to preserve enhancement and extend relaxation times in NMR using dynamic nuclear polarization. *Angewandte Chemie*, 122(35):6318–6321, 2010.
- [106] J. Milani, B. Vuichoud, A. Bornet, P. Miéville, R. Mottier, S. Jannin, and G. Bodenhausen. A magnetic tunnel to shelter hyperpolarized fluids. *Review of Scientific Instruments*, 86(2):024101, 2015.
- [107] W. B. Mims, K. Nassau, and J. D. McGee. Spectral diffusion in electron resonance lines. *Physical Review*, 123(6):2059, 1961.
- [108] L. J. Mittal, J. P. Mittal, and E. Hayon. Photo-induced decarboxylation of aliphatic acids and esters in solution. dependence upon state of protonation of the carboxyl group. *The Journal of Physical Chemistry*, 77(12):1482–1487, 1973.
- [109] J. P. Mugler and T. A. Altes. Hyperpolarized ^{129}Xe MRI of the human lung. *Journal of Magnetic Resonance Imaging*, 37(2):313–331, 2013.

- [110] J. Natterer and J. Bargon. Parahydrogen induced polarization. *Progress in Nuclear Magnetic Resonance Spectroscopy*, 31(4):293–315, 1997.
- [111] S. J. Nelson, J. Kurhanewicz, D. B. Vigneron, P. E. Z. Larson, A. L. Harzstark, M. Ferrone, M. van Criekinge, J. W. Chang, R. Bok, I. Park, G. Reed, L. Carvajal, E. J. Small, P. Munster, V. K. Weinberg, J. H. Ardenkjaer-Larsen, A. P. Chen, R. E. Hurd, L. I. Odegardstuen, F. J. Robb, J. Tropp, and J. A. Murray. Metabolic imaging of patients with prostate cancer using hyperpolarized [1- ^{13}C]pyruvate. *Science Translational Medicine*, 5(198):198ra108 1–10, 2013.
- [112] P. Nikolaou, A. M. Coffey, K. Ranta, L. L. Walkup, B. M. Gust, M. J. Barlow, M. S. Rosen, B. M. Goodson, and E. Y. Chekmenev. Multidimensional mapping of spin-exchange optical pumping in clinical-scale batch-mode ^{129}Xe hyperpolarizers. *Journal of Physical Chemistry B*, 118(18):4809–4816, 2014.
- [113] A. W. Overhauser. Polarization of nuclei in metals. *Physical Review*, 92(2):411, 1953.
- [114] I. Park, P. E. Z. Larson, J. L. Tropp, L. Carvajal, G. Reed, R. Bok, F. Robb, J. Bringas, A. Kells, P. Pivrotto, K. Bankiewicz, D. B. Vigneron, and S. J. Nelson. Dynamic hyperpolarized ^{13}C MR metabolic imaging of nonhuman primate brain. *Magnetic Resonance in Medicine*, 71(1):19–25, 2014.
- [115] A. Pines, M. G. Gibby, and J. S. Waugh. Proton-enhanced nuclear induction spectroscopy ^{13}C chemical shielding anisotropy in some organic solids. *Chemical Physics Letters*, 15(3):373–376, 1972.
- [116] A. M. Portis. Spectral diffusion in magnetic resonance. *Physical Review*, 104(3):584, 1956.

- [117] M. Pourfathi, N. N. Kuzma, H. Kara, R. K. Ghosh, H. Shaghaghi, S. J. Kadlec, and R. R. Rizi. Propagation of dynamic nuclear polarization across the xenon cluster boundaries: Elucidation of the spin-diffusion bottleneck. *Journal of Magnetic Resonance*, 235:71–76, 2013.
- [118] B. N. Provotorov. Magnetic resonance saturation in crystals. *Sov. Phys. JETP*, 14(5):1126–1131, 1962.
- [119] I. I. Rabi, J. R. Zacharias, S. Millman, and P. Kusch. A new method of measuring nuclear magnetic moments. *Physical Review*, 53(4):318–, February 1938.
- [120] A. G. Redfield. Nuclear magnetic resonance saturation and rotary saturation in solids. *Physical Review*, 98(6):1787, 1955.
- [121] A. Rigamonti and P. Carretta. *Structure of matter*. Springer, 2007.
- [122] I. C. Ruset, S. Ketel, and F. W. Hersman. Optical pumping system design for large production of hyperpolarized ^{129}Xe . *Physical Review Letters*, 96(5):053002 1–4, 2006.
- [123] G. Schrank, Z. Ma, A. Schoeck, and B. Saam. Characterization of a low-pressure high-capacity ^{129}Xe flow-through polarizer. *Physical Review A*, 80(6):063424 1–10, 2009.
- [124] L. Schroder, T. J. Lowery, C. Hilty, D. E. Wemmer, and A. Pines. Molecular imaging using a targeted magnetic resonance hyperpolarized biosensor. *Science*, 314(5798):446–449, 2006.
- [125] A. Schweiger and G. Jeschke. *Principles of pulse electron paramagnetic resonance*. University Press, Oxford, 2001.

- [126] J. S. Six, T. Hughes-Riley, K. F. Stupic, G. E. Pavlovskaya, and T. Meersmann. Pathway to cryogen free production of hyperpolarized ^{83}Kr and ^{129}Xe . *PLoS One*, 7(11):e49927 1–16, 2012.
- [127] I. Solomon. Polarisation dynamique et détection des signaux de résonance par double irradiation. *Proc Coll Amp*, 11:25–38, 1962.
- [128] S. Stoll and A. Schweiger. EasySpin, a comprehensive software package for spectral simulation and analysis in EPR. *Journal of Magnetic Resonance*, 178(1):42–55, 2006.
- [129] O. Taratula and I. J. Dmochowski. Functionalized ^{129}Xe contrast agents for magnetic resonance imaging. *Current Opinion in Chemical Biology*, 14(1):97–104, 2010.
- [130] R. Tycko and G. Dabbagh. Nuclear magnetic resonance crystallography: molecular orientational ordering in three forms of solid methanol. *Journal of the American Chemical Society*, 113(9):3592–3593, 1991.
- [131] J. H. van Vleck. The dipolar broadening of magnetic resonance lines in crystals. *Physical Review*, 74(9):1168, 1948.
- [132] T. G. Walker and W. Happer. Spin-exchange optical pumping of noble-gas nuclei. *Reviews of Modern Physics*, 69(2):629–642, 1997.
- [133] L. L. Walkup and J. C. Woods. Translational applications of hyperpolarized ^3He and ^{129}Xe . *NMR in Biomedicine*, 27(12):1429–1438, 2014.
- [134] W. T. Wenckebach. Thermodynamics of dynamic nuclear polarization. *Nuclear Instruments and Methods in Physics Research Section A: Accelerators, Spectrometers, Detectors and Associated Equipment*, 356(1):1–4, 1995.

- [135] W. T. Wenckebach, T. J. B. Swannenburg, and N. J. Poulis. Thermodynamics of spin systems in paramagnetic crystals. *Physics Reports*, 14(5):181–255, 1974.
- [136] L. Wharton, L. P. Gold, and W. Klemperer. Quadrupole moment of ^6Li . *Physical Review*, 133(2B):B270, 1964.
- [137] R. A. Wind, M. J. Duijvestijn, C. van der Lugt, A. Manenschijn, and J. Vriend. Applications of dynamic nuclear polarization in ^{13}C NMR in solids. *Progress in Nuclear Magnetic Resonance Spectroscopy*, 17:33–67, 1985.
- [138] J. Wolber, F. Ellner, B. Fridlund, A. Gram, H. Johannesson, G. Hansson, L. H. Hansson, M. H. Lerche, S. Månsson, R. Servin, et al. Generating highly polarized nuclear spins in solution using dynamic nuclear polarization. *Nuclear Instruments and Methods in Physics Research Section A: Accelerators, Spectrometers, Detectors and Associated Equipment*, 526(1):173–181, 2004.
- [139] C. I. Yaws. *Thermophysical properties of chemicals and hydrocarbons*. William Andrew, 2nd edition, 2014.
- [140] X. Zhou, Y. P. Sun, M. Mazzanti, N. Henninger, J. Mansour, M. Fisher, and M. Albert. MRI of stroke using hyperpolarized ^{129}Xe . *NMR in Biomedicine*, 24(2):170–175, 2011.

List of publications

Journal papers

- **Capozzi A.**, van der Klink J.J, Cheng T., Breukels V., van Bentum P.J.M., Scheenen T.W.J., Comment A., "High field dynamic nuclear polarization: the role of "proton-assisted" ^{13}C spin diffusion", Journal of Physical Chemistry C, 2015, submitted.
- **Capozzi A.**, Hyacinthe J.-N., Cheng T., Eichhorn T.R., Boero G., Roussel C., van der Klink J.J., Comment A., "Photo-Induced non-Persistent Radicals as Polarizing Agents for X-Nuclei dissolution-DNP", Journal of Physical Chemistry C, 2015, 119, 22632-22639.
- Breukels V., Jansen K.C.F.J., van Heijster F.H.A., **Capozzi A.**, van Bentum P.J.M., Schalken J.A., Comment A., Scheenen, T.W.J., "Direct dynamic measurement of intracellular and extracellular lactate in small-volume cell suspensions with ^{13}C hyperpolarized NMR", NMR in Biomedicine, 2015, 28, 1040-1048.
- **Capozzi A.**, Roussel C., Comment A., Hyacinthe J.-N., "Optimal glass-forming solvent brings sublimation dynamic nuclear polarization to ^{129}Xe hyperpolarization biomedical imaging standards", Journal of Physical Chemistry C, 2015, 119, 5020-5025.

- Orlando T., **Capozzi A.**, Umut E., Bordonali L., Mariani M., Galinetto P., Pineider F., Innocenti C., Masala P., Tabak F., Scavini M., Santini P., Corti M., Sangregorio, C., Ghigna P., Lascialfari A., “Spin dynamics in hybrid iron oxide-gold nanostructures”, *Journal of Physical Chemistry C*, 15, 119, 1224-1233.
- Cheng T., **Capozzi A.**, Takado Y., Balzan R., Comment A., “Over 35% liquid state ^{13}C polarization obtained via dissolution-dynamic nuclear polarization at 7 T and 1 K using ubiquitous nitroxyl radicals”, *Physical Chemistry Chemical Physics*, 2013, 15, 20819-20822.
- Eichhorn T.R., Takado, Y., Salameh N., **Capozzi A.**, Cheng T., Hyacinthe J.-N., Mishkovsky M., Roussel C., Comment A., “Hyperpolarization without persistent radicals for in vivo real-time metabolic imaging”, *Proceedings of the National Academy of Sciences of the United States of America*, 2013, 110, 18064-18069.

Book chapters

- “Hyperpolarized xenon-129 magnetic resonance”. Edited by Thomas Meersmann and Eike Brunner. *New developments in NMR – Royal Society of Chemistry Books*. Volume 2015-January, Issue 4, 2015, Pages 442-452: “Beyond spin exchange optical pumping: hyperpolarization of xenon-129 via sublimation dynamic nuclear polarization”. Hyacinthe J.-N., **Capozzi A.**, Comment A..

Conference papers

- “In vivo hyperpolarized MR at physiological and pharmaceutical bioprobe concentrations to study cerebral function and metabolism”, Mishkovsky M., **Capozzi**

A., Takado Y., Gruetter R., Comment A., 5th International Symposium on DNP, 31st August -4th September 2015, Egmond aan Zee, The Netherlands.

- "Co-polarization of radical-free mixtures of ^{13}C -metabolites to probe separate biochemical pathways simultaneously in vivo by hyperpolarized ^{13}C MR", Bastiaansen J.A.M., Yoshihara H.A.I, **Capozzi A.**, Schwitter J., Gruetter R., Merritt M.E. and Comment A., 5th International Symposium on Dynamic Nuclear Polarization (2015).
- "Radical-free mixture of co-polarized ^{13}C metabolites for probing separate biochemical pathways in vivo by hyperpolarized ^{13}C MR". Bastiaansen J.A.M., Yoshihara H.A.I., **Capozzi A.**, Schwitter J., Merritt M.E., Comment A.. Proceedings of the International Society for Magnetic Resonance in Medicine, 23 (2015), p. 416, ISMRM 23rd Annual Meeting, 30 May -5 June 2015, Toronto, Canada.
- "Dynamic Imaging of Hyperpolarized ^6Li Cerebral Distribution at Pharmacological Concentration", Mishkovsky M., **Capozzi A.**, Salameh N., Hyacinthe J.-N., Gruetter R., Comment A.. Proc. Intl. Soc. Mag. Reson. Med. 23, 324 (2015). ISMRM 23rd Annual Meeting, 30 May -5 June 2015, Toronto, Canada.
- "Optimal Glass Forming Solvent and Photo-Induced Radicals Yield ^{129}Xe Hyperpolarization Via Sublimation-DNP to Biomedical Imaging Standards". **Capozzi A.**, Roussel C., Comment A., Hyacinthe J.-H.. Proc. Intl. Soc. Mag. Reson. Med. 23, 324 (2015). ISMRM 23rd Annual Meeting, 30 May -5 June 2015, Toronto, Canada.
- "B1 Correction in Spatiotemporal Encoding (SPEN) MRI". Schmidt R., Hyacinthe J.-H., **Capozzi A.**, Kunz N., Gruetter R., Comment A., Frydman L.,

- Mishkovsky M.. Proc. Intl. Soc. Mag. Reson. Med. 23, 324 (2015). ISMRM 23rd Annual Meeting, 30 May -5 June 2015, Toronto, Canada.
- “Photo-induced non-persistent radicals as polarizing agents for multi-nuclei dissolution-DNP”, **Capozzi A.**, Hyacinthe J.-N., Cheng T., Eichhorn T.R., Boero G., Roussel C., Comment A., 56th ENC, April 19 - 24, 2015 at the Asilomar Conference Center, Pacific Grove, CA.
 - “Optimal glass forming solvent and photo-induced radicals bring ^{129}Xe hyperpolarization via sublimation-DNP to biomedical imaging standards”, **Capozzi A.**, Roussel C., Comment A., Hyacinthe J.-N., 56th ENC, April 19 - 24, 2015 at the Asilomar Conference Center, Pacific Grove, CA.
 - “Three fields study of solvent deuteration influence on the Dynamic Nuclear Polarization process for hyperpolarized ^{13}C MRS and MRI”. **Capozzi A.**, Cheng T., Bruekels V., van der Klink J.J., Comment A.. SPS 2014, Fribourg, Switzerland, July 2014.
 - “100 ml of natural abundance Xe gas hyperpolarized up to 25% in about 30 min via sublimation-DNP”. **A. Capozzi**, J.-N. Hyacinthe, N. Salameh, A. Comment. Euromar 2014, ETH Zurich, Switzerland, June 2014. • “Photo-induced radicals improves ^{129}Xe Hyperpolarization via sublimation-DNP”. J.-N. Hyacinthe, **A. Capozzi**, N. Salameh, A. Comment. Euromar 2014, ETH Zurich, Switzerland, June 2014.
 - “Influence of solvent deuteration on the dynamic nuclear polarization process at different magnetic fields”. **A. Capozzi**, T. Cheng, V. Breukels, J. P. van Bentum, T. Scheenen, J.J. van der Klink, A. Comment. COST Euro-Hyperpol, WG2/WG3 Joint Meeting, Southampton, England, May 2014.

- “A new low volume NMR tube for in-vitro hyperpolarized ^{13}C experiments of prostate cancer cell suspensions”. V. Breukels, C. F. J. Jansen, van Asten, J. A. Jack, van Os, W. M. Jan, **A. Capozzi**, P. J. M. van Bentum, A. Comment and T. W. J. Scheenen. 22nd Annual ISMRM Meeting, Milan, Italy, May 10-16, 2014.
- “In vivo real-time metabolic imaging using frequency selective bSSFP and hyperpolarized compounds”. N. Salameh, J.-N. Hyacinthe, **A. Capozzi** and A. Comment. 22nd Annual ISMRM Meeting, Milano, Italy, May 10-16, 2014.
- “A 140 GHz Corrugated Waveguide based on Stacked Rings Technology for dissolution-DNP”. T. Cheng, **A. Capozzi**, A. Comment. 55th ENC, Boston, Massachusetts, March 23-28, 2014; Boston, Massachusetts, 2014.
- “Influence of solvent deuteration on the dynamic nuclear polarization process at different magnetic fields”. **A. Capozzi**, T. Cheng, V. Breukels, J. P. van Bentum, T. Scheenen, J.J. van der Klink, A. Comment. 55th ENC, Boston, Massachusetts, March 23-28, 2014; Boston, Massachusetts, 2014.
- “ ^{13}C DNP efficiency as a function of the glassing matrix content at different magnetic fields”. **A. Capozzi**, T. Cheng, R. Balzan, V. Breukels, J. van Bentum, T. Scheenen and A. Comment. 4th DNP Symposium, Copenhagen, August 28-30, 2013.
- “Accurate fast low-angle solid state nuclear polarization measurement”. R. Balzan, **A. Capozzi**, T. Cheng and A. Comment. 4th International DNP Symposium, Elsinore, Denmark, August 28-31, 2013.
- “Hyperpolarization of ^{129}Xe by sublimation DNP using photo-activated radical precursors”. J.-N. Hyacinthe, **A. Capozzi**, T. R. Eichhorn, N. Salameh, C. Rousel, F. Lazeyras and A. Comment. 4th International DNP Symposium, Elsinore,

Denmark, August 28-31, 2013.

- “Over 35% of liquid state ^{13}C polarization enhanced by TEMPOL via high field dissolution dynamic nuclear polarization”. T. Cheng, **A. Capozzi**, Y. Takado, R. Balzan and A. Comment. 4th International DNP Symposium, Elsinore, Denmark, August 28-31, 2013.
- “Development of a user facility for dissolution-DNP development and applications”. A. N. Smith, D. P. Downes, R. Balzan, **A. Capozzi**, A. Comment and J. R. Long. 4th International DNP Symposium, Elsinore, Denmark, August 28-31, 2013.
- “LNCaP shows increased pyruvate to alanine conversion compared to other prostate cancer cell lines”. V. Breukels, C. F. J. Jansen, van Asten, J. A. Jack, **A. Capozzi**, van Os, W. M. Jan, P. J. M. van Bentum, A. Comment, J. A. Schalken and T. W. J. Scheenen. 4th International DNP Symposium, Elsinore, Denmark, August 28-31, 2013.
- “Spin Dynamics in Magneto-plasmonic Hybrid Nanostructures”. **A. Capozzi**, E. Umut, T. Orlando, M. Mariani, F. Pineider, C. Sangregorio, M. Corti, F. Tabak, A. Lascialfari, P. Ghigna. JEMS 2012, Parma, Italy, September 9-14, 2012.

Curriculum vitae

ANDREA CAPOZZI

CH F1 542 (Bâtiment CH), Station 6, CH-1015 Lausanne

e-mail: andrea.capozzi@epfl.ch

phone: +41 21 69 30383 - mobile: +41774437665

Education

PhD student in Physics [Jan 2012 – today]

École polytechnique fédérale de Lausanne (EPFL)

PhD thesis major subject: methods to hyperpolarize nuclear spins via dissolution and sublimation DNP at high magnetic field

Relevant topics: different fields solid state DNP; dissolution-DNP; sublimation-DNP; hyperpolarized ^{13}C , ^{129}Xe , ^6Li NMR; EPR of photo-induced radicals; cryogenics; high magnetic field coil design.

Master degree in Physics [Oct 2009 – Dec 2011]**University of Pavia, Italy**

Grade: 110/110 cum Laude, top 5 percent of year group.

Master thesis major subject: investigation of the physical properties of Au – Fe₃O₄ hybrid nanoparticles by means of NMR spectroscopy with potential applications in biomedicine.

Relevant topics: theory of magnetism, phase transition, superconductivity, statistical mechanics, photonics, NMR, MRI, ionizing radiations.

IUSS (Excellence School) [Sept 2006 – May 2012]**Pavia, Italy**

Grade: excellent.

Final thesis major subject: DNP - physics principles and biomedical applications.

Relevant topics: story of Mathematics, astronomy, materials science, numerical models, optical tweezers (high level academic records, exams by deadlines).

Bachelor degree in Physics [Sept 2006 – Dec 2009]**University of Pavia, Italy**

Grade: 110/110 cum Laude, top 5 percent of year group.

Bachelor thesis major subject: Surface Enhanced Raman Scattering - theoretical principles and applications to biological systems.

Alumnus of Collegio Ghislieri [Sept 2006 - Dec 2011]

Pavia, Italy

High level academic records, exams by deadlines, international environment.

Further achievements

Prizes

- EPFL PhD special prize, October 2014.

Workshops and scientific collaborations

- BioNMR Workshop at Weizmann Institute, Rehovot, Israel, February 26-28, 2013.
- Winter School at Paul Scherrer Institute, 3 - 7 December 2012: “Dynamic Nuclear Polarization using strong microwaves, W. Th Wenckebach.
- Scientific collaboration with Paul Scherrer Institute, Villigen, Switzerland, October 2013, February 2014, February 2015, April 2015.
- Scientific collaboration with University of Pavia, Pavia, Italy, July 2013.
- Scientific collaboration with University of Lund, Lund, Sweden, June 2013.
- Scientific collaboration with University of Florida, Gainesville, United States of America, March 2013.
- Scientific Collaboration with Radboud University, Nijmegen, Netherlands, January 2013, March 2014.

Teaching experience

NMR class for 3rd year Physics students: theory and experiments.

Language skills and IT

Italian: mother tongue

English: fluent

French: fluent

Application programs: Windows, Office, Origin, Labview, MatLab, Inkscape, Gimp.

